REWAS 2022

Energy Technologies and CO_2 Management

VOLUME II

EDITORS

Fiseha Tesfaye
Lei Zhang
Donna Post Guillen
Ziqi Sun
Alafara Abdullahi Baba
Neale R. Neelameggham
Mingming Zhang
Dirk E. Verhulst
Shafiq Alam

TMS

Springer

The Minerals, Metals & Materials Series

Fiseha Tesfaye · Lei Zhang · Donna Post Guillen ·
Ziqi Sun · Alafara Abdullahi Baba ·
Neale R. Neelameggham · Mingming Zhang ·
Dirk E. Verhulst · Shafiq Alam
Editors

REWAS 2022: Energy Technologies and CO_2 Management (Volume II)

TMS

Springer

Editors
Fiseha Tesfaye
Åbo Akademi University
Turku, Finland

Donna Post Guillen
Idaho National Laboratory
Idaho Falls, ID, USA

Alafara Abdullahi Baba
University of Ilorin
Ilorin, Nigeria

Mingming Zhang
Wood Mackenzie
Chicago, IL, USA

Shafiq Alam
University of Saskatchewan
Saskatoon, SK, Canada

Lei Zhang
University of Alaska Fairbanks
Fairbanks, AK, USA

Ziqi Sun
Queensland University of Technology
Brisbane, QLD, Australia

Neale R. Neelameggham
IND LLC
South Jordan, UT, USA

Dirk E. Verhulst
Reno, NV, USA

ISSN 2367-1181 ISSN 2367-1696 (electronic)
The Minerals, Metals & Materials Series
ISBN 978-3-030-92558-1 ISBN 978-3-030-92559-8 (eBook)
https://doi.org/10.1007/978-3-030-92559-8

© The Minerals, Metals & Materials Society 2022
This work is subject to copyright. All rights are solely and exclusively licensed by the Publisher, whether the whole or part of the material is concerned, specifically the rights of translation, reprinting, reuse of illustrations, recitation, broadcasting, reproduction on microfilms or in any other physical way, and transmission or information storage and retrieval, electronic adaptation, computer software, or by similar or dissimilar methodology now known or hereafter developed.
The use of general descriptive names, registered names, trademarks, service marks, etc. in this publication does not imply, even in the absence of a specific statement, that such names are exempt from the relevant protective laws and regulations and therefore free for general use.
The publisher, the authors and the editors are safe to assume that the advice and information in this book are believed to be true and accurate at the date of publication. Neither the publisher nor the authors or the editors give a warranty, expressed or implied, with respect to the material contained herein or for any errors or omissions that may have been made. The publisher remains neutral with regard to jurisdictional claims in published maps and institutional affiliations.

This Springer imprint is published by the registered company Springer Nature Switzerland AG
The registered company address is: Gewerbestrasse 11, 6330 Cham, Switzerland

Preface

Volume II of the *REWAS 2022* proceedings contains peer-reviewed papers presented at the REWAS 2022: Energy Technologies and CO_2 Management symposium, organized in conjunction with the TMS 2022 Annual Meeting & Exhibition and REWAS 2022. The symposium was sponsored by the TMS Extraction and Processing Division (EPD), Light Metals Division (LMD), and Energy Committee.

The papers in this volume intend to address issues related to intricacies, challenges, and development of new strategies as the reliance on fossil fuels for energy is unsustainable and has released an unprecedented amount of carbon dioxide into our atmosphere. The continual research and development effort into clean and sustainable energy technologies and efficient carbon dioxide management are of paramount importance to ensure the responsible progress of human civilization and innovations.

The REWAS 2022: Energy Technologies and CO_2 Management symposium was open to participants from both industry and academia with a focus on energy-efficient technologies including innovative ore beneficiation, smelting technologies, recycling and waste heat recovery, as well as emerging novel energy technologies. The topics cover various technological aspects of sustainable energy ecosystems, processes that improve energy efficiency, reduce thermal emissions, and reduce carbon dioxide and other greenhouse emissions. Contributions from all areas of non-nuclear and non-traditional energy sources are discussed.

Topics include renewable energy resources to reduce the consumption of traditional fossil fuels; emerging technologies for renewable energy harvesting, conversion, and storage; new concepts or devices for energy generation, conversion, and distribution; waste heat recovery and other industrial energy efficient technologies; energy education and energy regulation; scale-up, stability, and life cycle analysis of energy technologies, and improvement of existing energy intensive processes; theory and simulation in energy harvesting, conversion, and storage; design, operation, and optimization of processes for energy generation (e.g., carbon capture) and conversion of energy carriers; energy efficiency improvement in process engineering (e.g., for biomass conversion and improved combustion) and electrical engineering (e.g., for power conversion and developing smart grids); thermoelectric/electrolysis/photoelectrolysis/fundamentals of PV; emission control; CO_2

capture and conversion, carbon sequestration techniques, CO_2 and other greenhouse gas reduction metallurgy in ferrous (iron and steel making and forming), non-ferrous and reactive metals including critical rare-earth metals; sustainability and life cycle assessment of energy systems; and thermodynamics and modelling for sustainable metallurgical processes.

We hope this volume will serve as a reference for materials scientists and engineers as well as metallurgists for exploring innovative energy technologies and novel energy materials processing.

We would like to acknowledge the contributions from the authors of the papers in this volume, the effort of the reviewers involved with the manuscript review process, and the help received from the TMS staff.

Fiseha Tesfaye
Lead Organizer, REWAS 2022: Energy
Technologies and CO_2 Management
Åbo Akademi University
Turku, Finland

Contents

Part I Renewable Energy and Combustion Technologies

Part II Energy Efficiency, Decarbonization and CO_2 Management

Part III Thermal Management and Hydrogen Technology

About the Editors

Fiseha Tesfaye is a senior researcher with the title of Docent (Adjunct Professor) in metallurgical thermodynamics in the Laboratory of Molecular Science and Engineering at Åbo Akademi University, Finland. He received his M.Sc. degree in materials processing technology and Ph.D. degree in metallurgy from Aalto University. His research activities are focused mainly on the thermodynamic investigation of inorganic materials as well as rigorous theoretical and experimental investigations for promoting improved valuable metals and renewable energy production. In 2018, Dr. Tesfaye was also appointed as a visiting research scientist in Seoul National University, South Korea.

Dr. Tesfaye is a regular contributor and active member of The Minerals, Metals & Materials Society (TMS), and is a winner of the 2018 TMS Young Leaders Professional Development Award. He serves as a subject editor for *JOM*, the member journal of TMS, and *Energies*, MDPI. Furthermore, he has edited several scientific research books. His personal research achievements include remarkable improvement of experimental research applying the solid-state EMF technique for thermodynamic investigations of inorganic materials, as well as a noticeable contribution for promoting the transition toward the circular economy. In his research areas, Dr. Tesfaye has published over 60 peer-reviewed articles.

Lei Zhang is an Associate Professor in the Department of Mechanical Engineering at the University of Alaska Fairbanks (UAF). Prior to joining UAF, she worked as a postdoctoral associate in the Department of Chemical and Biomolecular Engineering at the University of Pennsylvania. Dr. Zhang obtained her Ph.D. in Materials Science and Engineering from Michigan Technological University in 2011, and her M.S. and B.E. in Materials Science and Engineering from China University of Mining and Technology, Beijing, China, in 2008 and 2005, respectively. Her current research mainly focuses on the synthesis of Metal-Organic Frameworks (MOFs) and MOF-based nanocomposites, and the manipulation of their properties and applications in gas storage, separation, and water treatment. She is also working on the development and characterization of anti-corrosion coatings on metallic alloys for aerospace and biomedical applications.

Dr. Zhang has served on the TMS Energy Committee since 2014, including the Vice-Chair role in 2018–2020 and the Chair role in 2020–2022. She also served on a Best Paper Award Subcommittee of the committee. She has served as a frequent organizer and session chair of TMS Annual Meeting symposia (2015–present). She was the recipient of the 2015 TMS Young Leaders Professional Development Award.

Donna Post Guillen has over 35 years of research engineering experience and has served as principal investigator/technical lead for numerous multidisciplinary projects encompassing waste heat recovery, combustion, heat exchangers, power conversion systems, nuclear reactor fuels and materials experiments, waste vitrification, and advanced manufacturing. Her core area of expertise is computational modeling of energy systems, materials, and thermal fluid systems. She is experienced with X-ray and neutron beamline experiments, computational methods, tools and software for data analysis, visualization, application development, machine learning and informatics, numerical simulation, and design optimization. As Principal Investigator/Technical Lead for the DOE Nuclear Science User Facility Program, she has engaged in irradiation testing of new materials and performed thermal analysis for nuclear reactor experiments. She actively mentors students, serves in a leadership capacity as well as routinely chairs and organizes technical meetings for professional societies, provides subject matter reviews for proposals and technical manuscripts, has published over 100 papers and received three Best Paper awards, authored numerous technical reports and journal articles, and has written/edited several books.

Ziqi Sun is currently an associate professor and ARC future fellow in the Queensland University of Technology (QUT), Australia. His research interests include developing bio-inspired smart nano-materials and 2D metal oxide nano-materials for sustainable energy and environmental applications, such as rechargeable batteries, oil-water separations, and catalysis. He received his Ph.D. in Materials Science and Engineering from the Institute of Metal Research, Chinese Academy of Sciences in 2009. After one year of experience as the NIMS postdoctoral fellow (Japan) on solid oxide fuel cells, he joined the University of Wollongong (UOW), Australia, in 2010 and moved to QUT as a faculty member in 2015. He has served in some prestigious leadership roles in both the academic and professional communities, such as the chair of the TMS Energy Committee; editor-in-chief of *Sustainable Materials and Technologies* (CiteScore = 8.43, Elsevier); handling editor of *Physics Open* (Elsevier); principal editor of *Journal of Materials Research* (MRS); associate editor of *Surface Innovations* (ICE); and editorial board member of *Scientific Reports*, *Journal of Materials Science and Technology*, and *Nano Materials Science.*

Alafara Abdullahi Baba is a Professor of Analytical/Industrial and Materials Chemistry in the Faculty of Physical Sciences, University of Ilorin, Nigeria. He holds a Ph.D. in Chemistry from the University of Ilorin (2008). His dissertation entitled "Recovery of Zinc and Lead from Sphalerite, Galena and Waste Materials by Hydrometallurgical Treatments" was judged the best in the area of Physical Sciences at the University of Ilorin, Nigeria in 2010. His area of research covers analytical, industrial, and materials chemistry in general with special interests in solid minerals and materials processing through hydrometallurgical routes; reactions in solution for metallurgical applications; preparation of phyllosilicates, porous, and bio-ceramic materials; ore beneficiation including indigenous barite processing for oil and gas applications with developing eco-friendly-cum-low energy synthetic routes for industrial, technological utilities, among others.

Professor Alafara has been cited in many international acclaimed journals of high impact. As an academically inclined scholar with many distinct awards, several of his research breakthroughs of more than 135 publications have been presented at both national and international conferences and workshops for wider recognition. His Unilorin 198th Inaugural Lecture (2021) "Sustainable National Development: Mineral and Material Resources to the Rescue" affirmed the use of locally sourced minerals for industries, a condition for countries to save a significant of foreign earnings.

Professor Alafara has occupied various positions as a chairperson, secretary, and member of relevant academic and professional committees. He was Head, Department of Industrial Chemistry of the University of Ilorin between 2017–2020; Deputy Director, Central Research Laboratories (2014–2017); University of Ilorin Senate Representative for Students' Disciplinary Committee (2019–present); Secretary, Hydrometallurgy and Electrometallurgy Committee of the Extraction & Processing Division (2018–2021); Co-organizer of the Rare Metal Extraction & Processing Symposium and Lead Organizer, Energy Technologies & Carbon-dioxide Management Symposium (2021); Materials Characterization—Education Committee; EPD and Best Awards Committee Representatives and appointed EPD Council (Education Representative) of The Minerals, Metals and Materials Society (TMS), USA. He is also the current National Vice President of the Materials Science and Technology Society of Nigeria and Fellow of many professional societies including the Chemical Society of Nigeria and Materials Science and Technology Society of Nigeria.

He has supervised and is still supervising many undergraduate and postgraduate research works and is currently serving as an External Examiner to Postgraduate researchers in universities within and outside Nigeria.

Neale R. Neelameggham IND LLC, is involved in international technology and management consulting for metals and chemicals, thiometallurgy, energy technologies, soil reactor design with Agricoal, lithium-ion battery design, OrangeH2, rare earth oxides, and metal manufacturing.

He has more than 38 years of expertise in magnesium production and was involved in the process development of its startup company NL Magnesium to the present US Magnesium LLC, UT until 2011, during which he was instrumental in process development from the solar ponds to magnesium metal foundry. His expertise includes competitive magnesium processes worldwide and related trade cases.

In 2016, Dr. Neelameggham and Brian Davis authored the ICE-JNME award-winning paper "Twenty-First Century Global Anthropogenic Warming Convective Model." He is working on Agricoal® to greening arid soils, and at present energy efficient Orange hydrogen, and methane abatement. He authored the ebook *The Return of Manmade CO to Earth: Ecochemistry*, published through Smashwords in November 2018.

Dr. Neelameggham holds 16 patents and applications and has published several technical papers. He has served in the Magnesium Committee of the TMS Light Metals Division (LMD) since its inception in 2000, chaired in 2005, and since 2007 has been a permanent advisor for the Magnesium Technology Symposium. He has been a member of the Reactive Metals Committee, Recycling Committee, Titanium Committee, and Program Committee for LMD and LMD council.

Dr. Neelameggham was the Inaugural Chair, when in 2008, LMD and the TMS Extraction and Processing Division (EPD) created the Energy Committee and has been a Co-Editor of the Energy Technology Symposium through the present. He received the LMD Distinguished Service Award in 2010. As Chair of the Hydrometallurgy and Electrometallurgy Committee, he initiated the Rare Metal Technology Symposium in 2014 and has been a co-organizer to the present. He organized the 2018 TMS Symposium on Stored Renewable Energy in Coal.

Mingming Zhang is currently a principal consultant at Wood Mackenzie. He has more than 15 years of experience in the field of mining, mineral processing, smelting and refining, and materials engineering. Before joining Wood Mackenzie, Dr. Zhang held lead engineer position at ArcelorMittal Global R&D in East Chicago, Indiana. He obtained his Ph.D. in Metallurgical Engineering from The University of Alabama and his master's degree in Mineral Processing from the General Research Institute for Non-ferrous Metals in China. Prior to joining ArcelorMittal, he worked with Nucor Steel in Tuscaloosa, Alabama where he was a metallurgical engineer leading the development of models for simulating slab solidification and secondary cooling process. Dr. Zhang has conducted a number of research projects involving mineral beneficiation, thermodynamics and kinetics of metallurgical reactions, electrochemical processing of light metals, metal recycling, and energy-efficient and environmentally cleaner technologies. He has published more than 50 peer-reviewed research papers and he is the recipient of several U.S. patents. Dr. Zhang also serves as editor and reviewer for a number of prestigious journals including *Metallurgical and Materials Transactions A* and *B*, *JOM*, *Journal of Phase Equilibria and Diffusion*, and *Mineral Processing and Extractive Metallurgy Review*. Dr. Zhang has made more than 30 research presentations at national and international conferences including more than 10 keynote presentations. He was the recipient of the 2015 TMS Young Leaders Professional Development Award. He has served as conference/symposium organizer and technical committee chair in several international professional organizations including The Minerals, Metals & Materials Society (TMS), the Association for Iron & Steel Technology (AIST), and the Society for Mining Metallurgy & Exploration (SME).

Dirk E. Verhulst spent the last 40 years in practical process metallurgy research on both sides of the Atlantic, bringing a number of projects from the laboratory to the pilot scale, and a few to industrial implementation. He is presently an independent consultant in process metallurgy and energy efficiency.

Until the end of 2008, he was Director of Research at Altairnano in Reno, Nevada. He participated in the development of the Altair Lithium-ion Battery and was involved in the design and procurement of the manufacturing plant for the ceramic materials.

Over the period 2003–2008, he worked extensively on the Altair Hydrochloride TiO_2 Pigment Process and the operation of its pilot plant. The complex flow sheet included both hydrometallurgical and pyrometallurgical steps. Optimization of energy use was a key factor to make this new approach competitive.

From 1995 to 2000, he was Senior Development Engineer in BHP's Center for Minerals Technology at the same location in Reno. It is at BHP that the development of the hydrochloride TiO_2 pigment process was initiated. Other BHP projects included novel processes for nickel, cobalt, zinc, and copper.

Prior to 1995, he worked for 17 years in the research department of Umicore in Hoboken, Belgium. He was active in lead refining and in the hydrometallurgy of minor metals (indium, tellurium, selenium), but was mostly involved in the introduction of electric furnaces in lead smelting and slag cleaning. He tackled mathematical models and lab-scale experiments, ran pilot plants, and participated in the start-up of industrial operations.

Dr. Verhulst has a doctor of engineering science degree in extractive metallurgy from Columbia University, and a chemical engineering degree from the Free University of Brussels. He wrote and presented publications in the areas of hydrometallurgy, pyrometallurgy, nanomaterials, and environmental science. He holds several patents and patent applications.

Shafiq Alam is an Associate Professor at the University of Saskatchewan, Canada. He is an expert in the area of mining and mineral processing with profound experience in industrial operations, management, engineering, design, consulting, teaching, research, and professional services. As a productive researcher, he has secured 2 patents and has produced over 170 publications. He is the lead/co-editor of 11 books, and one of the editorial board members of two mining and mineral processing journals named *Minerals* (an Open Access Journal by MDPI) and the *International Journal of Mining, Materials and Metallurgical Engineering*. He is the winner of the 2015 Technology Award from the Extraction & Processing Division of The Minerals, Metals & Materials Society (TMS), USA.

With extensive relevant industry experience as a registered professional engineer, Dr. Alam has worked on projects with many different mining industries. He is an Executive Committee Member of the Hydrometallurgy Section of the Canadian Institute of Mining, Metallurgy and Petroleum (CIM). During 2015–2017, he served as the Chair of the Hydrometallurgy and Electrometallurgy Committee of the Extraction & Processing Division (EPD) of TMS. Currently, he is serving on the TMS-EPD Awards Committee. He is a co-organizer of many symposia at international conferences through CIM and TMS. Dr. Alam is one of the founding organizers of the Rare Metal Extraction & Processing Symposium at TMS. He was involved in organizing the International Nickel-Cobalt 2013 Symposium and TMS 2017 Honorary Symposium on applications of Process Engineering Principles in Materials Processing, Energy and Environmental Technologies. Dr. Alam was a co-organizer of the 9th International Symposium on Lead and Zinc Processing (PbZn 2020). He is also involved in organizing the Rare Metal Extraction & Processing Symposium, co-located with the TMS 2022 Annual Meeting and Exhibition in Anaheim, California.

Part I
Renewable Energy and Combustion Technologies

Development of a Thermodynamic Model for Chromates, Molybdates, Tungstates, and Vanadates Involved in the Corrosion of Steels (Fe, Cr, Ni, Mo, W, and V) at High Temperatures in Atmospheres Containing O–H–S–C–Cl and Alkaline Salts

Sara Benalia, Christian Robelin, and Patrice Chartrand

Abstract This research work falls under the generic theme of modeling high-temperature processes, during energy conversion, flaking, and corrosion phenomenon, for systems converting mainly organic matter into energy. Energy conversion facilities are made of a metal alloy of the type Fe–Cr–Ni–V–Mo–W and are exposed to gaseous species from combustion, or from the flying of ashes. Under certain conditions, highly corrosive molten salts may be formed, causing the protective oxide layer of the steel to be transformed into either chromates, molybdates, tungstates or vanadates, or their mixture. This is called "catastrophic" corrosion. The presence of ash deposits limits the maximum operating temperature and the energy efficiency of the process. Thus, this research aims to develop a thermodynamic model including chromates, molybdates, tungstates, and vanadates that may form in environments containing O–H–S–C–Cl and alkaline salts, to predict the limiting conditions at which ash deposition and corrosion can occur.

Keywords Thermodynamic modeling · Energy conversion processes · Molten salts · Alkaline salts

Introduction

In this context, our research focuses on the high-temperature modeling of "hot corrosion" products (600–950 °C) in combustion energy conversion processes. This phenomenon occurs most often in combustion furnaces, coal gasification, or biomass

---

S. Benalia (✉) · C. Robelin · P. Chartrand
Centre for Research in Computational Thermochemistry (CRCT), Department of Chemical Engineering, Polytechnique Montréal, Station Downtown, Box 6079, Montréal, QC H3C 3A7, Canada
e-mail: sara.benalia@polymtl.ca

F. Tesfaye et al. (eds.), *REWAS 2022: Energy Technologies and CO_2 Management (Volume II)*, The Minerals, Metals & Materials Series,
https://doi.org/10.1007/978-3-030-92559-8_1

conversion units and recovery boilers. The major challenge for manufacturers is to maximize the energy efficiency of these processes [1–12].

To do this, the fuel should be burned with excess oxygen under conditions of high steam pressure and temperature. On the other hand, this trend, which targets such operating conditions, accelerates the risk of corrosion, which consequently limits energy efficiency gains [1–12].

Hot corrosion manifests itself specifically on the coldest parts of installations, where the water vapor circulating under pressure is heated by heat exchange with combustion gases such as furnace walls, tubes of parts of thermal power plants, and steam generators [13].

Environmental corrosiveness is largely related to the amount of air that must be available for combustion and the nature of the fuel used containing impurities (S, Cl, Na, K, V, Zn, Pb, etc.), thus determining the compositions of gases and ashes [12, 14–16]. High-temperature corrosion is usually the result of a combination of oxidation and sulfuration. Indeed, fly ash or alkaline salts can adhere to the metal walls, thus forming deposits.

This results in a change in the chemical potential of the environment at its interface with the metal. Due to the contact of oxygen and sulfur, the deposit has the effect of decreasing the oxygen potential and increasing the sulfur potential, which will prevent the formation of a protective and durable oxide layer [12]. The formation of these types of deposits, often rich in salts, increases the risk of corrosion and even more so when they become liquid, since they can dissolve the protective oxides and attack the metal surface.

Case Study of a Corrosion Problem in the Manufacture of Pulp by the Kraft Process

Figure 1 shows a representative case of corrosion that occurs during pulp manufacturing, mainly at the recovery boiler. This corrosion phenomenon is due to either molten salts or corrosive gases [9]. Figure 1 includes the main reactions that occur in a recovery boiler as well as their location.

The problems caused by corrosion in recovery boilers are complex. Indeed, the burned black liquor regenerates mainly mixtures of the molten salts Na_2CO_3 and Na_2S in the bottom of the furnace on the hearth [17]. The particulate residues during the combustion of the black liquor are mainly mixtures of sodium sulfate, sodium carbonate, and sodium chloride [18].

On the other hand, the reduction of sulfur to sulfide also produces hydrogen sulfide, small amounts of which may escape with the flue gases when the air supply is insufficient or when the air mixing in the furnace is incomplete. Large instantaneous emissions of hydrogen sulfide can occur as a result of deposits falling from the furnace walls [19].

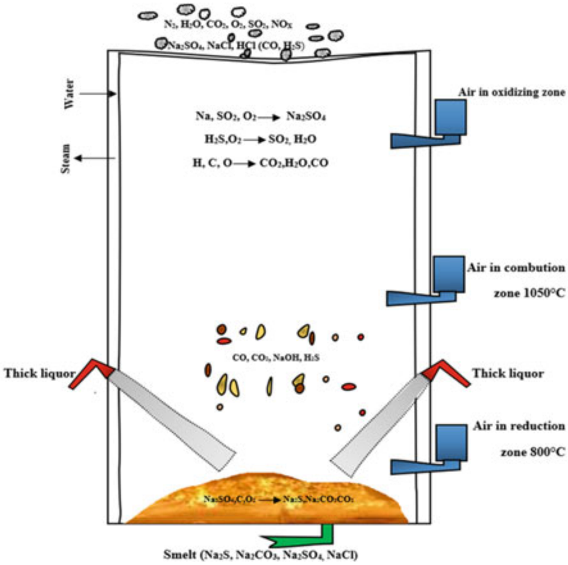

Fig. 1 Chemical reactions in a recovery boiler (inspired from reference [19])

In the upper part of the tubes and in the superheater, corrosion is mainly due to gases containing water vapor, carbon dioxide, oxygen, some hydrogen sulfide H_2S, and sulfur dioxide SO_2 [17]. Sulfur dioxide reacts with sodium in the gas phase to form sodium sulfate.

Since the higher dry matter content of the black liquor leads to an increase in temperature in the furnace, there is a decrease in hydrogen sulfide emissions and an increase in sodium emissions.

The sulfide bound in greater quantities to the sodium sulfate form therefore induces a decrease in the sulfur dioxide emissions [19].

Context of Investigation

The formation of volatile ash and corrosive gases is mainly due to the elements K, Na, Ca, Mg, Fe, Al, Si P, S, Cl, C, H, and O [14, 15]. These elements, in an incinerating environment, can form complex ionic liquids, molten salts as well as multicomponent gases. A chemical analysis of the solid deposits formed on the heat exchangers revealed the presence mainly of KCl, K_2CO_3, and K_2SO_4 as well as small amounts of NaCl, Na_2CO_3, and Na_2SO_4.

Presently, there are models that can predict the melting properties of K^+, Na^+ || Cl^-, SO_4^{2-}, and CO_3^{2-} mixtures with good accuracy [16]. However, thermodynamic models for chromates, molybdates, tungstates, and vanadates are still lacking.

We will focus on developing such models relevant for the corrosion of Fe, Cr, Ni, Mo, W, and V steels in contact with oxygen, hydrogen, sulfur, carbon, chlorine, and alkaline salts (KCl, K_2SO_4, NaCl, Na_2SO_4, etc.). We will consider the system K^+, Na^+ || Cl^-, SO_4^{2-}, CO_3^{2-}, (CrO_4^{2-}, $Cr_2O_7^{2-}$), (MoO_4^{2-}, $Mo_2O_7^{2-}$), (WO_4^{2-}, $W_2O_7^{2-}$), and O^{2-} including in particular chromates, molybdates, and tungstates. The two anions $\mathbf{VO_4^{2-}}$ and $\mathbf{V_2O_7^{2-}}$ related to vanadate-based corrosion will not be included in our model since the corresponding literature on corrosion mechanisms as well as the thermodynamic data required for calibration are extremely limited.

The developed thermodynamic model will permit to predict the boundary conditions under which corrosive deposits can occur and avoid their formation, so as to preserve the facilities, and optimize the energy conversion rate while increasing temperature (reduction of the burned fuel consumption for the same energy efficiency). The main challenge is to avoid the fusion of ash deposits which is favored by higher temperatures.

Corrosion Related to Alloying Elements (Cr, Mo, W, and V)

Chromates

Thermodynamic model of 6^+ oxidation state of chromium takes into account the presence of the following compounds: K_2CrO_4, Na_2CrO_4, $K_2Cr_2O_7$, and $Na_2Cr_2O_7$. Indeed, the interaction of KCl or NaCl from combustion processes with the protective layer of Cr_2O_3 generates a whole sequence of corrosion reactions forming K_2CrO_4 and Na_2CrO_4 [7, 10] according to:

$$24\mathrm{KCl(s)} + 10\mathrm{Cr_2O_3(s)} + 9\mathrm{O_2(g)} = 12\mathrm{K_2CrO_4(s)} + 8\mathrm{CrCl_3(s)}$$

$$2\mathrm{Cr_2O_3(s)} + 8\mathrm{NaCl(s)} + 5\mathrm{O_2(g)} = 4\mathrm{Na_2CrO_4(s)} + 4\mathrm{Cl_2(g)}$$

During the reaction, chromium oxide converts to sodium chromate (Na_2CrO_4) or potassium chromate, which results in further oxidation of chromium from state III to VI [2]. In addition, the protective oxide will be affected by the emitted chloride, which attacks the steel aggressively [4].

Potassium dichromate ($K_2Cr_2O_7$) is formed as a result of the interaction of KCl with Cr [2]. The latter is involved in the formation of eutectic mixtures with K_2CrO_4 and KCl [2]. The melting temperatures of these mixtures are even lower than the melting points of the pure compounds. Therefore, their presence induces the dissolution of the Cr_2O_3 protective film in the form of chromate or dichromate ions (${CrO_4}^{2-}$ or ${Cr_2O_7}^{2-}$) [2].

Molybdates

Studies by [8, 20] have highlighted the effects of Mo on the hot corrosion of superalloys. The formation of Na_2MoO_4 and a molten mixture of Na_2MoO_4-MoO_3 causes catastrophic corrosion. The mechanism of the latter remains unclear [21].

Leslie and Fontana [22] investigated the oxidation of Fe-25Ni-16Cr-6Mo (Mo > 3%) nickel-based superalloys at 900 °C and noted that the corrosion of steel had been catastrophic, with a significant accumulation of MoO_3 gas on the metal surface.

Further studies revealed that MoO_3 combines with Na_2SO_4 to produce an acidic SO_2-rich salt, generating an acidic flux at the deposit/metal interface.

In addition, the evidence of Na_2MoO_4–MoO_3 and Na_2MoO_4–$2MoO_4$ liquid solutions, indicates that those exhibit high Cr_2O_3 solubility [8].

Tungstates

Catastrophic corrosion can also originate from Na_2WO_4 [21], which leads to the self-sustained acidic dissolution of the protective oxide layer when the salt film contains WO_3 (a strongly acidic oxide).

Vanadates

Dissolution of Cr_2O_3 protective layers can occur in the presence of molten vanadium-based deposits. This is because V_2O_5 is a strongly acidic oxide that can promote the automatic dissolution of the protective oxide [9].

Oxides forming acidic solutes of much higher solubility in the presence of vanadates would lead to more rapid attack by molten sulfate-vanadate mixtures than by molten sulfate [10].

Strategy and Description of Our Methodology

Thermodynamic models allow to better investigate the chemistry of ash deposits and heat exchanger alloys, since the combined ash/gas/alloy chemistry controls the melting behaviour of ashes.

For this purpose, a thorough literature review on chromates, molybdates, tungstates, and vanadates was carried out for pure compounds, and binary, ternary, quaternary, and reciprocal (i.e. systems with two or more cations and two or more anions) sub-systems to gather the available data from the literature, and to perform thermodynamic optimizations. We have identified and collected all relevant articles containing experimental data that can be used for the calibration of the thermodynamic model (phase equilibria, heat contents, heat capacities, etc.).

The most reliable data have been identified and selected, and the thermodynamic properties of the following pure compounds have been estimated: Na_2CrO_4, K_2CrO_4, $Na_2Cr_2O_7$, $K_2Cr_2O_7$, Na_2MoO_4, K_2MoO_4, $Na_2Mo_2O_7$, $K_2Mo_2O_7$, Na_2WO_4, K_2WO_4, $Na_2W_2O_7$, and $K_2W_2O_7$.

The Modified Quasi-Chemical Model in the Quadruplet Approximation [23–26] is used for the liquid phase; it simultaneously considers the short-range order between first-nearest neighbours (cation/anion) and between second-nearest neighbours (cation/cation and anion/anion). The Compound Energy Formalism (CEF) [27, 28] is used to model the solid solutions. A CALPHAD (CALculation of PHAse Diagrams) approach is adopted (see Fig. 2): the model equations allow to describe the Gibbs energy of every phase as a function of temperature and composition.

Predictions can be made for the multicomponent system of interest from the model parameters obtained for the binary sub-systems (and possibly also the ternary and ternary reciprocal sub-systems) using appropriate interpolation techniques. Thermodynamic properties and phase equilibria are calculated using the FactSage thermochemical software, which includes a Gibbs energy minimization algorithm.

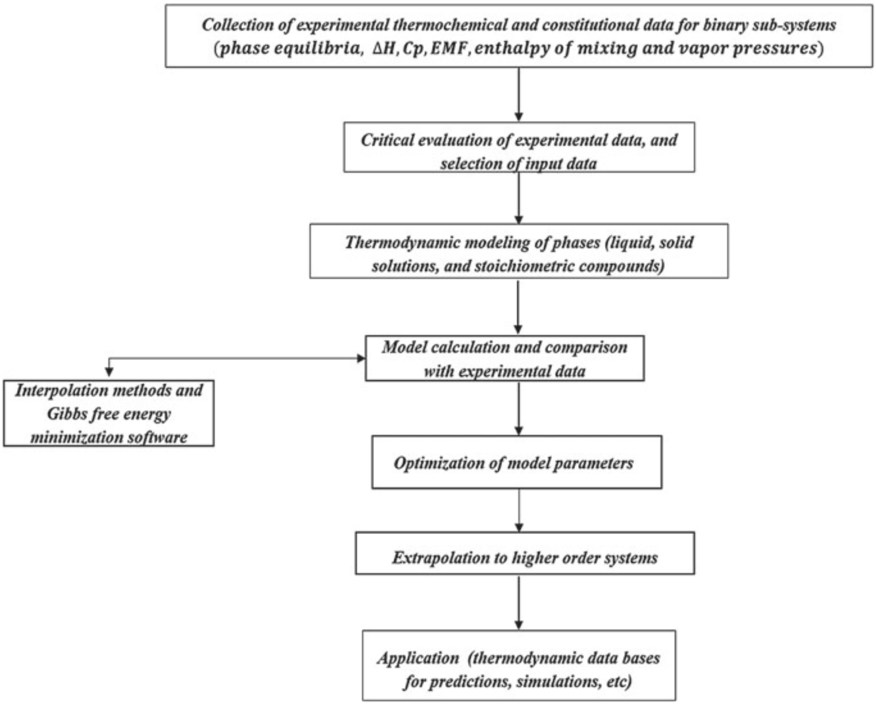

Fig. 2 Flowchart representing the core of the CALPHAD method [29, 30]

For some systems, there are limited or no data available in the literature, or sometimes conflicting data. Therefore, additional experiments are required in order to be able to best calibrate the thermodynamic model.

Experiments are in progress at Åbo Akademi Process Chemistry Centre (Turku, Finland) until the end of April 2022. The number of experiments that can be conducted will depend on the restrictions related to the COVID-19 pandemic and on the accessibility of the DSC/DTA apparatuses. XRD and DTA/DSC measurements are being performed for the relevant **pure compounds** A_2MO_4 and $A_2M_2O_7$ (with A = Na or K, and M = Cr, Mo, or W). For a given compound, the crystal structures of the various allotropes will be determined by XRD, thus permitting to define properly the various solid solutions (in binary and higher-order systems), and DSC/DTA will permit to measure the temperatures and enthalpies of the solid–solid transitions as well as the temperature and enthalpy of fusion.

Thereafter, DSC/DTA measurements will be conducted for the relevant binary sub-systems and ternary (common-cation, or ternary reciprocal with Na^+, K^+ and 2 different anions) sub-systems. Systems involving chromates, molybdates, or tungstates are being prioritized since reactions of the type $2A_2MO_4 = A_2M_2O_7 + A_2O$ (with A = Na or K, and M = Cr, Mo, or W) are calculated to be very limited. Then, predictions can be made in higher-order sub-systems from the corresponding optimized binary model parameters.

Results

As an example, Fig. 3 shows the calculated Na_2CO_3–Na_2CrO_4 phase diagram along with the available data from the literature. The two compounds Na_2CO_3 and Na_2CrO_4 have several allotropes; the high-temperature forms both have the same crystal structure (hexagonal) with the same space group ($P6_3/mmc$) [31, 32].

Thus, the experimental eutectic plateau observed over a wide composition range corresponds to a solid solution miscibility gap (that is, the formation of two solid solutions with the same crystal structure, and different compositions).

Summary and Conclusions

The relevance and original contributions of this project consist in the development of a new thermodynamic model applicable to a wide range of problems mentioned previously, in particular, related to combustion energy conversion.

The thermodynamic model developed by including chromates, molybdates, and tungstates will permit researchers to better understand the phenomenon of catastrophic corrosion and avoid the formation of a corrosive liquid phase. Indeed, the predictive capability of the model will be fully employed, allowing to optimize

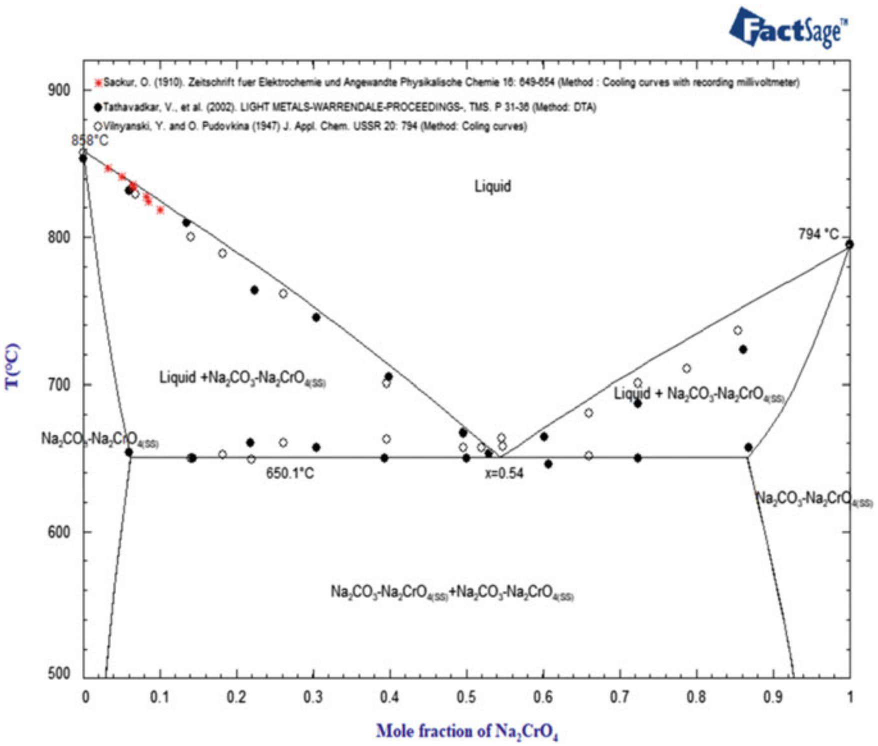

Fig. 3 Calculated Na_2CO_3-Na_2CrO_4 phase diagram

the operating parameters and improve the efficiency (energy and environmental) of various industrial processes.

Additionally, this model will permit to calculate all thermodynamic properties (especially phase equilibria) in every sub-system of the multicomponent system of interest $K^+, Na^+ \parallel Cl^-, SO_4^{2-}, CO_3^{2-}, (CrO_4^{2-}, Cr_2O_7^{2-}), (MoO_4^{2-}, Mo_2O_7^{2-})$ and O^{2-}.

Conflict of Interest The authors declare that they have no conflict of interest.

References

1. Paneru M et al (2013) Corrosion mechanism of alloy 310 austenitic steel beneath NaCl deposit under varying SO_2 concentrations in an oxy-fuel combustion atmosphere 27(10):5699–5705
2. Lehmusto J et al (2012) Studies on the partial reactions between potassium chloride and metallic chromium concerning corrosion at elevated temperatures. Oxid Met 77(3–4):129–148
3. Goebel J, Pettit F, Goward G (1973) Mechanisms for the hot corrosion of nickel-base alloys. Met Trans 4(1):261–278

4. Küpper J, Rapp R (1987) Oxidation/reduction reactions of molybdate ions in sodium sulfate at 1200 K. Mater Corros 38(11):674–682
5. Shinata Y (1987) Accelerated oxidation rate of chromium induced by sodium chloride. Oxid Met 27(5–6):315–332
6. Lindberg D et al (2006) Thermodynamic evaluation and optimization of the (Na+ K+ S) system. J Chem Thermodyn 38(7):900–915
7. Hazi M (2006) Processus d'interaction corrosion/érosion/dépôt dans les enceintes de traitement thermique des déchets
8. Pettit F et al (1984) Oxidation and hot corrosion of superalloys. Superalloys 85:651–687
9. Otsuka N, Rapp RA (1990) Effects of chromate and vanadate anions on the hot corrosion of Preoxidized Ni by a thin fused Na_2SO_4 film at 900° C. J Electrochem Soc 137(1):53–60
10. Eliaz N et al (2002) Hot corrosion in gas turbine components. Eng Fail Anal 9(1):31–43
11. Stringer and Technology (1987) High-temperature corrosion of superalloys. Mater Sci Technol 3(7):482–493
12. Antoni L, Galerie AJ (2003) Corrosion sèche des métaux. Cas industriels: dépôts, milieux fondus 10(M4227):M4227
13. François Armanet GB, Moulin G (2012) Corrosion par les gaz à haute température des métaux et alliages réfractaires. Technique de l'ingénieur, no COR378, pp 1–37
14. Huntz A-M, Pieraggi B (2003) Oxydation des matériaux métalliques: comportement à haute température, éd: Hermes-Lavoisier
15. Lacombe P, Dabosi F (1987) Les Ulis, Corrosion des Matériaux à Haute Température
16. Lindberg D (2007) Thermochemistry and melting properties of alkali salt mixtures in black liquor conversion processes. Åbo Akademi University
17. Remeau J-J, H Barthelemy and Techniques (1978) Quelques problèmes de corrosion dans la fabrication de la pâte à papier par le procédé kraft. Mater Techn 66(11–12):383–385
18. Lindberg D et al (2013) Towards a comprehensive thermodynamic database for ash-forming elements in biomass and waste combustion—current situation and future developments. Fuel Process Technol 105:129–141
19. Pöyry J (1992) Reduction of atmospheric emissions from pulp industry, on behalf of Swedish EPA
20. Fryburg G, Kohl F, Stearns C (1984) Chemical reactions involved in the initiation of hot corrosion of IN-738. J Electrochem Soc 131(12):2985–2997
21. Misra A (1986) Mechanism of Na_2SO_4-induced corrosion of molybdenum containing nickel-base superalloys at high temperatures I: corrosion in atmospheres containing only. J Electrochem Soc 133(5):1029–1038
22. Peters K, Whittle D, Stringer J (1976) Oxidation and hot corrosion of nickel-based alloys containing molybdenum. Corros Sci 16(11):791–804
23. Pelton AD et al (2000) The modified quasichemical model I—binary solutions. Metall Mater Trans B 31(4):651–659
24. Pelton AD, Chartrand P (2001) The modified quasi-chemical model: Part II. multicomponent solutions Metall Mater Trans A 32(6):1355–1360
25. Chartrand P, Pelton AD (2001) The modified quasi-chemical model: Part III. two sublattices Metall Mater Trans A 32(6):1397–1407
26. Pelton AD, Chartrand P, Eriksson G (2001) The modified quasi-chemical model: Part IV. two-sublattice quadruplet approximation Metall Mater Trans A 32(6):1409–1416
27. Hillert M, Jansson B, Sundman B (1988) Application of the compound-energy model to oxide systems/anwendung des compound-energy. Modells auf Oxidsysteme. Int J Mater Res 79(2):81–87
28. Sundman B, Ågren J (1981) A regular solution model for phases with several components and sublattices, suitable for computer applications. J Phys Chem Solids 42(4):297–301
29. Cacciamani G (2016) An introduction to the calphad method and the compound energy formalism (CEF). Technol Metal Mater Miner 13(1):16–24
30. Kumar KH, Wollants P (2001) Some guidelines for thermodynamic optimisation of phase diagrams. J Alloys Compd 320(2):189–198

31. Lindberg D, Backman R, Chartrand P (2007) Thermodynamic evaluation and optimization of the (Na_2CO_3+ Na_2SO_4+ Na_2S+ K_2CO_3+ K_2SO_4+ K_2S) system. J Chem Thermodyn 39(6):942–960
32. Goldberg A, et al (1973) Phase diagram and crystallography of the system Na_2CrO_4–K_2CrO_4. N Jb Miner Mh 241–252

Copper in Biomass Fuels and Its Effect on Combustion Processes

Fiseha Tesfaye, Daniel Lindberg, Mykola Moroz, Mikko Hupa, and Leena Hupa

Abstract The role of Cu-based phases in combustion processes has boldly emerged with the drastic increase in waste combustion, initiating the need to update thermodynamic databases for a better understanding and control of problems arising at high temperature. In the present work, we have reviewed the content and sources of Cu in selected biomass fuels and ashes, and examined the mechanisms through which it affects combustion processes and the environment. Phase equilibria and thermodynamic properties of phases in the CuCl-$CuSO_4$ system and their effects on the melting behavior of chlorides and sulfates of Na, K, Cu, Pb, Zn, and Fe were investigated. The observed results are presented and discussed.

Keywords Renewable fuels · Copper · Eutectic melt formation · High temperature · Thermochemical data

Introduction

The major greenhouse gas emissions come from the energy sector globally. Increasing the generation of energy from renewable resources in different economic sectors is essential to protect the environment. Solid biomass, municipal waste, and industrial waste utilization for energy generation is one of the options available for reducing the use of fossil fuels. Furthermore, in an attempt to increase self-sufficiency

---

F. Tesfaye (✉) · M. Hupa · L. Hupa
Johan Gadolin Process Chemistry Centre, Åbo Akademi University, 20500 Turku, Finland
e-mail: fiseha.tesfaye@abo.fi

D. Lindberg
Department of Chemical and Metallurgical Engineering, Aalto University, 02150 Espoo, Finland

M. Moroz
Department of Chemistry and Physics, National University of Water and Environmental Engineering, Rivne 33028, Ukraine

Department of Physical and Colloid Chemistry, Ivan Franko National University of Lviv, Lviv 79005, Ukraine

F. Tesfaye et al. (eds.), *REWAS 2022: Energy Technologies and CO_2 Management (Volume II)*, The Minerals, Metals & Materials Series,
https://doi.org/10.1007/978-3-030-92559-8_2

in energy, fossil fuel importing countries have been planning to enhance energy generation from renewable resources and improve existing renewable-energy power plants. One of the driving forces to enhance the usage of renewable-energy sources is the target set by the European Union (EU) [1]. In biomass-rich countries such as Finland, the energy produced from wood-based fuels (solid biomass) accounted for >25% of the total energy consumption in 2020 [2]. A large share of this energy comes from the forest industry's byproducts, including bark, black liquor, and sawdust. In 2019, the share of solid biomass in the heating sector of the EU was about 17% [3]. Combustion of biomass for heat and electricity is generally carried out in large industrial combustors such as fluidized bed boilers and grate-fired boilers.

In biomass combustion processes, alkali metal elements in the biomass fuels and the ash fusion behavior are the two main factors contributing to fouling and slagging during high-temperature processing. These fouling and slagging problems threaten the long-term operational availability and economics of power plants [4–6]. For instance, renewable-energy power plants built recently in Northern China have to shut down for cleaning the boiler almost every month because of the fouling in the intermediate-temperature superheaters [6, 7]. Problematic low-temperature fouling also often occurs on or near the bag filters of some boilers [7]. One of the main effects of the formation of slagging and fouling deposits is that they reduce the heat transfer process between the flame side and the water steam side and accelerate corrosion and erosion on the surfaces of superheaters and boiler tubes. These deposits also result in an increase in the flue gas temperature that reduces the efficiency of the plant system and increases corrosion and erosion problems in the boilers [8, 9]. Corrosion control is considered as a piece of a big puzzle for the economics of power plants; controlled corrosion minimizes the need for tube replacement (reduced maintenance cost), minimizes plant shut-down frequencies, and maintains a good level of plant efficiency during operations [8].

A high alkali metal concentration in renewable fuels is known to result in the formation of compounds with low melting temperatures. Considerable amounts of the highly corrosive alkali chlorides in the flue gases are agglomerated in these processes [10]. The main objective of this work is to review the content of copper in biomass and waste-derived fuels and their ashes, and examine mechanisms through which copper affects combustion processes, including deposition/melt formations and environmental aspects. Effects of $CuCl_x$ and $CuSO_4$ on the other salts to induce melt formations are investigated.

Copper in Combustion Processes

As much as Cu plays a crucial role in modern society, it is considered problematic when it comes to combustion processes. Cu in biomass fuels exists as a trace metal. According to Vassilev et al. [11], Cu in various biomass ashes (ash samples generated under laboratory conditions) is typically around 100 ppm. The effect of

Cu in combustion processes has boldly emerged with the drastic increase in waste combustion.

Undesired copper levels in biomass combustion processes usually emanate from contaminations and co-firing with other fuels. In waste-derived fuel combustion processes, copper was reported to occur in oxidation states of zero, +I, and +II:

- the bed ash mainly contains a mix of Cu and Cu- oxides [12], and
- the cyclone ash may contain a mix of copper metal, Cu_2O, $CuCl_x$, $Cu(OH)_2$, and $CuSO_4 \cdot 5H_2O$ [12].

Copper halides are known to have a catalyst role in the formation of the environmentally harmful PCDD/F emissions in the *de novo* mechanism. The behavior of copper in fly ash in the oxychlorination cycle is illustrated in Fig. 1. $CuCl_2$ is an active catalyst compared to $CuSO_4$ [12]. This catalytic effect of Cu halides is the most intense in the lower temperature range 200–400 °C.

On the other hand, the relatively higher Cu contents in municipal solid waste incineration (MSWI) ash can be a potential source of metal recovery. Cu in different forms was reported up to 1 wt% in MSWI bottom ash, and around 1000 ppm in MSWI fly ash [14].

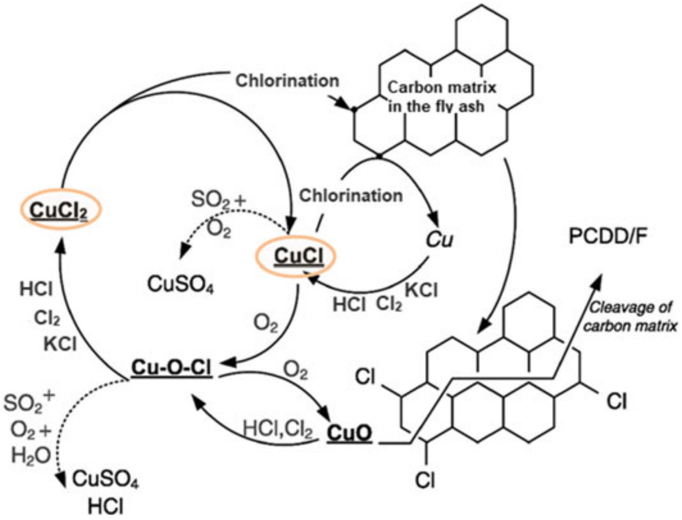

Fig. 1 The formation of PCDD/F (dioxins and furans) in the *de novo* mechanism catalyzed by $CuCl_x$, modified from [13]

Composition of Copper in Fuels and Ashes

The approximate concentration level of copper in softwoods and hardwoods (excluding carbon, hydrogen, nitrogen, and oxygen) is in the range of 1–10 ppm [15]. The average concentration of Cu in the inner and outer barks of birch, spruce, and pine is 2 ppm, with higher content in the outer surfaces [16].

The content of Cu in different biomass varies significantly; for example, wheat straw contains 0.06 ppm Cu [17], beech wood contains 43 ppm Cu [17], phyto remed from plants in contaminated sites contains 70 ppm Cu [18], sewage sludge contains 330 ppm Cu [19], chicken litter contains 71 ppm Cu [20], and paper sludge contains 310–450 ppm Cu [21, 22]. According to Saarela et al. [16], the pine bark obtained nearby the metal industry in Kokkola, Finland, contained about 515 ppm of Cu.

According to Grasso and Atkins [23], recycled wood fuels including telephone poles, pallets, and shipping containers can contain above 1000 ppm Cu. Their result indicates that waste-derived fuels contain a significantly higher concentration of Cu, compared to the <10 ppm concentration of Cu in non-recycled woody biomass. The main sources for copper in waste-derived fuels and ashes are:

- brass and copper wires;
- “impregnated wood”—CCA (Chromated copper arsenate ($CrAsO_4 + Cu_3(AsO_4)_2$));
- plastic catalyst and colorant; and
- pigments.

During combustion processes, all heavy metals except mercury are retained in the ash effectively [24]. However, the heavy metals including Cu are significantly enriched in the finer aerosol particles formed during combustion [25]. The partitioning of metals between the bottom ash and the fly ash depends on the type of furnace [26]. Thermodynamic equilibrium is attained in larger bottom ash particles from grate furnaces because of the length of exposure to high temperature of the particles. However, in fluidized beds, there is insufficient time for equilibrium, and mass transport effects dominate [24]. Table 1 shows the composition of copper in ashes of different fuels. The reported results also suggest a higher concentration of copper in the fly ashes than the bottom ash.

Results and Discussion

Thermodynamic Considerations in Combustion Processes

To avoid the liquid phase formations, phases and phase mixtures that lie along the solidus and liquidus lines must be determined. These data will also help to understand corrosion mechanisms on the superheater surfaces. When the composition of the feedstock is known, accurate data on the ash melting behavior together with furnace

Table 1 Concentration of copper in different types of ash

Fuel source of ash	Type of ash	Cu content (ppm)	Reference
Spruce wood	Ash samples generated under laboratory conditions, after combustion at 500 °C for 4 h in a muffle furnace	42.7	[27]
Beech wood		29.3	
Oak wood		37.9	
Spruce wood bark		16.1	
Beech wood bark		12.4	
Beech wood bark		12.6	
Boiler biomass	Bottom	12.8	[28]
		< 10.0	[29]
	Cyclone	31.6	[28]
	Filter	18.9	[28]
		60.0	[29]

gas temperature can help to identify the sticky temperature range, a temperature range in which fly ashes contain a certain amount of melt that leads to sticking and deposits build up on the surfaces of superheater and boiler tubes [30].

Copper Salts Containing Mixtures and Their Melting Behavior

The effect of CuCl on melt formation of Na-, K-, Cu-, Pb-, Zn-, and Fe- chlorides were investigated. Figure 2 shows how the melt-forming temperatures of the salts drop as the amount of CuCl increases in a binary mixture. For example, the melting temperature of KCl is 771 °C. In the presence of 22 mol.% CuCl, the melt-formation temperature drops to 550 °C.

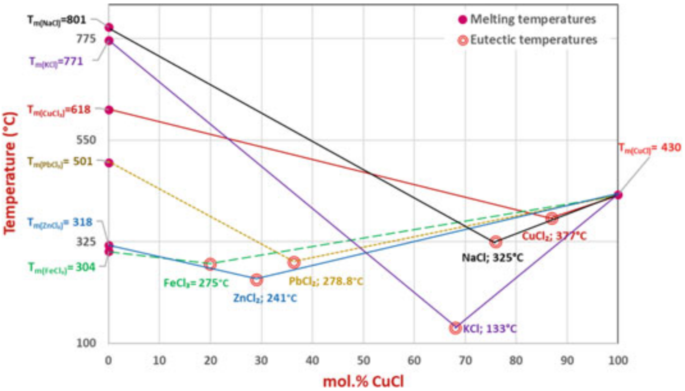

Fig. 2 Effect of CuCl on eutectic melt formations with Na-, K-, Cu-, Pb-, Zn-, and Fe- chlorides

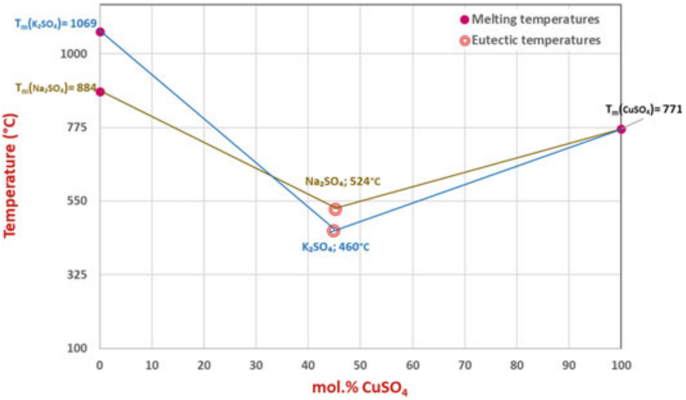

Fig. 3 Effect of $CuSO_4$ on the eutectic melt formations with K- and Na sulfates

The effect of $CuSO_4$ on the eutectic melt formation with sulfates of K and Na were investigated, and the results are presented in Fig. 3. As observed in the case of mixing CuCl with the other metal chlorides, adding $CuSO_4$ to the K- and Na- sulfates forms eutectic melt that drops the melting temperature of the mixtures significantly.

These mixture melt formations at a relatively lower temperature than the individual phases could favor the sticking of fly ashes on the surfaces of the superheater and boiler tubes, causing problematic deposit build-up that could eventually disrupt the combustion process.

Summary and Conclusions

In this paper, the amount of copper in selected fuels and ashes, environmental aspects of copper in the combustion processes, and the role of copper in undesired melt formations on the surfaces of boiler tubes were reviewed.

It has been observed that the average amount of copper in woody biomass fuels is between 0.5 and 10 ppm, in biomass ashes it is between 10 and 100 ppm, and in waste-derived fuel ashes it is between 1000 and 10,000 ppm. The main forms of copper in combustion processes are Cu, CuO_x, $CuCl_x$, and $CuSO_4$. Copper halides are observed to be highly volatile and suspected to be key catalysts for dioxin formation via the *de novo* mechanism. The catalytic effect is reported to be higher at low temperatures (200–400 °C).

The effect of CuCl and $CuSO_4$ on the melting behavior of commonly known chlorides and sulfates in combustion processes was examined, and all the studied phases were found to form eutectic melt with both Cu salts. The effect of CuCl on the low-temperature eutectic melt formation with KCl is the most significant.

Acknowledgements This work was partly supported by the Academy of Finland project (Decision number 311537), as part of the activities of the Johan Gadolin Process Chemistry Centre at Åbo Akademi University. The authors are also grateful to the national projects of the Ministry of Education and Science of Ukraine: "Synthesis, physico-chemical and thermodynamic properties of nano sized and nanostructured materials for electrochemical systems" (No. 0120U102184).

Conflict of Interest The authors declare that they have no conflict of interest.

References

1. European Commission (2009) Directive 2009/28/EC of the European parliament and of the council of April 23. http://data.europa.eu/eli/dir/2009/28/2015-10-05. Accessed on 14 Aug 2021
2. Official Statistics of Finland (OSF) (2021) Energy supply and consumption. http://www.stat.fi/til/ehk/2020/01/ehk_2020_01_2020-06-30_tie_001_en.html. Accessed on 31 Aug 2021
3. Schmidt-Baum T, Thrän D (2020) Nine measures to take—unlocking the potential for biomass heat in the german industry and the trade, commerce, and service sector. Energies 13(1–23): 4614
4. Vamvuka D, Zografos D, Alevizos G (2008) Control methods for mitigating biomass ash-related problems in fluidized beds. Bioresour Technol 99:3534–3544
5. Lindberg DK, Tesfaye F (2017) The thermodynamics of slag forming inorganic phases in biomass combustion processes. In: Zhang L, Drelich J, Neelameggham NR, Guillen DP, Haque N, Zhu J, Sun Z, Wang T, Howarter JA, Tesfaye F (eds) Energy technology 2017, TMS 2017. Springer, Cham, pp 27–41
6. Zhu Y, Niu Y, Tan H, Wang X (2014) Short review on the origin and countermeasure of biomass slagging in grate furnace. Front Energy Res 2:7
7. Niu Y, Tan H, Wang X, Liu Z, Liu Y, Xu T (2010) Study on deposits on the surface, upstream, and downstream of bag filters in a 12MWbiomass-fired boiler. Energy Fuels 24:2127–2132
8. Enestam S (2019) Ash related challenges from a boiler manufacturer's point of view: chemistry in energy technology 2019. http://users.abo.fi/maengblo/CET_2019/6_Ash%20related%20challenges%202019%20Enestam%20_rev.pdf. Accessed on 5 Sept 2021
9. Febrero L, Granada E, Regueiro A, Míguez JL (2015) Influence of combustion parameters on fouling composition after wood pellet burning in a lab-scale low-power boiler. Energies 8:9794–9816
10. Karlsson S, Åm L-E, Liske J (2015) Reducing high-temperature corrosion on high-alloyed stainless steel superheaters by co-combustion of municipal sewage sludge in a fluidised bed boiler. Fuel 139:482–493
11. Vassilev SV, Baxter D, Andersen LK, Vassileva CG (2013) An overview of the composition and application of biomass ash. Part 1: phase–mineral and chemical composition and classification. Fuel 105:40–76
12. Lassesson H, Steenari B (2013) Speciation of copper in ash from a fluidized-bed boiler fired with municipal solid waste. Energy Fuels 27:3891–3897
13. Takaoka M et al (2005) Dynamic change of copper in fly ash during de novo synthesis of dioxins. Environ Sci Technol 39:5878–5884
14. Lindberg D, Molin C, Hupa M (2015) Thermal treatment of solid residues from WtE units: a review. Waste Manage 37:82–94
15. Willför SR, Alén J, van Dan, Liu Z, Tähtinen M (2011) Raw materials. In: Fardim P (ed) Chemical Pulping Part 1. Porvoo, Finland, Paperi ja Pu Oy, pp 16–186
16. Saarela K-E, Harju L, Lill J-O, Rajander J, Lindroos A, Heselius S-J, Saari K (2002) Thick-target PIXE analysis of trace elements in wood incoming to a pulp mill. Holzforschung 56(4):380–387

17. Demirbaş A (2005) Influence of gas and detrimental metal emissions from biomass firing and co-firing on environmental impact. Energy Sources 27:1419–1428
18. Mellem JJ, Baijnath H, Odhav B (2009) Translocation and accumulation of Cr, Hg, As, Pb, Cu and Ni by Amaranthus dubius (Amaranthaceae) from contaminated sites. J Environ Sci Heal Part A 44:568–575
19. Werther J, Ogada T (1999) Sewage sludge combustion. Prog Energy Combust Sci 25:55–116
20. Abelha P, Gulyurtlu I, Boavida D, Seabra Barros J, Cabrita I, Leahy J, Kelleher B, Leahy M (2003) Combustion of poultry litter in a fluidised bed combustor. Fuel 82:687–692
21. Latva-Somppi J, Moisio M, Kauppinen EI, Valmari T, Ahonen P, Tapper U, Keskinen J (1998) Ash formation during fluidized-bed incineration of paper mill waste sludge. J Aerosol Sci 29:461–480
22. Rink KK, Kozinski JA, Lighty JS (1995) Biosludge incineration in FBCs: behaviour of ash particles. Combust Flame 100:121–130
23. Grasso T, Atkins RS (1991) The composition of recycled wood fuel: environmental permitting implications. In: 16th IGT conference, energy from biomass wastes Washington DC, pp 73–94
24. Nzihou A, Stanmore B (2013) The fate of heavy metals during combustion and gasification of contaminated biomass—a brief review. J Hazard Mater 256–257:56–66
25. Zeuthen JH, Jensen PA, Jensen JP, Livbjerg H (2007) Aerosol formation during the combustion of straw with addition of sorbents. Energy Fuels 21(2):699–709
26. Toledo JM, Corella J, Corella LM (2005) The partitioning of heavy metals in incineration of sludges and waste in a bubbling fluidised bed 2. Interpretation of results with a conceptual model. J Hazard Mater 126:158–168
27. Demirbaş A (2003) Toxic air emissions from biomass combustion. Energy Sources 25(5):419–427
28. Li L, Yu C, Bai J, Wang Q, Luo Z (2012) Heavy metal characterization of circulating fluidized bed derived biomass ash. J Hazard Mater 233–234:41–47
29. Dahl O, Nurmesniemi H, Pöykiö R, Watkins G (2009) Comparison of the characteristics of bottom ash and fly ash from a medium-size (32 MW) municipal district heating plant incinerating forest residues and peat in a fluidized-bed boiler. Fuel Process Technol 90:871–878
30. Tesfaye F, Lindberg D, Moroz M, Hupa L (2020) Investigation of the K-Mg-Ca sulfate system as part of monitoring problematic phase formations in renewable-energy power plants. Energies 13(1–12):5366

Synthesis Methods for Nanoparticle Morphology Control in Energy Applications

Joy Morin, Kiyo Fujimoto, Arin Preston, and Donna Post Guillen

Abstract Lightweight nano-composite materials, nano-coatings, nanocatalysts, and nano-structured materials have demonstrated an ability to reduce emissions and maximize clean energy production. Nanoparticles play an important role in engineering and decarbonization for energy applications, and a wide range of nanoparticle synthesis methods have been developed to include those that enable control over particle morphology. The ability to control nanoparticle morphology allows the tailoring and improvement of material properties that will accelerate efforts towards lowering carbon emissions by developing advanced catalysts for carbon sequestration and will enhance energy-efficient processes and technologies. Synthesis methods aimed towards shape control of nanoparticles have demonstrated an ability to form spheres, rods, flower-like shapes, cubes, plates, shells, and chiral geometries. Processing methods used to form these morphologies include microwave-assisted synthesis, solvothermal, hydrothermal, and a wide range of capping agents. A discussion of a few of these methods is given along with results and applications.

Keywords Nanoparticles · Morphology control · Synthesis · Decarbonization · Clean energy

Introduction

Nanoparticles are classified as "a particle that ranges from 1–100 nm in size [1]." Specific mechanical properties of a material, like stiffness, tensile strength, and hardness [2], vary and are determined by the size and shape of the nanoparticles [3]. Some common shapes that a nanoparticle can form are spheres (Fig. 1), rods (Fig. 1), flower-like shapes (Fig. 2), cubes (Fig. 3), plates (Fig. 4), shells (Fig. 5), and chiral geometries (Fig. 6). Although these shapes can naturally form, there are ways to control which shapes particles form. To intentionally achieve and control these shapes, shape-control processes must be used. Many shape-control methods

---

J. Morin · K. Fujimoto · A. Preston · D. P. Guillen (✉)
Idaho National Laboratory, Idaho Falls, ID 83415, USA
e-mail: Donna.Guillen@inl.gov

F. Tesfaye et al. (eds.), *REWAS 2022: Energy Technologies and CO_2 Management (Volume II)*, The Minerals, Metals & Materials Series,
https://doi.org/10.1007/978-3-030-92559-8_3

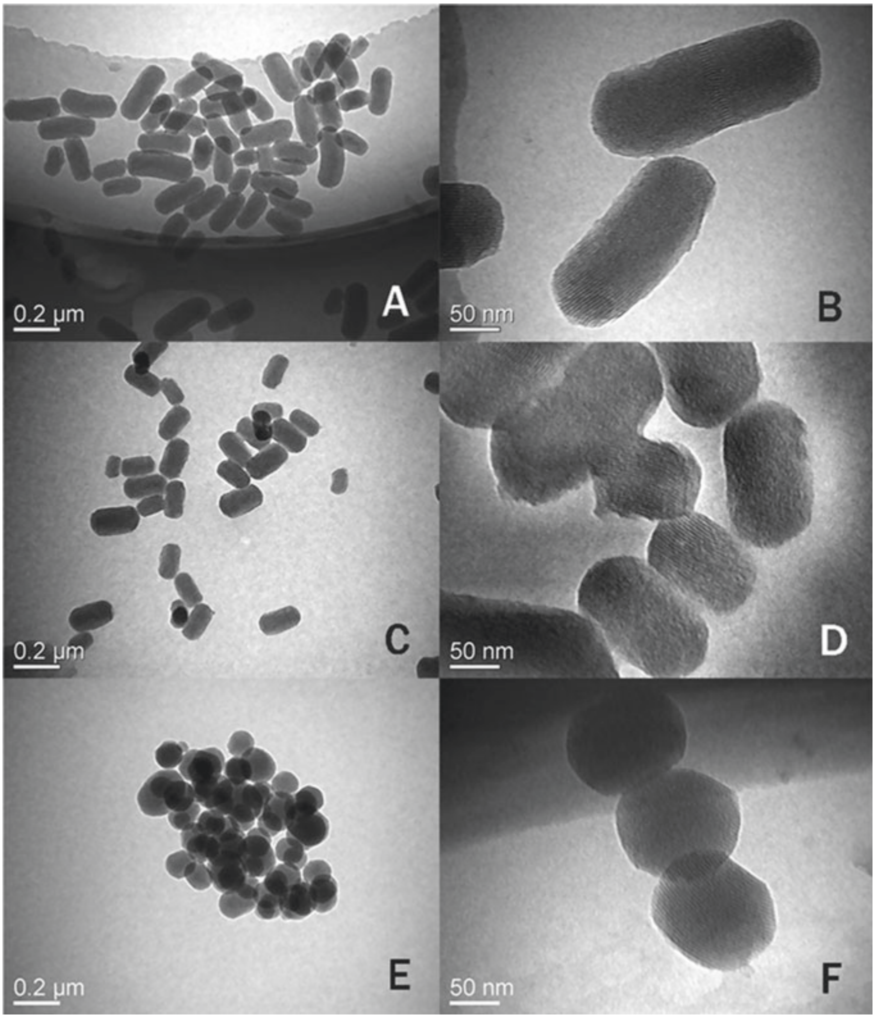

Fig. 1 Rod-shaped fluorescent mesoporous silica nanoparticles (**a**–**d**) and sphere-shaped fluorescent mesoporous silica nanoparticles (**e**–**f**) [26] Used under a Creative Commons CC-BY License

use a "bottom-up" approach, where the formation begins with atomic agglomeration, or by modification of simple "seed" particles, and builds up into a shaped particle. Such bottom-up methods proceed by atomic deposition in chemical, microwave, or thermal environments using supplied capping agents and precursors. When using a top-down approach, the shape is harder to control during synthesis [4]. In the top-down approach, the material is taken away to form a product which is more difficult to precisely control than synthesizing and building up material chemically. The top-down approach is also typically more expensive [5]. Both thermodynamics

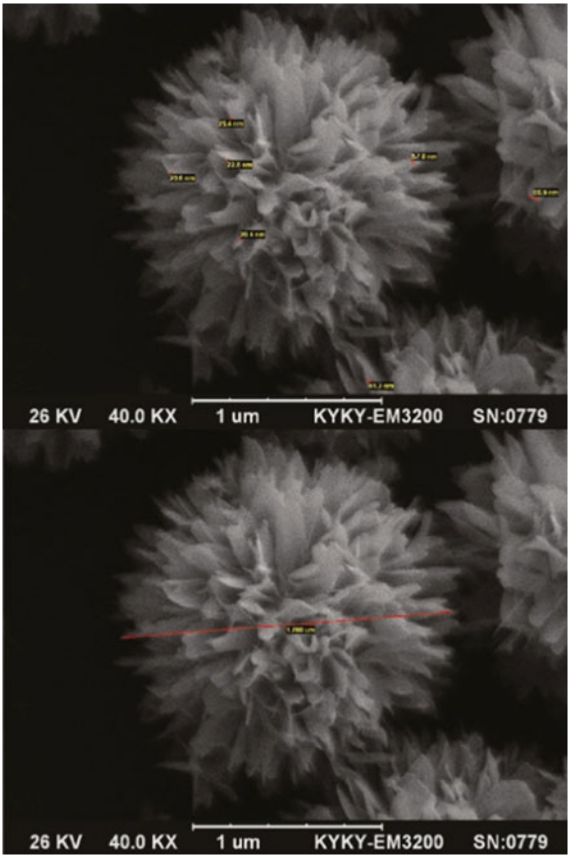

Fig. 2 Flower-like SEM images of PbS obtained in the presence of glucose (capping agent) [27] Used under Open Access Creative Commons Attribution-NonCommercial-NoDerivs 3.0 Unported license

and kinetics are driving forces in nanoparticle synthesis. Kinetics refers to a stabilized facet leading to the “most favorable pathway towards the final product,” while thermodynamics refers to said stabilized facets as leading “to the most stable final product [6].” During a thermodynamic process, the surface free energy of the particles decreases and forces the particle into a certain shape. Shape-control processes can use either thermodynamics, kinetics, or a combination of the two during synthesis [7]. The ability to control the shape of a particle provides numerous advantages such as self-assembly [8, 9], increased plasmonic absorbance [10], and improved catalytic activity [5, 11]. Multiple materials can be formed using shape synthesis. Metals and ceramics are synthesized for electronic improvements [12], clean energy applications [9, 13], and decarbonization efforts, among other applications [14].

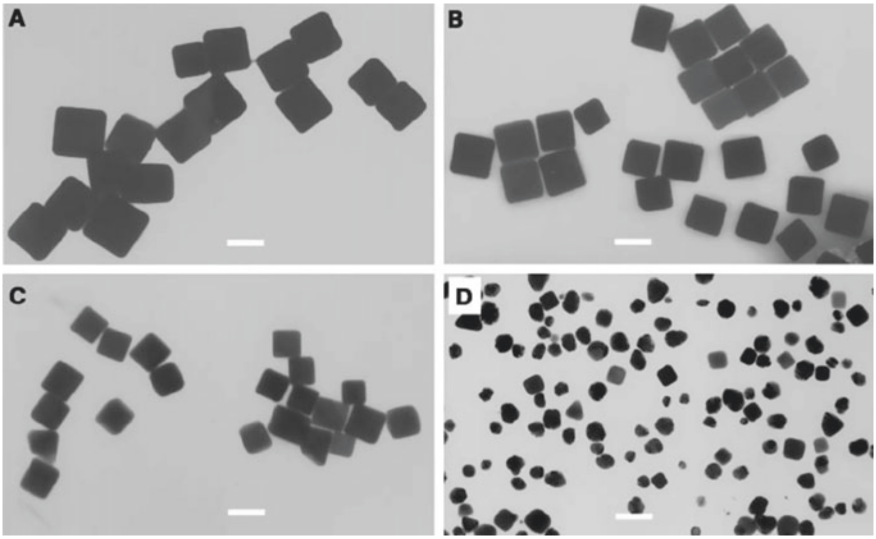

Fig. 3 Silver nanocubes synthesized at different growth times from [28]. Reprinted with permission from AAAS [28]

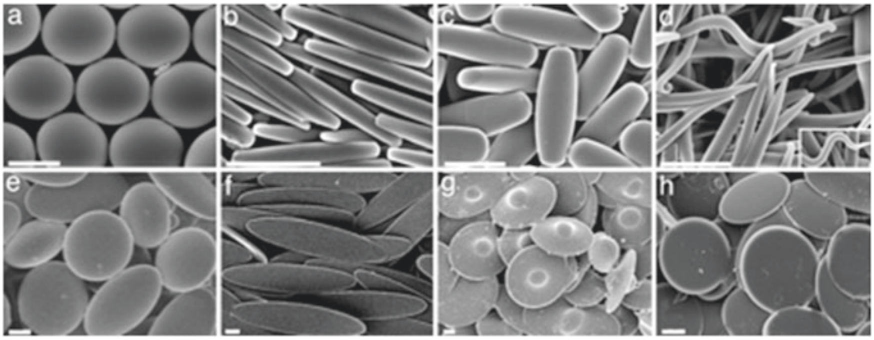

Fig. 4 Micrographs of shapes made by using scheme showing different platelet shapes (**e**, **f**, **g**, and **h**) from [29]. Copyright (2007) National Academy of Sciences, U.S.A. Reprinted with permission from PNAS [29]

Motivation

The ability to control nanoparticle shape during synthesis has several benefits. Things like carbon emissions [13], catalysis [5, 11], self-assembly [9], battery efficiency [12], and more can be improved. Although clean energy has made advances in the past, specific nanoparticle geometry can provide more benefits than before. "Shape… plays a major role in how particles are transported through a fluid, especially within narrow tubes [15]" which is the environment of nanofluids used for heating and

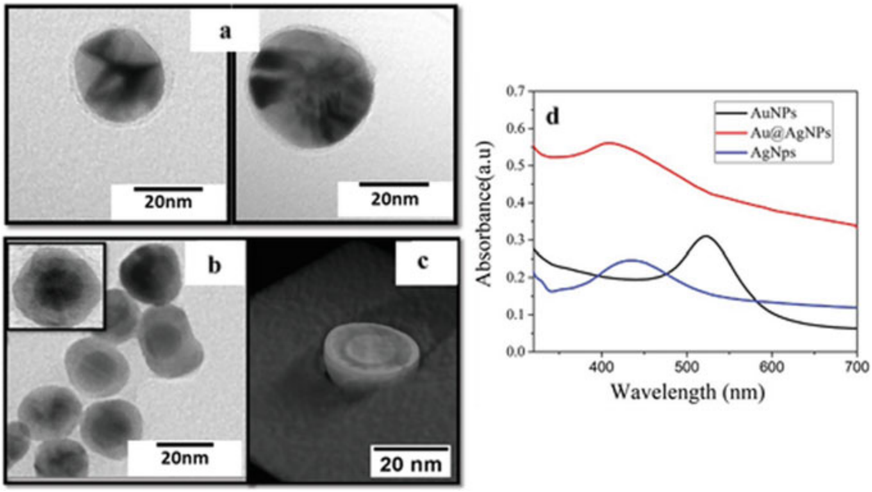

Fig. 5 **(a)–(c)** TEM images of Au@Ag (Core–shell bimetallic plasmonic NPs consisting of gold NPs as core material and silver as shell) nanoparticles showing shell geometry **(d)** UV-VIS absorbance spectrum [30] Used under the Creative Commons Attribution-NonCommercial-NoDerivs License

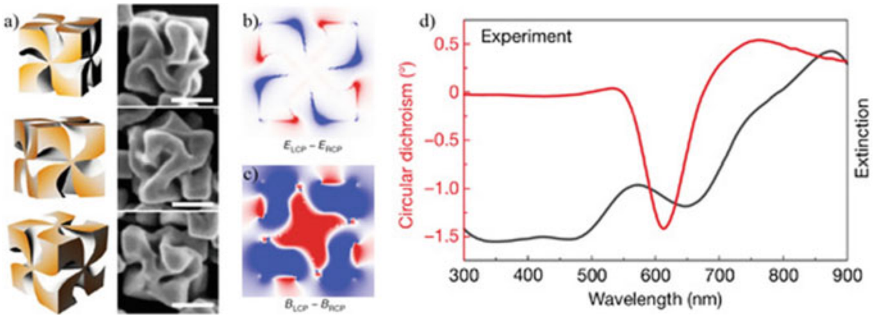

Fig. 6 **(a)–(b)** 3D and SEM images of nanoparticles with chiral geometry, **(c)** magnetic B near-fields, and **(d)** circular dichroism signals [31]. Used under the Creative Commons Attribution License

cooling systems. An example of how shape is important in decarbonization specifically can be seen in solar collection that takes advantage of nanoparticles [14]. Shapes with more sharp corners and edges can support larger plasmonic electric field enhancements than shapes without [10]. In another study by Zhu, W., et al., it was found that Pd nanoparticles with an octahedral shape showed higher CO selectivity (up to 95%) and better activity than Pd nanoparticles that were synthesized as cubes [16]. These Pd particles are used to reduce CO_2 into a synthesis gas. With higher CO selectivity, this process can be done more efficiently.

Catalysts are also a large part of the motivation for shape control. Different shapes of particles will have different surface facets. These surface facets will respond differently with other molecules and can lead to more efficient interaction with said molecule [5]. This will cause an increase in catalytic activity which can save time and energy by having a faster reaction that may not require something like heat to act as a catalyst. Catalysts play a major role in reducing carbon emissions. They can be used to convert carbon into other useful materials like alcohol, so the better the catalyst, the more carbon that can be converted. Catalysts can also be used in the production of hydrogen. With improved catalysts, water can be split in a renewable way to create hydrogen [11].

Another important factor of shape control is the promotion of self-assembly among the nanoparticles. When particles are in a certain shape like cubes, there is more self-assembly than other shapes like a sphere. This increased self-assembly can be used to create networks of nanoparticles that can help fabricate functional devices like catalysts [3]. Applications of these self-assembled networks include oil spill clean-up, toxic metal removal, and removal of dyes in water [9]. Because of the bottom-up formation of these nanonetworks, the pathways can be potentially controlled by programming molecular-scale information by simple organic synthesis [9]. Some of these self-assembled networks allow solid-like phases to interact with liquids, leading to the removal of pollutants in water.

Improving battery efficiency is another area benefitted by shape-control synthesis. A study by Seher, J., et al. showed that when $LiFePO_4$ nanoparticles had a plate-like shape, they showed an increase in electrochemical performance and fast-charging capability compared to nanoparticles with a rod-like shape [12]. This means that batteries using plate-like particles would have a faster charging time and improved reliability, leading to less wasted energy and less contribution to pollution.

Other energy efficiency improvements in electricity play a role in reducing carbon emissions while being affected by nanoparticle shape control. Thermoelectric power generation is a process that takes waste heat and converts it to usable electric power [13]. The conversion efficiency in this process can be improved based on the shape of nanoparticle used. In a study by Han, L., et al., Al-doped ZnO particles were synthesized into rods and platelets [13]. Platelets that had aligned laminar grains had a better conversion efficiency than the rods and other platelets synthesized, which would benefit the reduction of carbon emissions.

Methods and Outcomes

There are numerous ways to control the particle shape during nanoparticle synthesis. Four main types of synthesis exist under the umbrella of thermodynamics and kinetics including using different capping agents, microwave heat treatment, autoclave heat and pressure treatment, and using different solvents and precursors at different concentrations.

Capping agents not only provide stability to nanoparticles by preventing agglomeration of colloidal particles but also restrict their growth. Capping agents have a hydrophobic tail and a hydrophilic head that bond to the nanoparticles. Some capping agents that are used in nanoparticle synthesis include small ligands, surfactants, polysaccharides, cyclodextrins, polymers, and dendrimers [17]. One way that capping agents are used is in creating electrocatalysts to increase the efficiency of polymer electrolyte fuel cells (PEFCs) [18]. A study by Safo, I. A., et al. attempts to accelerate the oxygen reduction reaction (ORR) by creating shape-controlled nanoparticles to "modify the adsorption of reactants to the surface [18]." Polyvinylpyrrolidone (PVP) and oleylamine (OAm) were the two capping agents that were used and compared for the Pt nanocubes that were synthesized. The PVP capping agents created smaller particles than the OAm capping agents, and the OAm particles were synthesized as spheres that "showed significantly higher electrochemically active surface area and ORR activity than the PVP" particles [18]. This spherical shape created a better catalyst for the ORR. This is because the surfaces of cubes are comprised of (100) facets, which are very low-index, low surface energy. The surface of a sphere will have numerous facet types, and many of those will have high surface energy. Another example of capping agents being used to synthesize nanoparticles while controlling shape is called solution-phase synthesis. A study by Sun, Y., et al. uses metal nanoparticles to synthesize hollow interior nano-structures [19]. A shape that has a hollow interior will have higher surface areas compared to an equivalent solid structure, which often leads to greater reactivity [5]. An oxidation–reduction (redox) process called the galvanic replacement reaction was used to control the "molar ratio between Ag and AuCl4-(aq) precursor added into the reaction mixture [20]." This allowed for control of the structure of the final material.

Microwave synthesis is a method that provides a temperature change when forming the nanoparticles. The reduction rate of the precursor monomer rapidly increases in the solution, and this affects the particle formation shape. This process is used over other heating methods like heating in a water or oil bath because of the decrease in processing time [21]. A study conducted by Wang, W., et al. on zinc oxide particle synthesis showed that different microwave temperatures produced different particle shapes when using an ionic liquid [BMIM]BF_4 [22]. When the microwave was set to 50 °C, flower-like particles of ZnO were synthesized. While under the same conditions but changing the temperature to 125 °C, needle-like shapes were synthesized. In between those temperatures at 90 °C, both flower-like and needle-like particles of ZnO were synthesized, showing that changing the temperature during microwave synthesis can affect the shape of the particle being synthesized. While the advantages of the flower-like shape compared to the needle-shape particles were not studied in this experiment, it proves that microwave synthesis is a form of shape-control synthesis.

An autoclave is another tool used for shape control during nanoparticle synthesis. Autoclaves can reach temperatures and pressures that other methods can't. Shape synthesis using an autoclave is beneficial due to the fact that "the controlled environment provided by the autoclave ensures that the best possible physical properties are reputably attainable and repeatable [23]." A study by Mi, Y., et al. used the hydrothermal method in an autoclave to produce carbon micro-spheres [24]. By using a combination of a water and glucose precursor (50 ml and 4.0 g, respectively) with a 500 °C furnace, carbon micro-spheres were obtained after 12 h in the oven. When the experiment was repeated at lower temperatures of 300 and 400 °C, no carbon micro-spheres were obtained. These spheres are beneficial in the production of lithium-ion secondary batteries, and "high-density and high-strength carbon artifacts [24]." Cha, H. G., et al. show how pressure can affect nanoparticle shape in a study where "different shaped metal nanocrystals were prepared by annealing time and vacuum pressure and each have a highly crystalline structure [25]." When under a vacuum pressure of 500 mTorr, multiple shapes of crystalized nanoparticles were produced from Fe_3O_4 including rods, spheres, triangles, and diamond shapes. It was observed that as pressure increases, nanocrystals will nucleate. This synthetic process that Cha, H.G., et al. studied "is environmentally friendly and economical because it uses nontoxic and inexpensive reagents and solvents," so when applied to a larger industrial scale, there will be less pollution than other methods [25].

The concentration of precursors and type of solvent used can also be used to affect the shape. The concentration of the reducing agents, ion sources, or capping agents will affect the growth rate, changing the particle shape. Using different solvents offers different functional groups that can react with the precursor monomer. By changing the solvent used in the synthesis, the particle shape that forms can be controlled [4]. Rosenfeldt, S., et al. conducted a study where they used sodium-oleate and iron salt to synthesize a metal-oleate precursor. It was found that when using a greater excess of sodium-oleate, the particles would synthesize as cubes instead of spheres like they formed with a smaller excess of sodium-oleate [3]. This is one example of how changing the solvent/concentration can contribute to shape-control synthesis. An example of how precursors can be used for shape synthesis is shown in a study by Han, L., et al. A solution of 0.49 M $Zn(CH_3COO)_2{*}H_2O$, 0.01 M $Al(NO_3)_3$, (Zn/Al = 98: 2), 0.1 M NaOH, and 0.17 mM sodium citrate was used with Al-doped ZnO to form platelets, while a solution of 0.49 M $ZnCl_2$, 0.01 mM $AlCl_3$, (Zn/Al = 98: 2), and 0.1 mM PEG20 000 after adjusting the pH value to 7–8 using aqueous ammonia was used to form rods [13]. Both methods used a hydrothermal technique to synthesize the shapes, the platelets at 95 °C for 24 h, and the rods at 160 °C for 20 h which also shows again how heat can also have a part in controlling particle shape during synthesis. The method of concentration of materials and type of solvent is also used in a study by Sofianos, V. M., et al. where synthesized zinc oxide is used to produce hydrogen in a renewable way [11]. This is conducted by using sodium hydroxide to form ZnO nanoparticles in the shapes of cuboids, spheres, and wires. The sodium hydroxide was added to a solution of zinc acetate and absolute ethanol at three different concentrations to achieve pH levels of 8, 10, and 12 which formed nanowires, cuboids, and spheres, respectively [11]. It was concluded that the spherical-shaped nanoparticles had the highest electrocatalytic activity; however, all three particle shapes had higher electrocatalytic activities towards hydrogen production (splitting of water) than unloaded carbon control. Due to the high catalytic activity shown by this method, advancements can be made to produce clean hydrogen.

Because methods like these have been studied and proven to work in shape-control synthesis, they can be further studied and applied to the cleaner energy solutions outlined previously under the “Motivation” heading. Although these methods have been shown to be effective in shape-control synthesis of nanoparticles, the progress and development of shape control is mostly trial and error [5]. The reproducibility can be challenging due to the number of variables like material, heating method, temperature, and environment. By using more controlled environments such as autoclaves or humidity-controlled rooms, some of these inconsistencies can be irradicated.

Conclusion

As can be seen, shape-control synthesis of nanoparticles is an important part of engineering and innovation in the decarbonization process. The shape of a nanoparticle affects properties like stiffness, tensile strength, and hardness as well as functions like the particles’ ability to distribute, improve adhesion and catalysis, and promote self-assembly. These improved abilities are being used to combat carbon emissions, improve solar technology, and create more efficient batteries. Methods that use thermodynamics and kinetics including the use of capping agents, microwave synthesis, the use of an autoclave, and different concentrations and types of solvents were shown to have the ability to control the shape of nanoparticles during synthesis. While each method produced different shapes, all showed that you can start with one shape and have it change to another depending on the variables that are modified like temperature, concentration, and materials used. By proving these methods are successful, shape-control synthesis can be better implemented into combatting energy waste and carbon emissions. Although these methods were successful at shape-control synthesis in nanoparticles, the shape-control process remains complex and requires trial and error to produce desired results.

Acknowledgements This work was performed by Battelle Energy Alliance, LLC, under Contract No. DE-AC07-05-ID14517 with the U.S. Department of Energy, Office of Nuclear Energy. The student internship for Joy Morin was supported by the U.S. DOE Office of Science, Office of Workforce Development for Teachers and Scientists under the Science Undergraduate Laboratory Internship program.

References

1. What are nanoparticles? Definition, size, uses and properties. https://www.twi-global.com/technical-knowledge/faqs/what-are-nanoparticles. Accessed 15 Sept 2021
2. Adams J (1993) Particle size and shape effects in materials science: examples from polymer and paper systems. Clay Miner 28(4):509–530. https://doi.org/10.1180/claymin.1993.028.4.03

3. Rosenfeldt S, Forster S, Friedrich T, Rehnberg I, Weber B (2018) Self-assembly of magnetic iron oxide nanoparticles into cuboidal superstructures. In: Domracheva N, Caporali M, Rentschler EBT-NMN (eds) Novel magnetic nanostructures. Elsevier, pp 165–189
4. Wu Z, Yang S, Wu W (2015) Shape control of inorganic nanoparticles from solution. https://doi.org/10.1039/C5NR07681A
5. Geonmonond RS, Da Silva AGM, Camargo PHC (2018) Controlled synthesis of noble metal nanomaterials: motivation, principles, and opportunities in nanocatalysis. Anais da Academia Brasileira de Ciências 90(1)Suppl 1:719–744 (Accessed 7 Sept 2021)
6. Wang Y, He J, Liu C, Chong WH, Chen H (2015) Thermodynamics versus kinetics in nanosynthesis. https://doi.org/10.1002/anie.201402986
7. Marks LD, Peng L (2016) Nanoparticle shape, thermodynamics and kinetics. J Phys: Condens Matter 28:053001
8. Yadav S, Sharma AK, Kumar P (2020) Nanoscale self-assembly for therapeutic delivery. Front Bioeng Biotechnol
9. Okesola BO, Smith DK (2016) Applying low-molecular weight supramolecular gelators in an environmental setting—self-assembled gels as smart materials for pollutant removal. Chem Soc Rev 15:4226–4251. https://doi.org/10.1039/C6CS00124F (Review Article)
10. Neal RD, Hughes RA, Preston AS, Golze SD, Demille TB, Neretina S (2021) Substrate-immobilized noble metal nanoplates: a review of their synthesis, assembly, and application. J Mater Chem C 9:12974–13012
11. Sofianos VM, Lee J, Silvester DS, Samantha PK, Paskevicius M, English NJ, Buckley CE (2020) Diverse morphologies of zinc oxide nanoparticles and their electrocatalytic performance in hydrogen production. https://doi.org/10.1016/j.jechem.2020.07.051
12. Seher J, Froba M (2021) Shape matters: the effect of particle morphology on the fast-charging performance of LiFePO4/C nanoparticle composite electrodes. ACS Omega 6(37):24062–24069
13. Han L et al (2014) Effects of morphology on the thermoelectric properties of Al-doped ZnO. RSC Adv 4:12353. https://doi.org/10.1039/c3ra47617k
14. Verma SK, Tiwari AK (2015) Application of nanoparticles in solar collectors. A Rev Mater Today: Proc 2:3638–3647
15. Caldorera-Moore M, Guimard N, Shi L, Roy K (2010) Designer nanoparticles: incorporating size, shape and triggered release into nanoscale drug carriers. Expert Opin Drug Deliv 7(4):479–495. https://doi.org/10.1517/17425240903579971
16. Zhu W, Kattel S, Jiao F, Chen JG (2019) Shape-controlled CO_2 electrochemical reduction on Nanosized Pd hydride cubes and Octahedra. United States: N. Web. https://doi.org/10.1002/aenm.201802840
17. Javed R, Zia M, Naz S, Aisida SO, Ain NU, Ao Q (2020) Role of capping agents in the application of nanoparticles in biomedicine and environmental remediation: recent trends and future prospects. J Nanobiotechnol 18:172. https://doi.org/10.1186/s12951-020-00704-4
18. Safo IA, Dosche C, Özaslan M (2019) Effects of capping agents on the oxygen reduction reaction activity and shape stability of Pt nanocubes
19. Sun Y, Mayers B, Xia Y (2003) Metal nanostructures with hollow interiors. Adv Mater 15:641–646. https://doi.org/10.1002/adma.200301639
20. Xia X, Wang Y, Ruditskiy A, Xia Y (2013) 25th anniversary article: galvanic replacement: a simple and versatile route to hollow nanostructures with tunable and well-controlled properties. Adv Mater 25:6313–6333. https://doi.org/10.1002/adma.201302820
21. Tsuji M (2017) Microwave-assisted synthesis of metallic nanomaterials in liquid phase. Chem Sel 2:805. https://doi.org/10.1002/slct.201700011
22. Wang W, Zhu Y (2004) Shape-controlled synthesis of zinc oxide by microwave heating using an imidazolium salt. Inorg Chem Commun 7(9):1003–1005. ISSN 1387-7003
23. Pani A, Lee JH, Yun SI (2016) Autoclave mediated one-pot-one-minute synthesis of AgNPs and Au–Ag nanocomposite from Melia azedarach bark extract with antimicrobial activity against food pathogens. Chem Cent J 10:15

24. Mi Y, Hu W, Dan Y, Liu Y (2008) Synthesis of carbon micro-spheres by a glucose hydrothermal method. Mater Lett 62(8–9)
25. Cha HG, Lee DK, Kim YH, Kim CW, Lee CS, Kang YS (2008) Solventless nanoparticles synthesis under low pressure. Inorg Chem 47(1):121–127. https://doi.org/10.1021/ic701570z
26. Zhao Y, Wang Y, Ran F, Cui Y, Liu C, Zhao Q, Gao Y, Wang D, Wang S (2017) A comparison between sphere and rod nanoparticles regarding their in vivo biological behavior and pharmacokinetics. Sci Rep 7:4131. https://doi.org/10.1038/s41598-017-03834-2
27. Kord M, Hedayati K, Farhadi M (2017) Green synthesis and characterization of flower-like PbS and metal-doped nanostructures via hydrothermal method. Main Group Met Chem 40(1–2):35-40. https://doi.org/10.1515/mgmc-2016-0046
28. Sun Y, Xia Y (2003) Shape-controlled synthesis of gold and silver nanoparticles. Science (New York, N.Y.) 298:2176–2179. https://doi.org/10.1126/science.1077229
29. Champion JA, Katare YK, Mitragotri S (2007) Making polymeric micro- and nanoparticles of complex shapes. PNAS 104(29):11901–11904. https://doi.org/10.1073/pnas.0705326104
30. Womiloju AA, Höppener C, Schubert US, Hoeppener S (2020) Microwave-assisted synthesis of core–shell nanoparticles—insights into the growth of different geometries. https://doi.org/10.1002/ppsc.202000019
31. Paiva-Marques WA, Gómez FR, Oliveira Jr ON (2020) Chiral plasmonics and their potential for point-of-care biosensing applications. Sensors 20(3):944. https://doi.org/10.3390/s20030944

Silicon Production from SiO Gas via Gas-Phase Reactions

Halvor Dalaker

Abstract The production of silicon with hydrogen is very challenging, although it is possible to get partway there, as SiO gas can form from SiO_2 and H_2. For some applications, metallurgical grade silicon is only an intermediary to gas-phase silicon species and “not needed” from a value-chain point of view. This work explores the possibility of going directly from SiO gas to useful Si-based gases with gas-phase chemistry. In particular, it looks into reactions between SiO gas and Cl_2 gas to form $SiCl_4$, which can be turned into raw materials for polysilicon production in the Siemens process. If successfully implemented, this would make CO_2-free polysilicon production possible. The work is theoretical in nature and is based on thermodynamical calculations using FactSage. Assessing the process steps in isolation, calculations show that both SiO formation from H_2 and SiO_2 and the formation of $SiCl_4$ from SiO are thermodynamically favourable. Combining the two steps in a process is likely to be challenging however, since if H_2/H_2O from the first step is present during the second, this will interfere with the chlorination of SiO, representing a serious bottleneck. Unless SiO can somehow be separated from H_2/H_2O at very high temperatures, success seems to be dependent on rapid quenching while suppressing back-reactions.

Keywords Silicon · Hydrogen · Silanes · Sustainability

Introduction

Silicon production is associated with large CO_2 emissions. In current industrial processes, SiO_2 is reacted with carbon into CO_2 and Si, which means that CO_2 is a natural by-product that is hard to avoid. The options for CO_2-abatement are to either capture the emitted CO_2, to use sustainably sourced and CO_2-neutral biologically based carbon (charcoal, biogas, etc.), or to invent new processes without carbon. Hydrogen is a gas that is predicted to play a role in the decarbonisation of many

---

H. Dalaker (✉)
SINTEF Industry, Trondheim, Norway
e-mail: Halvor.dalaker@sintef.no

F. Tesfaye et al. (eds.), *REWAS 2022: Energy Technologies and CO_2 Management (Volume II)*, The Minerals, Metals & Materials Series,
https://doi.org/10.1007/978-3-030-92559-8_4

sectors, including metallurgy, with particular attention on iron and steel. Unfortunately, as opposed to the iron oxides, which react with hydrogen to form metallic iron, silicon oxide cannot easily be reduced to silicon by hydrogen, and the reaction between SiO_2 and H_2 to Si is thermodynamically unfavourable below 4500 °C. However, the part-reaction to SiO gas, $SiO_2 + H_2 \rightarrow SiO + H_2O$, has been reported experimentally by several groups [1–3].

In the Siemens process for high-purity polysilicon production, the main raw materials are typically either trichlorosilane ($SiHCl_3$) or monosilane (SiH_4). In the process steps leading up to these species, silicon tetrachloride $SiCl_4$ is an unavoidable by-product, which can be turned into trichlorosilane through hydrogenation reactions.

According to calculations in FactSage [4], the reaction between SiO gas and chlorine gas into silicon tetrachloride is thermodynamically favourable at temperatures below 2740 °C. Thus, the prospect arises of a new process in which hydrogen is used to produce SiO gas, which is then chlorinated to $SiCl_4$, which is further upgraded into trichlorosilane and used in polysilicon production. This would remove the need to produce metallurgical grade silicon as an intermediary and make the value chain independent of carbon. If such a value chain could be realised, it would make silicon production without process-related CO_2 emissions possible. No investigations of the concept of chlorination of SiO gas were found in the literature.

The aim of the present work is to explore some key reactions and concepts surrounding this new hypothetical process. The objectives are: to assess to what extent such a process is theoretically feasible and deserving of further study; and if applicable to identify the main bottlenecks against realisation, which should be the focus of follow-up studies.

The work is based on thermodynamic calculations using FactSage [4]. The databases used were FactPS and FToxid.

Thermodynamics of Key Process Steps

In this section, the different steps from SiO production to $SiCl_4$ production are discussed. Once an overview of the different reactions has been presented, the next section will present a possible flowsheet for a potential process.

SiO Production with Hydrogen

Figure 1 shows the equilibrium partial pressure of SiO in a system with a surplus of SiO_2 and H_2 at one atmosphere total pressure, as calculated using FactSage. It can be seen that depending on the temperature at which the reaction takes place, the SiO will make up only around 1–10% of the total gas. This indicates that a large surplus of hydrogen will be needed in an industrial process and that looping of this hydrogen will likely be critical.

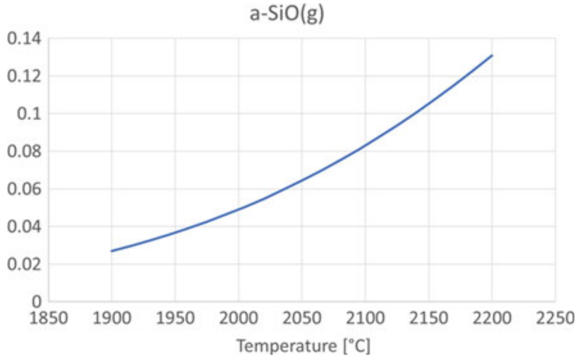

Fig. 1 Partial pressure/activity of SiO gas in equilibrium with SiO_2 and H_2 as a function of temperature, as calculated from FactSage. Total pressure is 1 atm

Chlorination of SiO Gas

Having generated SiO gas, the next step will be to react it to useful gaseous species. In this work, only chlorine-based species have been considered, but it is possible that other halides could also offer some potential. Considering chlorine, SiO gas can react with chlorine species to form chlorinated silanes according to several reactions, some examples of which are shown in Table 1.

Since SiO is unstable at low temperatures (Stable above 1870 °C in a pure SiO atmosphere), the most relevant reactions are those between SiO and Cl_2. A common feature is the presence of SiO_2 on the right-hand side of these reactions. This means that in a real process, there would be a need to loop the SiO_2 back to the SiO production step.

Table 1 Some potential reactions between SiO gas and chlorinated species, and the temperature range in which they are thermodynamically favourable. Also included in the last line is the reaction to silane in the chlorine-free $SiO\text{-}H_2$ system

Reaction	Temperature range for G < 0 (°C)
$SiO + Cl_2 \rightarrow SiCl_4 + SiO_2$	T < 2740
$4\ SiO + 3\ Cl_2 \rightarrow 2\ SiCl_3 + 2\ SiO_2$	T < 2752
$2\ SiO + Cl_2 \rightarrow SiCl_2 + SiO_2$	T < 2692
$4\ SiO + Cl_2 \rightarrow SiCl + 2\ SiO_2$	T < 1898
$6\ SiO + 3\ HCl \rightarrow SiHCl_3 + 2\ SiH + 3SiO_2$	T < 1420
$6\ SiO + 3\ HCl \rightarrow 2\ SiHCl_3 + SiH_4 + 3SiO_2$	T < 1572
$2\ SiO + 2\ HCl \rightarrow 4\ SiH_2Cl_2 + 2SiO_2$	T < 1609
$6\ SiO + 6\ HCl \rightarrow 2\ SiH_3Cl + SiCl_4 + 3\ SiO_2$	T < 1563
$2\ SiO + 2\ H_2 \rightarrow SiH_4 + SiO_2$	T < 1276

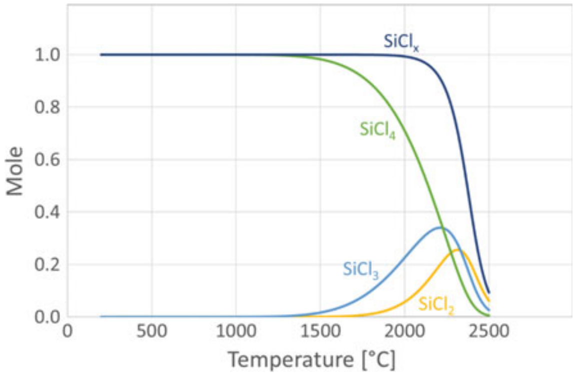

Fig. 2 Amount of different Si-Cl species in a SiO-Cl_2 mixture as a function of temperature. $SiCl_x$ denotes the sum of all Si-Cl species. At higher temperatures, the product SiO_2 (not shown) is not stable, so the various Si-Cl species do not form. Calculated using FactSage

In a real reaction between significant amounts of SiO and Cl_2, no single reaction will dominate, and the different Si-Cl species $SiCl_4$, $SiCl_3$, $SiCl_2$, and SiCl will all occur among the products in varying amounts. For simplicity, the nomenclature "$SiCl_x$" is introduced. It is taken to mean the sum of all Si-Cl species:

$$SiCl_x = SiCl_4 + SiCl_3 + SiCl_2 + SiCl.$$

Figure 2 shows the different amounts of $SiCl_4$, $SiCl_3$, and $SiCl_2$ as a function of temperature in a reaction between SiO and Cl_2 (SiCl exists only in trace amounts). It is seen that at lower temperatures, $SiCl_4$ is the preferred product and that this changes towards $SiCl_3$ and $SiCl_2$ at higher temperatures. The total amount of Si-Cl species, $SiCl_x$, is also included in the figure. It is seen that the total amount of Si-Cl species is constant at temperatures below approximately 2000 °C, but then starts to drop. This is because, at very high temperatures, monoatomic Cl and SiO are both relatively stable, so SiO will not react as easily with Cl_2. This means that there is probably an upper limit to the temperature at which a chlorination process would need to take place, but it is unlikely that such a limit would be significant in industrially relevant conditions. Calculations show that at 2100 °C, more than 97% of the chlorine will still react with SiO, dropping to 90% around 2200 °C, and even at temperatures as high as 2370 °C, 50% of the SiO still reacts.

Chlorination of SiO Gas in the Presence of H_2/H_2O

As Fig. 1 shows, if hydrogen gas is used to produce SiO from SiO_2, only a small fraction of the resulting gas mixture will be SiO. An equal fraction will be H_2O (assuming temperatures are low enough to avoid H_2O disassociation), and the remainder will be unreacted H_2. This has a massive impact on the subsequent chlorination step since

H_2 can react with Cl_2 to form hydrochloric acid, HCl:

$$H_2 + Cl_2 \leftrightarrow 2\,HCl.$$

As Fig. 3 shows, this reaction is more thermodynamically favourable than the desired reaction between SiO and Cl_2 at temperatures above approximately 1750 °C. It could be conceived that this could be circumvented by having a two-step process: First generating SiO gas at high temperature, and then doing the chlorination at a lower temperature. The problem then is that the SiO-generating reaction is an equilibrium reaction involving hydrogen and water:

$$H_2 + SiO_2 \leftrightarrow H_2O + SiO.$$

As has been shown, increasing the temperature drives this reaction towards the right, so with both SiO and H_2O in the system, lowering the temperature would drive it back to the left. Furthermore, even at lower temperatures, it is unlikely that the chlorination of SiO would completely dominate HCl formation since both reactions are still thermodynamically favourable and there is much more H_2 than SiO in the system. Since HCl formation consumes hydrogen, this would further act to drive the SiO-formation reaction towards the left. Under equilibrium conditions above 1750 °C, therefore, no chlorination of SiO would be expected to take place in the presence of H_2 and H_2O. Equilibrium calculations bear this out. Figure 4 shows the equilibrium composition of a gas mixture initially consisting of 0.8 mol H_2, 0.1 mol SiO, and 0.1 H_2O, to which increasing amounts of Cl_2 are added. It is seen that at low amounts of Cl_2, HCl formation dominates. At higher amounts of Cl_2, there is also some back-reaction between SiO and H_2O to SiO_2, but at no point does any significant amount of Si-Cl species form.

Fig. 3 Gibbs energy of reaction for the reaction of chlorine with SiO and hydrogen, as calculated using FactSage

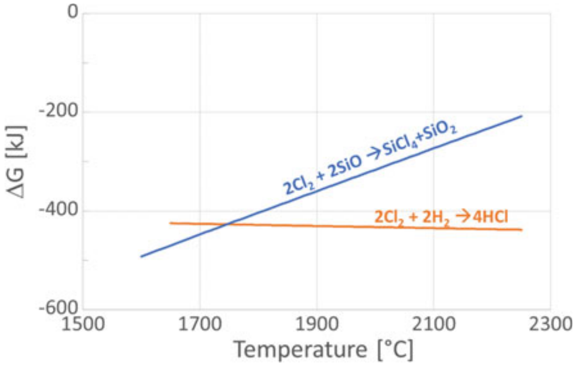

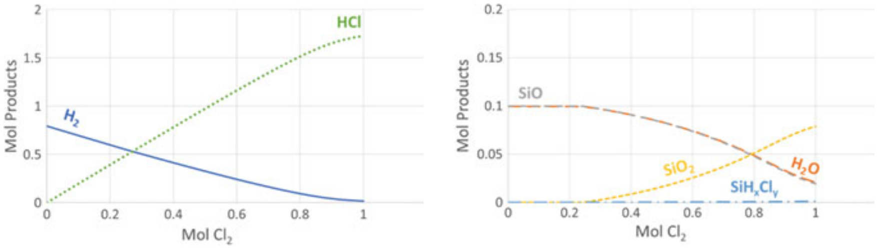

Fig. 4 Equilibrium composition, at 2150 °C of a gas mixture initially composed of 0.8 mol H_2, 0.1 mol H_2O, and 0.1 mol SiO, with additions of varying amounts of Cl_2. The products are displayed in two different charts due to the order of magnitude difference in the amounts of products (note the difference in scale on the Y-axes). The SiH_xCl_y curve represents the total combined amount of $SiCl_4$, $SiCl_3$, $SiCl_2$, and $SiHCl_3$. It is always below 0.002

Flowsheet of Potential Process

It was mentioned above that chlorination of SiO gas in the presence of H_2 and/or H_2O is impossible and that the quenching of SiO gas prior to chlorination in the presence of H_2O would likely lead to back-reaction and loss of SiO. Successful implementation of the ideas presented herein is thus thought to depend on either:

- the development of new high-temperature gas-separation technologies or
- the successful quenching of SiO gas while suppressing back-reaction of SiO and H_2O to SiO_2.

For the purposes of this discussion, it is assumed that SiO *can* be separated from H_2 and H_2O, in order to lay out what a process could look like should such a technological solution become available in the future.

Figure 5 shows a flowsheet for a potential process based on our current understanding of the phenomena. The flowsheet is based on a production unit of 1 mol of $SiCl_4$. This requires an input of 1 mol SiO_2 and 2 mol Cl_2. In addition, hydrogen is needed for the SiO-formation step. The SiO formation can be expected to have a hydrogen utilisation rate of around 10% (see Fig. 1), so some 10 mol of hydrogen will be needed per mol of SiO_2. With such a low utilisation grade, it will be necessary to loop the hydrogen, and only 2 mol of fresh H_2 will be needed per mol of $SiCl_4$ produced. With that in mind, it is suggested that hydrogen is supplied from an on-site electrolyser, where the recycled water vapour can be used as feed to the electrolyser, although other solutions are of course also possible. The electrolyser would require about 0.1 kWh per mol of H_2 produced or about 0.2 kWh per mol of $SiCl_4$ product.

In the SiO-production step, 20 mol H_2 reacts with 2 mol SiO_2, resulting in a gas mixture of 18 mol H_2, 2 mol SiO, and 2 mol H_2O. As outlined above, based on the current evaluation, it does not seem possible to perform chlorination of SiO gas in the presence of H_2 and/or H_2O. A gas-separation step is therefore necessary, to separate the SiO from the H_2 and H_2O.

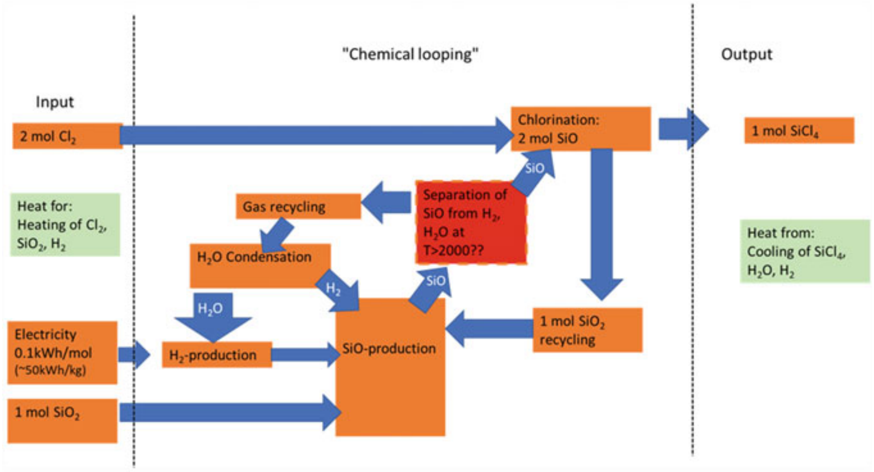

Fig. 5 Potential flowsheet of process based on $SiCl_4$ production from SiO_2 via SiO formation through hydrogen reduction. The need to separate SiO from H_2 and H_2O at high temperatures is expected to be a potential showstopper. See the text for further details

From here, the H_2-H_2O mixture goes through a condensation step, resulting in 18 mol pure H_2 that is returned to the SiO-production step. The condensed water can be returned to the electrolyser and turned back into hydrogen, and then added to the recycled hydrogen to maintain the correct ratio in the SiO-production unit.

Returning to the SiO gas, after the SiO-H_2/H_2O-separation step, 2 mol of SiO is reacted with 2 mol of Cl_2 gas. This causes half the SiO to be turned into SiO_2 (likely liquid droplets), which can be collected and returned to the SiO-production unit. The remainder of the SiO is turned into $SiCl_4$ product. In addition to the mass flows described above, the electrolyser will produce 1 mol of O_2 per 2 mol of H_2. This mass stream is not included in Fig. 5.

Since it is likely that the separation of SiO from H_2 and H_2O at high temperature is impossible, the total energy consumption of the process (heating, etc.) has not been estimated at the present stage.

A final challenge that has not been discussed or looked into in detail is whether realistic reactor materials exist that can withstand the corrosive gases like HCl and Cl_2 at the very high temperatures involved.

Conclusions

The idea of sidestepping the last reduction step in silicon production is an attractive one. Thermodynamic calculations have shown that it is possible to.

- produce SiO gas from SiO_2 with hydrogen:

$$SiO_2 + H_2 \leftrightarrow SiO + H_2O;$$

- produce silicon tetrachloride, $SiCl_4$, a potential raw material for polysilicon production, from SiO gas:

$$2\,SiO + 2\,Cl_2 \leftrightarrow SiO_2 + SiCl_4.$$

However, some important bottlenecks remain. The most important at present seems to be that the $SiCl_4$ formation from SiO gas is not possible in the presence of hydrogen gas, since Cl_2 and H_2 will preferentially react to form HCl. This could conceivably be solved either by separating the SiO and H_2 gas at a very high temperature (~2000 °C), but we are not aware of any known technology that could handle this issue. Another solution could be to quench the gas mixture while somehow suppressing the back-reaction $SiO + H_2O \rightarrow SiO_2$ and the condensation reaction $2\,SiO \rightarrow Si + SiO_2$. If quenched sufficiently below 1750 °C, it is possible that $SiCl_4$ formation could dominate HCl formation.

Any solution would also need to solve the material integrity challenges associated with corrosive gases at high temperatures.

Acknowledgements This work has been performed as part of the project "Reduced CO_2 emissions in metal production", which is financed by the Norwegian Research Council (project number 280968), and the industry partners Elkem, Eramet, Wacker, Finnfjord, and TiZir.

I also wish to thank my colleagues Ida Kero and Karen Osen for valuable input and discussions.

References

1. Tso ST, Pask JA (1982) Reaction of fused silica with Hydrogen gas. J Am Ceram Soc 65(9):457–460
2. Lewis SD (1979) Reduction of fused silica in hydrogen. MSc thesis, The University of Utah, Salt Lake City
3. Shirai H, Saito M, Pan L-S, Abe T (2001) Flow and diffusion analysis on the kinetics of reduction of fused silica in Hydrogen. J Solid State Chem 160:247–250
4. Bale CW, Bélisle E, Chartrand P, Decterov SA, Eriksson G, Gheribi AE, Hack K, Jung IH, Kang YB, Melançon J, Pelton AD, Petersen S, Robelin C, Sangster J, Van Ende M-A (2016) FactSage thermochemical software and databases, 2010–2016. Calphad, 54:35–53. www.factsage.com

Macroscopic Modeling and Phase Field Modeling of Solar Grade Silicon by Molten Salt Electrolysis

Aditya Moudgal, Mohammad Asadikiya, Douglas Moore, Gabriel Espinosa, Lucien Wallace, Alexander Wadsworth, Tyler Melo, Alexander Alonzo, Andrew Charlebois, Evan Costa, Peter Catalino, Adam Clayton Powell, Yu Zhong, and Uday Pal

Keywords Silicon · Electrometallurgy · Modeling · Primary metals manufacturing

---

A. Moudgal (✉) · M. Asadikiya · A. C. Powell · Y. Zhong
Materials Science and Engineering Program, Worcester Polytechnic Institute, 100 Institute Rd, Worcester, MA 01609, USA
e-mail: amoudgal@wpi.edu

M. Asadikiya
e-mail: masadikiya@wpi.edu

A. C. Powell
e-mail: acpowell@wpi.edu

Y. Zhong
e-mail: yzhong@wpi.edu

A. Moudgal · D. Moore · G. Espinosa · L. Wallace · A. Wadsworth · T. Melo · A. C. Powell · Y. Zhong
Department of Mechanical Engineering, Worcester Polytechnic Institute, 100 Institute Rd, Worcester, MA 01609, USA
e-mail: dmmoore@wpi.edu

G. Espinosa
e-mail: grespinosa@wpi.edu

L. Wallace
e-mail: lrwallace@wpi.edu

A. Wadsworth
e-mail: ajwadsworth@wpi.edu

T. Melo
e-mail: tamelo@wpi.edu

M. Asadikiya · A. Alonzo · A. Charlebois · E. Costa
Department of Chemical Engineering, Worcester Polytechnic Institute, 100 Institute Rd, Worcester, MA 01609, USA
e-mail: ajalonzo@wpi.edu

F. Tesfaye et al. (eds.), *REWAS 2022: Energy Technologies and CO_2 Management (Volume II)*, The Minerals, Metals & Materials Series,
https://doi.org/10.1007/978-3-030-92559-8_5

Introduction

The sixth Intergovernmental Panel on Climate Change report (IPCC) recently released predicts a deep reduction in emissions to meet global goals of 1.5 °C reduction in temperature. It states that concentrations of CO_2 have continuously increased in the atmosphere reaching averages of 410 ppm in 2019 [1]. Therefore, it becomes imperative to reduce CO_2 in any way possible. Silicon, which is an important material for renewable energy, electronics, and metallurgy, is primarily produced by the carbothermic reduction of quartz. This metallurgical grade silicon is then refined by the Siemens Process to solar grade silicon using hydrogen chloride. The by-product of trichlorosilane from this process is highly volatile and unstable [2].

This work aims to achieve the above process of reduction in a single step using electrochemistry. This would eliminate multiple steps and save energy and cost and reduce emissions if a suitable inert anode is used in production. Understanding electrochemical cell characteristics therefore is needed to prove and scale this technology.

Macroscopic models help engineers to design, develop, and improve the efficiency of electrochemical cells. They solve conservation equations of mass, momentum, and energy and help determine electrode current distribution, fluid flow, heat distribution, and stability of the cell [3]. They also help in correlating experimental work and understanding measurements in cells from a lab scale to a plant scale. However, they do not predict the microstructure and plating of material on the cathode. This can be calculated using phase field models. These phase field models predict interface stability and deposition morphology in the cell. In this work, we present these models in addition to proof-of-concept experiments.

A. Charlebois
e-mail: amcharlebois@wpi.edu

E. Costa
e-mail: epcosta@wpi.edu

P. Catalino
Department of Electrical Engineering and Computer Science, Worcester Polytechnic Institute,
100 Institute Rd, Worcester, MA 01609, USA
e-mail: pjcatalino@wpi.edu

U. Pal
Division of Materials Science and Engineering, Boston University, 730 Commonwealth Ave,
Boston, MA 02215, USA
e-mail: upal@wpi.edu

Materials and Methods

Cell Design

The cell design followed here for the macroscopic models is described in Moudgal et al. [4]. The lab scale experimental apparatus complements the model except a carbon anode with a Yttria Stabilised Zirconia solid oxide membrane tube [5] with silver is used in the place of an inert anode. The carbon anode is currently being used as it provides higher conductivity. A new oxygen evolving porous lanthanum nickelate ($LaNiO_3$) electrode with comparable conductivity is currently under development. The molten salt electrolyte used is a fluoride-based salt with a CaF_2–MgF_2 eutectic with CaO, $YO_{1.5,}$ and SiO_2. This salt was developed by Uday Pal et al. [6]. It has been shown that silicon can be reduced using a liquid tin cathode using this salt [7].

Macro Models

The goal of the macro models is to solve conservation equations of mass, momentum, and energy to gain a better understanding of the cell. The model uses COMSOL version 5.6, and the modules used are the electrochemistry module, electrodeposition module, and the fluid flow and heat transfer modules.

Phase Field Model

The phase field model solves the Cahn–Hilliard equations for cathode growth with electric field concentration and cathode growth as described by Pongsaksawad et al. [8]. It uses one or more field variables of C to describe the composition and differentiate between the Si deposit and electrolyte in accordance with Eqs. (1) and (2) below.

$$F = \int \left[H(C) + K|\nabla C|^2 + \frac{zF\rho}{M}(1-C)\phi \right] \tag{1}$$

$$\frac{DC}{Dt} = \nabla \cdot \left(\kappa \nabla \left(\frac{\partial H}{\partial C} - K\nabla^2 C \right) + \kappa \frac{zF\rho}{RTM} \frac{1-C}{1+C} \nabla\phi \right) \tag{2}$$

where $H(C)$ is homogeneous free energy, K is gradient penalty coefficient, and κ is mobility.

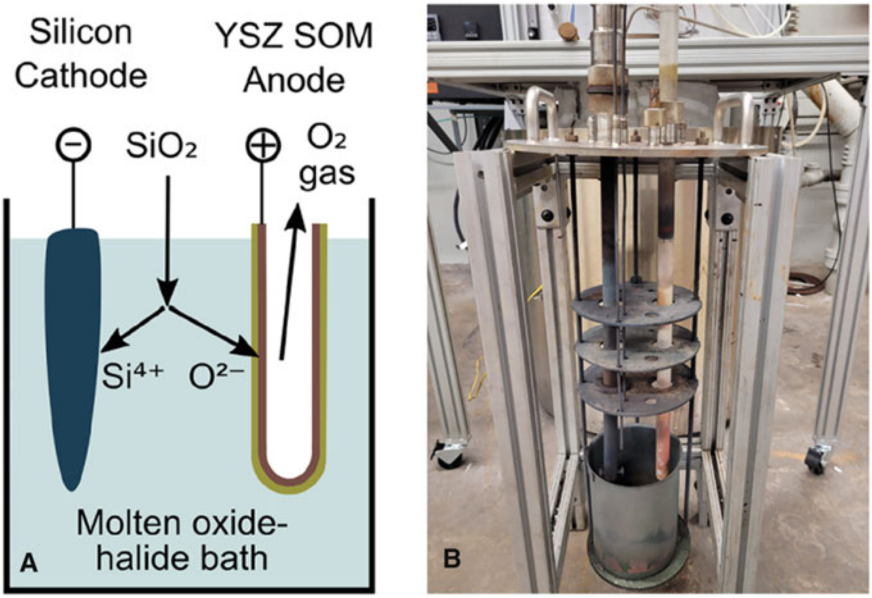

Fig. 1 **a** Diagram of the proposed process. **b** Experimental setup of electrochemical cell at lab scale consisting of **a** stainless steel crucible

Experimental

Experiments are conducted in a standard two-electrode high-temperature electrochemistry setup as shown in Fig. 1. Electrodes are completely immersed in the salt composition mentioned above, i.e., CaF_2–MgF_2–CaO–$YO_{1.5}$–SiO_2. The base eutectic with the calcium oxide and yttrium oxide in composition by weight 45.5% CaF_2, 36.4% MgF_2, 9% CaO, and 3.6% $YO_{1.5}$ are mixed first and dried in an inert environment of argon gas at 350 °C before being fused together at 1100 °C and crushed. 5 wt.% SiO_2 is added, and the salt is dried again in argon before being electrolysed at 1100 °C. There is a low potential pre-electrolysis step carried out before successive electrolysis is carried out in multiple intervals. Characterization was done using scanning electron microscopy and energy-dispersive x-ray spectroscopy.

Summary and Conclusions

In this work, the main goal is the decarbonization of silicon production to produce high-purity solar grade silicon at low costs. We have shown and described methods that can be used to achieve this primary production in a single step. Further development and analysis of the anode and flux is currently underway. We anticipate that the methods described can be applied to a scaled-up electrochemical cell in the future.

Conflict of Interest The authors declare that they have no conflict of interest.

References

1. AR4 Climate Change 2007: the physical science basis—IPCC. https://www.ipcc.ch/report/ar4/wg1/. Accessed 23 Aug 2021
2. Cowern NEB (2012) 1—silicon-based photovoltaic solar cells. In: Kilner JA, Skinner SJ, Irvine SJC, Edwards PP (eds) Functional materials for sustainable energy applications. Woodhead Publishing, pp 3–22e. https://doi.org/10.1533/9780857096371.1.1
3. Powell AC, Shibuta Y, Guyer JE, Becker CA (2007) Modeling electrochemistry in metallurgical processes. JOM 59(5):35–43. https://doi.org/10.1007/s11837-007-0063-y
4. Moudgal A et al (2021) Finite element analysis and techno-economic modeling of solar silicon molten salt electrolysis. JOM 73(1). https://doi.org/10.1007/s11837-020-04468-y
5. Pal UB, Powell AC (2007) The use of solid-oxide-membrane technology for electrometallurgy. JOM 59(5):44–49
6. Pal U, Su S, Villalon T (2017) Molten flux design for solid oxide membrane-based electrolysis of aluminium from alumina. In: Applications of process engineering principles in materials processing, energy and environmental technologies, pp 35–44
7. Villalón Jr T (2018) Zero-direct emission silicon production via solid oxide membrane electrolysis. PhD, Boston University, Boston, MA, USA. https://hdl.handle.net/2144/30729
8. Pongsaksawad W, Powell AC, Dussault D (2007) Phase-field modeling of transport-limited electrolysis in solid and liquid states. J Electrochem Soc 154(6):F122–F133

Design of a Molten Salt Metal-Air Battery with High-Energy Density

Mahya Shahabi, Nicholas Masse, Hongyi Sun, Lucien Wallace, Adam Powell, and Yu Zhong

Abstract Decarbonization of long-haul transportation, i.e., ships and trains is among the toughest challenges toward eliminating greenhouse emissions, but metal-air batteries have extraordinary potential to meet this challenge. More specifically, Mg-air batteries have the potential for 30–40 times the energy of lithium-ion batteries at very high efficiency, and their Mg anode and molten salt materials are abundant in seawater. The two main criteria for these batteries are stability of the cathode material and removal of MgO product from the electrolyte through directional solidification. This talk will present experimental and modeling results for a novel molten salt magnesium-air battery with an $MgCl_2$–NaCl–KCl electrolyte operating at 420–620 °C. O^{2-} dissolves at the cathodes and Mg^{2+} at anodes. Experimental results show 1.9 V open-circuit voltage, which is the highest to date for an Mg-air battery. Modeling shows up to 1.17 W/cm^2 at 73% efficiency and 2.89 W/cm^2 at 36% efficiency. This work illustrates the proof of concept of Mg-air batteries and discusses the requirements for larger-scale cells.

Keywords Metal-air battery · Directional solidification · Oxygen reduction · Zero-emission shipping

Nomenclature

η_{act}	Activation polarization
V	Actual cell voltage
T_0	Ambient temperature
j_{0a}	Anodic exchange current density
ASR_{ohm}	Area-specific resistance for ohmic polarization
j_{0c}	Cathodic exchange current density
α_a	Charge transfer coefficients of anodic reactions

M. Shahabi (✉) · N. Masse · H. Sun · L. Wallace · A. Powell · Y. Zhong
Mechanical Department, Worcester Polytechnic Institute, Worcester, MA 01609, USA
e-mail: mshahabi@wpi.edu

F. Tesfaye et al. (eds.), *REWAS 2022: Energy Technologies and CO_2 Management (Volume II)*, The Minerals, Metals & Materials Series,
https://doi.org/10.1007/978-3-030-92559-8_6

α_c	Charge transfer coefficients of cathodic reactions
α_i	Charge transfer coefficients of substances where i represents each species in the reactions
η_{conc}	Concentration polarization
$D_{cathode}$	Diffusion coefficient of cathode
D	Diffusion coefficient of charge carrier
F	Faraday's constant (96,485.3329 C/mol)
G	Gibb's free energy
HEF	Heat exchanger efficiency
j_L	Limiting current density
$C_{L,cathode}$	Limiting MgO molar density
L_{el}	Lorentz number (2.44e-8 W. Ω.K^{-2})
C	Molar density
j	Net current density
n_{cells}	Number of cells
n	Number of electrons participating in the reaction
n_{leads}	Number of leads
η_{ohm}	Ohmic polarization
T	Operating temperature
OCR	Oxygen consumption ratio
η	Polarization
ΔT	Temperature above that of environment
E_{th}	Theoretical open-circuit voltage
L	Thickness of electrode
ΔV_{lead}	Voltage loss from the leads

Introduction

Literature Review

Lithium-ion batteries (LIBs) have a wide variety of applications. They are used as portable battery-powered electronic devices, especially in notebook computers and mobile phones applications as well as electric vehicle (EV) and electric motor bicycles [1]. Despite the widespread use of LIBs, they face several challenges. These challenges include high cost, low energy density, safety, and environmental hazard which makes them less favorable for future high-efficiency energy storage demand [2]. Metal-air batteries on the other hand have been studied since the 1960s [3] and have been intensely focused upon as promising next-generation high-energy batteries [4].

Metal-air batteries use metal as the anodic reactant and oxygen from the air as the cathode. This cathode allows battery weight to drop and makes valuable space

Table 1 Comparison of potential fuels and batteries for long-range transportation. The red color illustrated the cons of the energy source while green illustrates optimal property. (Color table online)

Energy source	Bunker fuel	Mg	NH_3	H_2	Li-ion	Fe	Al
Fuel specific energy, kWh/kg	12.8	6.9	5.2	39.7	0.2	1.4	8.6
Stored fuel sp. energy, kWh/kg	10	5	3	1-3	0.2		
(Round-trip) efficiency	50%	40-55%	30%	40%	90%		
Delivered energy cost, $/kWh	0.03	0.3	0.4	0.3	<0.1		
Energy storage cost, $/kWh	Small	1-3	10	23	100		
Direct operating emissions	CO_2 , SO_2	–	NO_x, NH_3	–	–		Al_2O_3, $AlCl_3$

available for storing energy. Table 1 provides an overview of metal-air batteries' properties and their costs along with other common or potential shipping energy sources. It is important to note that H_2 with the highest fuel-specific energy (39.7 kWh/kg) has very low stored fuel-specific energy which is around 1–3 kWh/kg. The next highest fuel-specific energy is for bunker fuels; however, they emit CO_2 as well as SO_2, the former being the principal greenhouse gas contributing to global warming [5]. Similarly, Alumina (Al_2O_3) is produced when using Al as the anode which can accumulate in organs and lead to health problems. With a molten salt electrolyte, this process also produces aluminum salts ($AlCl_3$) which are highly toxic [6]. However, considering resource availability, Magnesium is an emission-free energy source that has high fuel and storage-specific energy as well as high-energy density and minimal toxicity which make it a suitable alternative for high-energy applications.

Current Metal-Air Battery Challenges

Despite the acceptable range of specific energy of metal-air batteries, efficient direct recovery of electrical energy from most of the metal oxidation enthalpy in a fuel cell is challenging for four primary reasons:

(1) Metal oxidation forms a passive oxide film, and in the case of aqueous electrolytes presence, a hydroxide film. Oxide or hydroxide films slow or shut down the reaction.
(2) Reactive metals with the highest energy per ion such as Li, Ca, Mg, and Al undergo a parasitic reaction with aqueous electrolytes to form hydrogen [7].
(3) The oxygen reduction reaction requires precious metal catalysts such as platinum or palladium.
(4) It is necessary to remove the oxidation product from the electrolyte [8].

These challenges have been addressed in this design. Starting with the first challenge, the electrolyte also has sufficient metal oxide solubility to avoid oxide film formation. Moreover, an anhydrous molten salt electrolyte eliminates hydrogen production which helps with both the first and second challenges. The third challenge is resolved by having operating conditions like high temperature which removes the need for precious metal catalysts [9–11]. The most common cathode material is nickel, which is oxidized in situ to NiO [9–12]. Finally, to face the last problem, one can remove the metal oxide reaction product from the electrolyte by directional solidification or filtration as in [8].

Magnesium Properties

Magnesium metal is potentially a viable zero-emission fuel for shipping propulsion due to: higher energy density than liquid fuels, higher specific energy than alkanes, high potential battery efficiency, the prevalence in seawater, fewer health issue than Al and Si, and recyclable products such as MgO, $Mg(OH)_2$, and $MgCO_3$ (Fig. 1). As presented in Table 1, an efficient Mg-air battery could cleanly deliver the energy needed for long-haul shipping, and the Mg is an ideal energy shipping medium: Mg specific energy is 3.7 times that of methylcyclohexane-toluene hydrogen storage.

Fig. 1 Mg properties

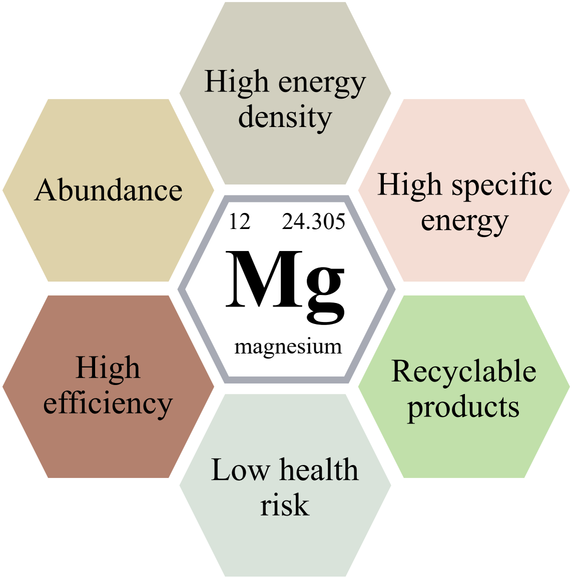

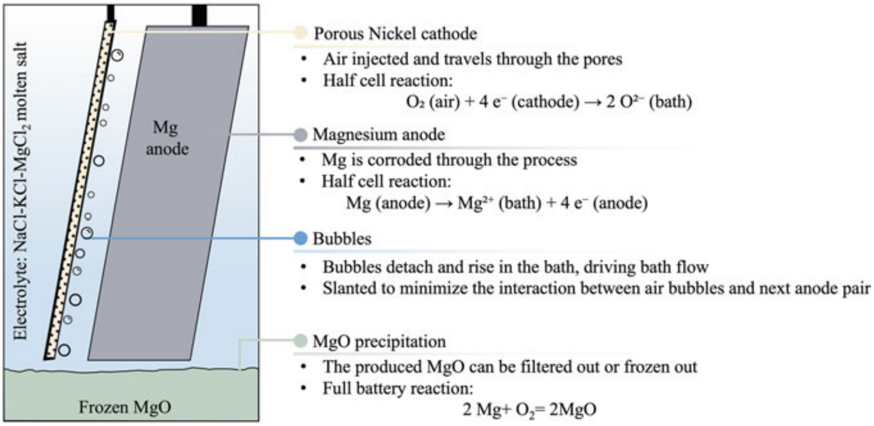

Porous Nickel cathode
- Air injected and travels through the pores
- Half cell reaction: O_2 (air) + 4 e^- (cathode) → 2 O^{2-} (bath)

Magnesium anode
- Mg is corroded through the process
- Half cell reaction: Mg (anode) → Mg^{2+} (bath) + 4 e^- (anode)

Bubbles
- Bubbles detach and rise in the bath, driving bath flow
- Slanted to minimize the interaction between air bubbles and next anode pair

MgO precipitation
- The produced MgO can be filtered out or frozen out
- Full battery reaction: $2\,Mg + O_2 = 2MgO$

Fig. 2 Mg-air battery setup

Mg-Air Battery Technology

The Mg-air battery presented here consists of the Mg metal anode, the air cathode, and the molten salt electrolyte as shown in Fig. 2. The molten salt electrolyte consists of NaCl–KCl–$MgCl_2$ with ~0.5% MgO solubility. Moreover, its eutectic temperature and Mg melting point bound the operating temperature range of 420–620 °C.

Cathode: O_2 (air) + 4 e^- (cathode) → 2 O^{2-} (bath).
Anode: Mg (anode) → Mg^{2+} (bath) + 4 e^- (anode) .
Total reaction: $2\,Mg + O_2 = 2MgO$.

Overview

This study discusses an Mg-air battery designed to address prior challenges. The modeling section of this study includes a numerical model elaborated to estimate the Voltage/Current relation of the cell. The experimental setup is then tested which showed the highest open-circuit voltage for an Mg-air battery to date: 1.9 V.

Materials and Manufacturing

Electrochemical Model

The energy balance modeling of the proposed Mg-air battery was calculated based on former solid oxide fuel cell studies [13–17]. Pure magnesium was used as the anode material and porous nickel was used as cathode. $MgCl_2$–NaCl–KCl (20-32-48 wt%) molten salt was used as the electrolyte. Due to deviations from modeled ideality, such as MgO product concentration in the electrolyte,, the actual cell voltage (V) is less than the theoretical open-circuit voltage [13], E_{th}, and illustrated in Eq. 1 where η shows the polarization and ΔV_{lead} shows the voltage loss from the leads. Moreover, Kakac et al. found these polarizations by categorizing them into three separate groups: activation polarization, ohmic polarization, and concentration polarization which are shown by η_{act}, η_{ohm}, and η_{conc}, respectively. The η_{act} is insignificant and ignored in this study. According to electromotive force (EMF), the theoretical open-circuit voltage can be calculated based on Gibbs's free energy of the cell reaction as shown in Eqs. 2 and 3.

$$V = E_{th} - \text{Losses} = E_{th} - \eta - \Delta V_{lead} \tag{1}$$

$$V = E_{th} - \eta_{act} - \eta_{ohm} - \eta_{conc} - \Delta V_{lead} \tag{2}$$

$$V = \frac{-\Delta G}{nF} - \eta_{act} - \eta_{ohm} - \eta_{conc} - \Delta V_{lead} \tag{3}$$

Furthermore, one can calculate the three polarizations using Eqs. 4–6. In the later equation, j_L is the limit current density of electrode which is calculated using Eq. 7.

$$\eta_{act} = \frac{RT}{nF}\left(\frac{1}{\alpha_a}\ln\left(\frac{j}{j_{0a}}\right) - \frac{1}{\alpha_c}\ln\left(\frac{j}{j_{0c}}\right)\right) \tag{4}$$

$$\eta_{ohm} = jASR_{ohm} \tag{5}$$

$$\eta_{conc} = \frac{RT}{nF}\left(1 + \frac{1}{\alpha_i}\right).\ln\left(\frac{j_L}{j_L - j}\right) \tag{6}$$

$$j = nF\frac{D\Delta C}{L} \tag{7}$$

Finally, the voltage corresponding to energy loss in the leads (ΔV_{lead}) is calculated using Eq. 8.

$$\Delta V_{lead} = 2\sqrt{L_{el}T\Delta T} \tag{8}$$

The parameters and assumptions used for this study are shown in Table 2 [16, 18]. Using this information, the limiting current density of anode and cathode was found as 7.72 and 2.92 A/cm^2, respectively. Oxygen consumption ratio and heat exchanger efficiency are model parameters assumed as 50% and 90%, respectively. Furthermore, the energy loss per cell was 0.04 V. As shown by Fig. 3, the $\frac{-\Delta H}{nF}$ value

Table 2 Battery performance model parameters

L	Thickness of electrode	0.5 cm
E_{th}	Theoretical open-circuit voltage	2.624195 mol
T0	Ambient temperature	293 K
T	Operating temperature	823 K
$D_{cathode}$	Diffusion coefficient of cathode	0.96 cm2/s
$C_{L,cathode}$	Limiting MgO molar density	3.94E-06 mol/cm^3
α_{MgO}	Charge transfer coefficients of MgO for cathode	2
α_{Mg}	Charge transfer coefficients of Mg for anode	2
n_{leads}	Number of leads	2
n_{cells}	Number of cells in a "stack"	10
AS R_{ohm}	Electrolyte area-specific resistance for ohmic polarization	$0.56\ \Omega \cdot cm^2$
OCR	Oxygen consumption ratio	50%
HEF	Heat exchanger efficiency	90%

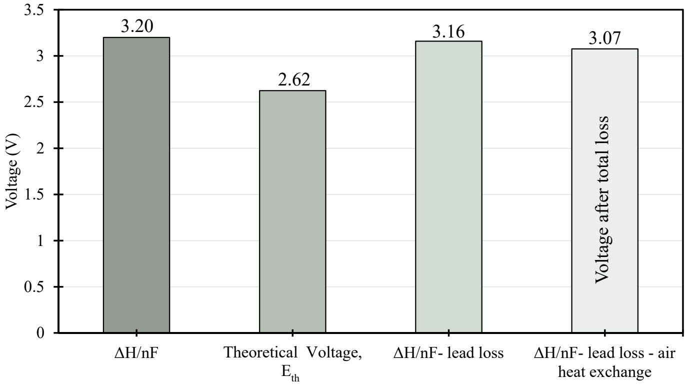

Fig. 3 The voltage loss through entropy, lead loss, and Mg and air heat exchange

for the designed cell was 3.2 V. The theoretical voltage was found as $\frac{-\Delta G}{nF} = 2.62$ V. Similarly, the voltage after lead loss and air heat exchange loss was found as 3.07 V.

High-Temperature Experimental Setup and Procedure

The high-temperature experiments explained in this section were designed as a proof of concept for the described Mg-air battery and to measure the open-circuit voltage (OCV) of the battery. Compared to the energy balance modeling, the voltage was expected to be around 2.6 V.

Figure 4 shows the experimental setup schematic. The salt ($MgCl_2$ 20 wt%, NaCl

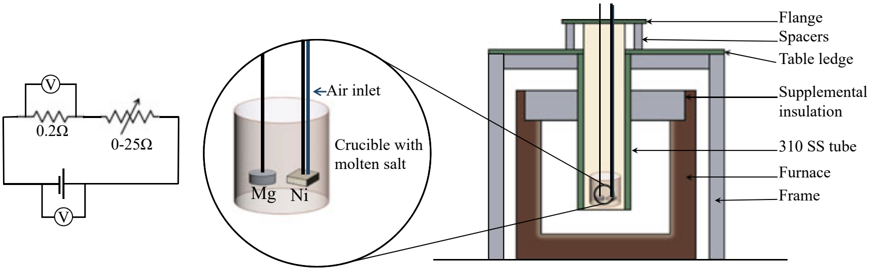

Fig. 4 Experimental setup for Mg-air battery

32 wt%, and KCl 48 wt%) was added to the crucible and placed into the furnace. The anode and cathode were set up to stay above the crucible at the start of the process. The Mg anode was in the shape of a cylinder with 2.5 cm diameter and 1.5–8 cm height. Nickel mesh, with a 2 cm^2 exposed area, was attached at the end of the cathode. Before the start of the experiment, the oxygen partial pressure of the chamber was verified to stay below 0.05 bar through injecting Argon gas. This prevented the burning of the graphite components as well as oxidation of the other components. The furnace temperature was then increased and kept at 450 °C to stabilize. Next, the temperature was ramped up to 500 °C and stabilized. Similarly, two more steps were taken to stabilize the temperature to 550 and 600 °C. All temperature ramping up rates in this experiment were 10 °C/min. The setup was ready to start the test once all the salt was molten. Then, the anode and cathode were inserted into the molten salt bath, air flow through the nickel mesh cathode began at 1 standard liter/minute, and the voltage and current were measured at variable resistance using the voltmeter. Both anode and cathode were drawn out of the bath before shutting off the furnace and ending the experiment.

Results and Discussion

Experimental Results

To identify the performance of the Mg-air battery discussed in this work, the voltages measured from the experiments were compared with modeling results and are shown in Fig. 5a. Figure 5b compares the calculated power from the experiments with the modeling results. As discussed in Section "Electrochemical Model", OCV expected from the cell was 2.62 V. As the current increases, the voltage decreases due to the concentration and ohmic polarization. The result from the electrochemical modeling illustrated that the Mg-air battery can operate under 0.5 A/cm^2 current density and 1.17 W/cm^2 power density at 73% efficiency. Similarly, 36% efficiency was achieved when operating under 2.5 A/cm^2 current density and 2.89 W/cm^2 power density.

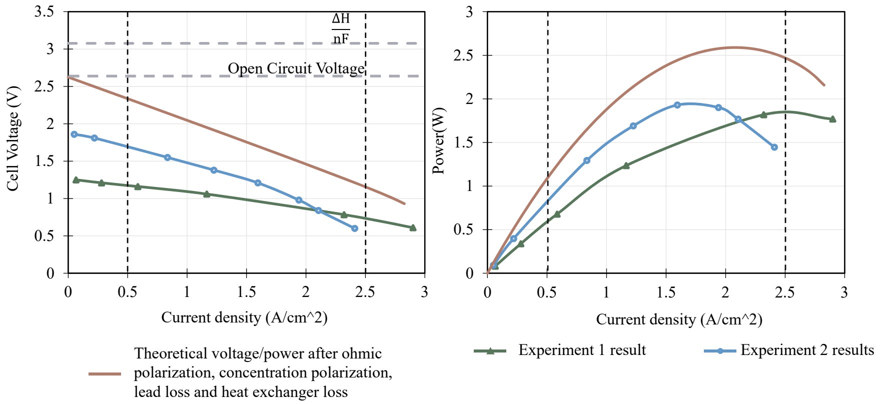

Fig. 5 Numerical and experimental results for Mg-air battery

The two experiments showed high accordance with the expectation from the model as shown in Fig. 5. The first experiment reached a very high current density of 2.9 A/cm^2 which is almost equal to the limiting current density (2.92 A/cm^2). Moreover, the second experiment reached 1.86 V which is 71% of the theoretical OCV. In both experiments, following the initial run, both OCV and current density fell over time. After each experiment, the nickel mesh cathode was partially blocked, with most pores filled with solid salt and some remaining open.

Discussion

The results found from the experiments of the Mg-air battery were aligned with the modeling expectations. This shows the proof of concept for the Mg-air battery. The designed Mg-air battery for transpacific zero-emission cruising will have a 20-foot standard shipping container with ten pairs of anodes and cathodes in series to increase the voltage and current produced while limiting the energy losses from cell leads. Such a battery could potentially deliver 90–120 MWh over up to 800 h (112–150 kW) at 60–80% efficiency, with the higher bound representing the model maximum OCV, and the lower bound representing the measured OCV in the second experiment above. This compares with just 3 MWh from the Tesla Megapack which is the highest-capacity containerized lithium-ion battery.

In the experiments, we believe that open-circuit voltage declined due to an increase in MgO concentration in the molten chloride electrolyte, and maximum current declined due to blockage of cathode pores by solidification due to cold input air. Future experiments will pre-heat incoming air and attempt to remove MgO from the electrolyte, in order to achieve long-term stable performance.

Summary and Conclusions

Key Findings

With global warming being one of the most critical challenges of today's world, this paper proposes an innovative Mg-air battery as an emission-free alternative to conventional energy sources. This work includes modeling and experimental investigation of Mg-air batteries. The key findings of this work are listed below:

- Mg-air batteries can provide the high-energy density required for long-haul transportation.
- The OCV of this battery was calculated as 2.62 V.
- Experiments were able to reach as high as 71% OCV of Mg-air battery.
- The maximum current density reached in the experiments was 2.9 which is almost equal to the modeling expectations.
- At 73% of efficiency, the Mg-air battery is expected to operate under 0.5 A/cm^2 current density and 1.17 W/cm^2 power density.
- At a current density of 2.5 A/cm^2, power increases to 2.89 W/cm^2, but efficiency falls to 36%.
- For reaching the highest performance of the battery, MgO concentration should be kept as low as possible in the electrolyte. This can be achieved by either freezing the MgO from the bottom or filtering it out.

Future Work

The current set of tests was designed to illustrate the applicability of the theoretical Mg-air battery concepts. This setup did not include a mechanism to remove MgO. However, such a system will be included in the next set of tests to lower MgO concentration in the electrolyte. Following that, it will be important to demonstrate the ability to recharge this battery system.

References

1. Yoshio M, Brodd RJ, Kozawa A (eds) (2009) Lithium-Ion batteries. Springer New York, New York, NY. https://doi.org/10.1007/978-0-387-34445-4
2. Tong F, Wei S, Chen X, Gao W (2021) Magnesium alloys as anodes for neutral aqueous magnesium-air batteries. J Magnes Alloy S2213956721001146. https://doi.org/10.1016/j.jma.2021.04.011
3. Blurton KF, Sammells AF (1979) Metal/air batteries: their status and potential—a review. J Power Sources 4(4):263–279. https://doi.org/10.1016/0378-7753(79)80001-4
4. Wang H-F, Xu Q (2019) Materials design for rechargeable metal-air batteries. Matter 1(3):565–595. https://doi.org/10.1016/j.matt.2019.05.008

5. Multi-Gas Contributors to Global Climate Change (2003) Center for climate and energy solutions, 20 Feb 2003. https://www.c2es.org/document/multi-gas-contributors-to-global-climate-change/. Accessed 01 Sept 2021
6. Zhang Q et al (2018) Exposure to alumina nanoparticles in female mice during pregnancy induces neurodevelopmental toxicity in the offspring. Front Pharmacol 9:253. https://doi.org/10.3389/fphar.2018.00253
7. Faegh E, Ng B, Hayman D, Mustain WE (2020) Practical assessment of the performance of aluminium battery technologies. Nat Energy 1–9. https://doi.org/10.1038/s41560-020-00728-y
8. Pei P et al (2019) A high-energy-density and long-stable-performance zinc-air fuel cell system. Appl Energy 241:124–129. https://doi.org/10.1016/j.apenergy.2019.03.004
9. Licht S, Cui B, Stuart J, Wang B, Lau J (2013) Molten air—a new, highest energy class of rechargeable batteries. Energy Environ Sci 6(12):3646. https://doi.org/10.1039/c3ee42654h
10. Peng C et al (2018) A rechargeable high-temperature molten salt iron-oxygen battery. Chemsuschem 11(11):1880–1886. https://doi.org/10.1002/cssc.201800237
11. Cui B, Licht S (2014) A low temperature iron molten air battery. J Mater Chem A 2(27):10577–10580. https://doi.org/10.1039/C4TA01290A
12. Czelej et al (2017) Atomistic insight into the electrode reaction mechanism of the cathode in molten carbonate fuel cells. J Mater Chem 5(26):13763–13768
13. Kakac S, Pramuanjaroenkij A, Zhou X (2007) A review of numerical modeling of solid oxide fuel cells. Int J Hydrog Energy 32(7):761–786. https://doi.org/10.1016/j.ijhydene.2006.11.028
14. Ni M, Leung MKH, Leung DYC (2006) A modeling study on concentration overpotentials of a reversible solid oxide fuel cell. J Power Sources 163(1):460–466. https://doi.org/10.1016/j.jpowsour.2006.09.024
15. Kim-Lohsoontorn P, Bae J (2011) Electrochemical performance of solid oxide electrolysis cell electrodes under high-temperature coelectrolysis of steam and carbon dioxide. J Power Sources 196(17):7161–7168. https://doi.org/10.1016/j.jpowsour.2010.09.018
16. Rutherford M, Telgerafchi AE, Espinosa G, Powell AC, Dussault D (2021) Low-cost magnesium primary production using gravity-driven multiple effect thermal system (G-METS) distillation. In: Magnesium 2021, Orlando, Florida, pp 139–144. https://doi.org/10.1007/978-3-030-65528-0_21
17. O'Hayre R, Cha S-W, Colella W, Prinz FB (2021) Fuel cell fundamentals, 3rd edn. Wiley, 2016. Accessed 06 Sept 2021. https://www.wiley.com/en-us/Fuel+Cell+Fundamentals%2C+3rd+Edition-p-9781119113805
18. Kisza A, Kazmierczak J, Børresen B, Haarberg GM, Tunold R (1997) Kinetics and mechanism of the magnesium electrode reaction in molten MgCl2–NaCl binary mixtures. J Electrochem Soc 144(5):1646. https://doi.org/10.1149/1.1837654

Part II
Energy Efficiency, Decarbonization and CO_2 Management

Circored Fine Ore Direct Reduction Plus DRI Smelting: Proven Technologies for the Transition Towards Green Steel

Sebastian Lang, Timo Haimi, and Max Köpf

Abstract The hydrogen-based direct reduction of iron ore combined with EAF smelting is being widely discussed as a possible replacement for the commonly used BF/BOF route in steelmaking when targeting carbon footprint reduction. One alternative to shaft furnaces is Metso Outotec's Circored process, which uses fine ore as feed for fluidized bed reactors, eliminating the cost and energy-intensive pelletizing step. As a direct reduction process using 100% hydrogen as the reductant, Circored has already proven its functionality in an industrial-scale demonstration plant. Direct charging of hot DRI to a smelter would further increase the energy efficiency of the process. Metso Outotec's rectangular six-in-line smelting furnace combines a flash smelter body and the Söderberg electrodes. This DRI smelting solution can replace small/medium-sized BFs and produce hot metal with the desired carbon content in existing steel plants with BOF converters. The large furnace volume enables the processing of low-grade iron ore with high gangue content and thus the use of BF-grade feed for DRI production.

Keywords Iron and steel · Environmental effects · Process technology

Introduction

In 2019, the United Nations announced that over 60 countries had committed to carbon neutrality by 2050 [1]. The European Green Deal, proclaimed in March 2020, translated this declaration into a legally binding target, significantly accelerating the dynamics for the development of carbon–neutral or green steelmaking technologies.

About 70% of the world's steel is produced via the blast furnace/basic oxygen furnace (BF/BOF) route, an efficient but highly carbon-intensive production method.

S. Lang (✉) · M. Köpf
Metso Outotec, GmbH & Co KG, An den Schwarzwiesen 13, 61440 Oberursel, Germany
e-mail: sebastian.lang@mogroup.com

T. Haimi
Metso Outotec Oy, Rauhalanpuisto 9, 02231 Espoo, Finland

F. Tesfaye et al. (eds.), *REWAS 2022: Energy Technologies and CO_2 Management (Volume II)*, The Minerals, Metals & Materials Series,
https://doi.org/10.1007/978-3-030-92559-8_7

With this process, on average 1.8 tons of CO_2 are produced for every ton of crude steel. In total, the steel industry is responsible for about 8% of global CO_2 emissions [2].

With limited investment cycles left until 2050, the steelmaking industry must decide within the next five to ten years which alternative technology for the reduction of iron ore to invest in. One widely discussed alternative to traditional carbon-intensive BF/BOF steelmaking is the hydrogen-based direct reduction of iron ore combined with electric arc furnaces (EAF). Most of the current projects focus on applying shaft furnaces for direct reduction with hydrogen. However, applying this method will generate the need for several hundred million tons of additional high-quality DR-grade pellets annually, with the associated impacts on the demand on high-grade iron ore concentrates, pellet availability, and consequently pellet prices.

An alternative is hydrogen-based direct reduction using fine ore instead of pellets. Metso Outotec's Circored technology is the first process for iron ore reduction based on 100% hydrogen and has proven its functionality and performance in an industrial-scale demonstration plant.

In addition, Metso Outotec has a proprietary technological solution for direct reduced iron (DRI) smelting in a six-in-line furnace, which links the new developments to the existing processing infrastructure of steel plants.

As the frequently discussed steelmaking route direct reduction in shaft furnaces followed by EAF steelmaking relies on the use of very clean raw material, it is evident that this will increase the already visible shortage of high-quality, clean raw material. The Metso Outotec DRI smelting furnace to produce hot metal would be able to handle large slag volumes without excess Fe-unit losses, thereby allowing the use of lower-quality raw materials. As a continuously operating process, this solution would secure constant production at the steel plant. By combining Circored with smelting and feeding the hot DRI product from Circored directly into a smelting furnace, the energy efficiency of the process route can be further improved.

This concept is new in the global framework and can be very competitive regarding both investment costs and technological risks and is an important enabler in decarbonizing steel production, thus contributing directly to the transition towards green steel.

In this paper, the principle of the Circored process and the results of the demonstration plant operation are described. The paper also introduces the six-in-line furnace technology and its possible application to treat low-grade iron ores. Finally, the possible role of the Circored process and DRI smelting in the industry's transition toward green steel will be outlined.

The Concept

Advantages of Fluidized Bed Technology

Metso Outotec has been involved in the direct reduction of iron ore (Lurgi legacy) since this technology was first introduced as one of the inventors of the SL/RN-process based on the rotary kiln and as a successful licensee of the Midrex shaft furnace process.

Circored is based on fluidized bed technology, which Metso Outotec has been leading the development of for several decades. The technology is state of the art for processes such as coal combustion in a circulating fluidized bed (CFB) with inherent SO_2 absorption and alumina calcination; in these applications, a CFB is used in place of rotary kiln technology because of the significantly lower energy consumption and lower CAPEX and maintenance costs.

The main advantages of fluidized bed processes are excellent heat and mass transfer conditions, precise temperature control, short solids retention times leading to higher plant capacities, and lower investment and operating costs.

The technology can also be applied for the direct reduction of iron ore to eliminate the cost and energy-intensive agglomeration step of iron ore fines in the form of sintering or pelletizing.

The Circored Process

The generic Circored process is based on the reduction behavior of iron ore, shown in Fig. 1.

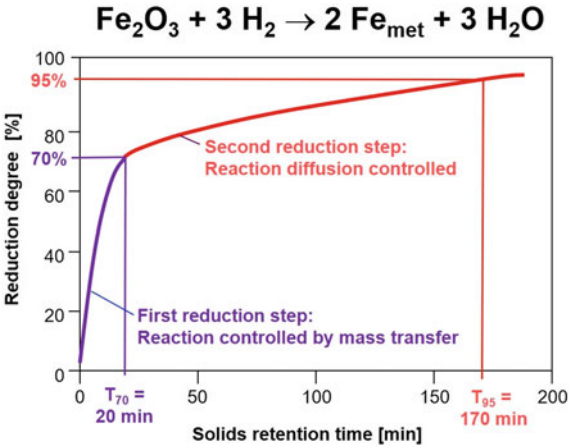

Fig. 1 Performance of H_2-based direct reduction process in fluidized beds

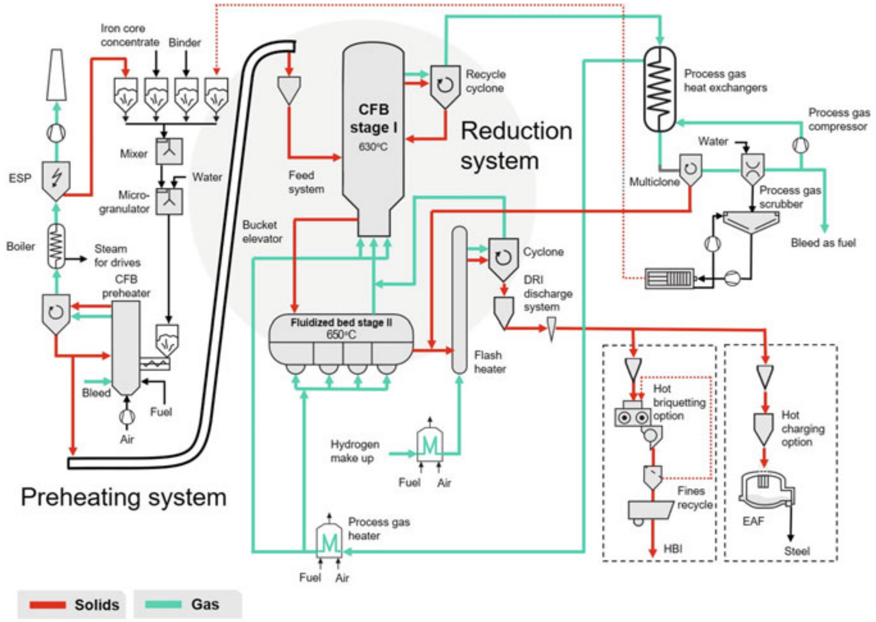

Fig. 2 A simplified process flow diagram of the Circored process including microgranulation

For the direct reduction of fine iron ore, Circored applies a two-stage reactor configuration with a CFB followed by a bubbling fluidized bed (FB) downstream. Below is a brief description of the Circored process, which is also visualized in the simplified process flow diagram in Fig. 2.

The preferred grain size for the process is 0.1–2.0 mm, though depending on decrepitation behavior, a grain size of up to 6 mm might also be acceptable. Ultrafine concentrate and in-plant fines can be microgranulated. The iron ore fines are dried and preheated in a CFB preheater to a temperature of approximately 850–900 °C before being introduced into the first-stage CFB reactor.

The initial reduction step is fast and controlled by the outer mass transfer of the reductant to the iron oxide particle. The CFB is the ideal reactor to achieve a prereduction degree of 65–80%, offering the following characteristics: high gas velocities of 4–6 m/s and high differential velocities between gases and solids leading to short solids retention times of 20–30 min, and the optimum lateral and vertical mixing of solids and gases ensuring uniform temperature distribution throughout the reactor.

For processing ultrafine ores (<50 μm) or scrubber dust, Metso Outotec has a patented a very simple microgranulation process. In this process, the ultrafine particles are agglomerated to microgranules to an average size of approximately 350 μm with the addition of a binder. The process does not require any additional heat-hardening equipment as the hardening of the granules takes place in the preheating section of the Circored plant (also shown in Fig. 2).

After prereduction, the material is discharged into the secondary FB reactor, which is compartmentalized for better process control. For the prolonged diffusion-controlled final reduction step, the bubbling FB reactor offers optimum conditions for achieving reduction degrees in excess of 93–95%, with low gas velocities of 0.5–0.6 m/s and longer solids retention times of 60–180 min depending on the nature of the ore. Operation at 4 bar(a) avoids the excessive equipment and piping costs that would result from large gas volumes needing to be recycled within the process.

For the Circored process, hydrogen was selected as the sole reducing agent. Its specific reduction reaction temperature characteristic lowers the temperature of the process to 630–650 °C and avoids particle sticking in the reduced material. Because of this, at the time of its development, hydrogen was the enabler for a new process; today, with the steel industry under pressure to decarbonize, the use of hydrogen as the sole reductant is much more significant. One could say that the hydrogen-based Circored process was developed 20 years too early.

For better briquetability, the reduced fines, which are discharged from the FB reactor at a temperature of about 630–650 °C, are heated in a flash heater up to about 700–720 °C, where preheated make-up hydrogen is utilized for heating and transporting the reduced fines to the top of the continuous discharge system.

Within the discharge system, the hydrogen atmosphere is gradually replaced by nitrogen and the pressure lowered to atmospheric level, thereby ensuring safe conditions for briquetting. A minimum briquetting temperature of around 680 °C is required to obtain high-density hot briquetted iron (HBI, >5.0 g/cm^3).

As the reduction of iron ore with hydrogen is an endothermic reaction, the energy must be supplied by heating both the ore and recycled gases. In the past, this was done using natural gas and process gas bleed. To achieve a totally carbon emission-free process, it is now foreseen to replace natural gas with electric heating by (green) power using renewable sources.

The off-gas from the recycle cyclone of the CFB reactor is passed through a process gas heat exchanger and a multiclone to recover ultrafine dust particles, which are recycled. The off-gas is then scrubbed and quenched simultaneously to remove any dust and water produced during reduction. The cooled and cleaned process gas is then recompressed and subsequently preheated to a temperature of approximately 750 °C before being reintroduced into the reactor system.

A further significant advantage of the CFB reactor is the ability to inject dust-laden, partially reacted gas from the second-stage FB reactor, which creates a counter-current flow of gases and solids throughout the dual-reactor system. This has a two-fold advantage: the nozzle grate of the CFB reactor is only exposed to clean recycled process gas, thereby minimizing nozzle wear, and the overall gas utilization of the entire process is maximized. The Circored process generates no residues or relevant emissions besides water and unavoidable heat release.

Key features of the Circored process

- Preheating the iron ore fines to 850–900 °C in a separate CFB reactor for calcining prior to charging in the primary CFB reduction stage. This method also allows the processing of magnetite ores, which can be difficult to reduce as the preheating stage oxidizes the magnetite to hematite. In addition, the microgranules produced can be hardened to avoid the generation of ultrafine particles in the reduction stage
- Prereduction in a CFB in about 20–30 min to a reduction degree of 65–80%
- Final reduction in a compartmentalized FB reactor to 93–95% reduction
- The use of hydrogen as the sole reductant enables low temperatures of 630–650 °C in the CFB and the FB; this low temperature avoids particle sticking and means that the reaction is easy to control
- A zero-carbon process variant is possible with electrical heating from renewable sources to provide the energy for the endothermic reduction reactions.

Comparison of Different Steelmaking Routes

When comparing the Circored/EAF steelmaking route with other state-of-the-art routes, especially in terms of CO_2 emissions and cost, common battery limits need to be defined. We look here at the conversion of an iron ore concentrate to raw steel with all the required intermediate steps, forming the references for this comparison (see Fig. 3). Both Circored and shaft furnace direct reduction technologies produce

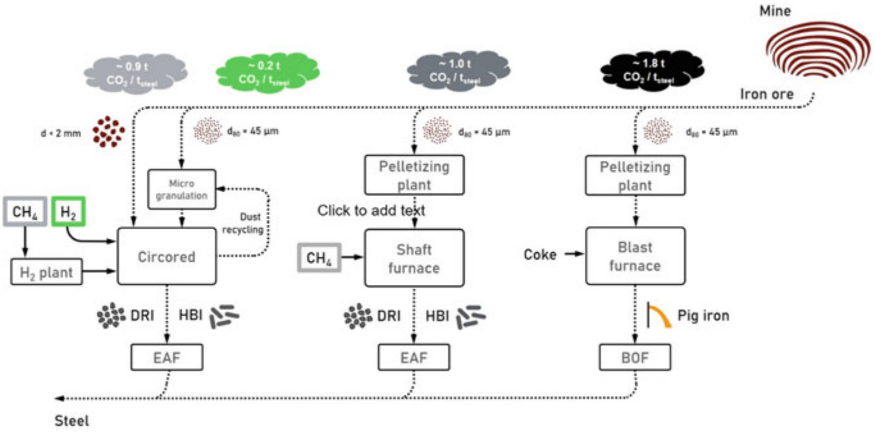

Fig. 3 A comparison of the main components, feeds, and products of different steelmaking routes

DRI or HBI that can be used directly in an EAF. The product from the blast furnace, pig iron, is fed to an oxygen converter (BOF). These downstream processes are considered in the CO_2 and cost figures.

Generally, the Circored process can handle feeds with a particle size of up to 2 mm; depending on the decrepitation behavior, particle sizes of up to 6 mm are possible. If an ultrafine concentrate is used, a microgranulation step should be applied to make the material fluidizable. Along with this option comes the opportunity to recycle any kind of dust or fines originating at different points in the plant. The Circored process uses a natural gas reformer to provide the hydrogen for reduction. For future scenarios, we further included a Circored + process variant that applies green hydrogen produced from renewable sources for direct reduction and electrical heaters for drying and preheating.

It is apparent that the BF/BOF route is by far the largest emitter of CO_2; furthermore, the technical solutions to minimize emissions are limited for this route. While the CO_2 emissions of the Circored process and shaft furnace direct reduction are in the same order of magnitude, Circored benefits from the omission of the pelletizing step. As the Circored + process is designed to produce fully green steel, the CO_2 emissions of the reduction process are negligible.

When it comes to cost, Circored is a very competitive route, partly because the CO_2 taxes are lower than for the BF/BOF route and because there is no pellet premium (versus the shaft furnace route). In terms of CO_2 emissions and cost, the ‘regular’ Circored process is already competitive today, and the Circored + variant is predicted to be even more so.

The Circored Plant in Trinidad

There were two main drivers for the development of the Circored process: the growing demand for a direct reduction process utilizing iron ore fines directly to decrease HBI production cost by avoiding a costly agglomeration step, and Lurgi’s desire to apply its vast experience of utilizing fluidized bed technology also for direct reduction.

After an extensive period of test work and process development, the investigations showed that the use of pure hydrogen as a reducing agent in a two-reactor (CFB and FB) combination would ideally suit the direct reduction characteristics of iron ore fines. Shortly after finishing test work and a conceptual engineering study, a contract for the first Circored plant, to be built in Trinidad, was awarded by Cliffs and Associates Limited in 1996. The plant started operation in May 1999; after the discharge system was modified, it reached its process design parameters in March 2001 and was operating at up to 105% of its design capacity.

Despite functioning normally, the plant was unfortunately idled after a short period of successful operation, which produced 300,000 tons of high-quality HBI. This was due to several changes in ownership and to economic and political reasons including steel-market developments and the lack of availability of natural gas. The Trinidad

Fig. 4 Trinidad plant with HBI stockpile

plant shown in Fig. 4 fulfilled process expectations in terms of a high and uniform degree of metallization achieved from the outset.

Key achievements of the Circored plant in Trinidad

- Over 300,000 tons of high-quality HBI were produced and were subsequently processed in electric arc furnaces located in the US.
- Plant design HBI production of 63 t/h periodically exceeded.
- High HBI product quality with maximum metallization degrees greater than 95% and constant briquette densities above 5.2 g/cm^3.

DRI Smelting

By utilizing the existing products and wide experience of the Metso Outotec Ferroalloys and Non-Ferrous Smelting organization, a new solution has been developed for smelting DRI that has been produced from low-grade iron ore to produce hot metal for further use in BOFs. Such DRI feed would be a challenge for standard steelmaking EAFs because of the excess slag volume, which causes unacceptable losses of Fe-units to the slag. In addition, incorporating this type of process into existing steel plant facilities using BOF converters can be a challenge, at least on a larger scale and for more demanding steel grades.

The Metso Outotec solution therefore aims to replace the blast furnace and achieve continuous production of suitable hot metal quality for an existing steel plant, to enable the use of existing BOF converters. The main idea is to use a closed EAF for the smelting of the pre-reduced iron ore feed (DRI from Circored). For fossil-free production, sustainable sources of carbon reductant would be needed for the smelting furnace, since the final reduction takes place there.

The main driver of this solution is that there is no need to use high-quality DRI-grade pellets or to increase usage of external (high-quality) scrap. It can use DRI produced from standard BF-grade pellets by direct reduction in a shaft furnace or Circored-DRI produced from low-grade iron ore fines and even utilize recycling of waste material like dust briquettes. Also, the slag can be modified to remove impurities and achieve the desired slag chemistry, targeting very good metal yields and good-quality slag products that can be used as raw materials by the cement industry. Furnace off-gas can be either utilized as combustible off-gas (in a similar way to coke oven gas/blast furnace gas in the possible existing power plant) or combusted to produce steam for other heating purposes.

The Metso Outotec DRI smelting furnace design uses six self-baking Söderberg electrodes, which are standard in ferroalloy and non-ferrous processes. The furnace body is familiar from flash smelting furnaces. Therefore, all equipment is proven technology and has many reference projects. Figure 5 shows an illustration of the furnace.

The feed can be fed into the feed bins on top of the smelting furnace, either hot or cold. There are several possibilities for the feeding system, but the most commonly used systems are conveyors and buckets. The hot feeding is highly efficient in terms of electrical energy consumption since a feed temperature of < 600 °C reduces specific smelting electrical energy consumption by as much as 20%. In case of hot feed, the reductants and fluxes need to be fed from separate bins to the hot DRI.

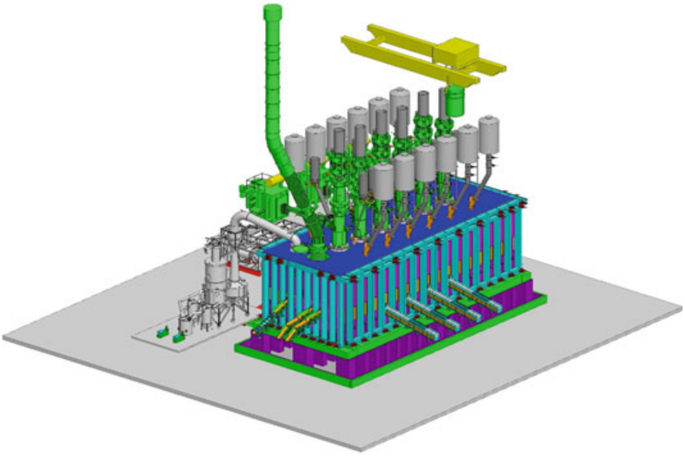

Fig. 5 The Metso Outotec DRI smelting furnace design

Table 1 Features and benefits of the Metso Outotec DRI smelting solution

Furnace feature	Benefits
Flexible feed systems	Allows a wide variety of feed materials to be used (HDRI, CDRI, HBI), reductants, fluxes, briquettes
Continuous process	High availability, similar to blast furnace
Blast furnace type hot metal	Only small adjustments needed to existing steel plant logistics
Large furnace volume	Enables high material flow and BF-grade pellets
	Can be used as a buffer
No need for extra scrap	Low level of tramp elements
Gastight construction	Low level of gaseous impurities
Long retention time	High metal yields
Separate metal/slag tap-holes	Optimal metal/slag separation
Black-top operation	Decreased heat flow to the roof
Spring-loaded furnace refractories	Expansion is easy to control
Six electrodes	Smaller electrodes needed; more active area, less passive area
Direct slag granulation from launders	No need for slag pots

The furnace is lined with refractories and cooled with water via different copper cooling elements. Table 1 describes the key features of the Metso Outotec DRI smelting solution and their respective benefits.

The carbon and silicon levels of the hot metal produced with the furnace need to be configured to the needs of each steel plant. Additionally, all DRI pellets use different iron ore feeds, which means that the solution needs to be optimized according to the needs of each individual steel plant.

Perspectives

Since the design, erection, and operation of the first Circored plant in Trinidad, numerous modifications to the original setup were investigated and developed:

- Plant capacity increased to 1.25 Mt/y per line, now considered the technical and economical optimum for an industrial-scale plant.
- Replacing natural gas with green electricity for preheating to achieve complete carbon neutrality.
- Microgranulation: for processing ultrafine (<50 μm) ores and scrubber dust, Metso Outotec has patented a very simple microgranulation process. In this process, the ultrafine particles are agglomerated to microgranules to an average size of approximately 350 μm with the addition of a binder. The process does not

require any additional heat-hardening equipment as the hardening of the granules takes place in the preheating section of the Circored plant.

- Direct feeding of hot DRI into an EAF to further improve energy efficiency.
- For low-grade iron ores, a combination of a single reduction stage Circored process (metallization degree of 75–85%) with smelting reduction in an electric smelter for hot metal production is feasible.

Circored technology is flexible in its production setup. Besides merchant cold HBI, which can easily be shipped, hot and cold DRI can be produced and directly linked to EAFs and BOFs as a substitute for hot metal and/or other virgin iron units. This guarantees the production of the high-quality steel products that have traditionally been the strength of integrated steel plants.

From discussions with clients, it became obvious that—at least for the transition period in existing steel plants—the feed material for the EAF is expected to be a mixture of different materials like HBI, DRI, and scrap. The carbon content can be adjusted to the required level in the EAF operation.

With the Circored process, Metso Outotec provides an alternative process route for the reduction of iron ores, using hydrogen as the sole reductant and fine ore instead of pellets as feed material. Circored is currently the only process for iron ore direct reduction based on pure hydrogen and has proven its functionality and performance in an industrial-scale demonstration plant with a capacity of 500,000 t HBI/y.

Conflict of Interest The authors declare that they have no conflict of interest.

References

1. Climate Action Summit (2019) Report of the secretary-general on the 2019 climate action summit and the way forward in 2020, UN.org
2. World Steel Association

Treatment of an Indigenous Lepidolite Ore for Sustainable Energy Considerations

Alafara A. Baba, Daud T. Olaoluwa, Kuranga I. Ayinla, Abdullah S. Ibrahim, Ayo F. Balogun, Sadisu Girigisu, Oluwagbemiga M. Adebola, and Jumoke Fasiku

Abstract Increased usage of lithium in lithium-ion batteries to power portable electronic devices as well as electric vehicles has resulted in a considerable global increase in demand for the metal. Consequently, the treatment of a Lepidolite ore was investigated for lithium extraction and purification through a combination of sodium carbonate roasting and water leaching. Various parameters such as ore: salt ratio, roasting temperature, and reaction time were studied. Experimental results showed the formation of various compounds as the roasting + water leaching process proceeded, yielding 91.2% lithium extraction efficiency, subsequently beneficiated to produce 99.1% pure *Zabuyelite* (Li_2CO_3: 83–1454, *m.p.* 720 °C). The product as characterized could be used as a precursor in lithium-ion batteries.

Keywords Lepidolite · Lithium · Leaching · Lithium batteries · Sustainable energy

Introduction

In view of its unique electrochemical and other properties, lithium has become cardinal as an anode material in lithium batteries [1, 2]. As a result of these properties, lithium has found its peak application in Li-ion batteries, which represents the

---

A. A. Baba (✉) · D. T. Olaoluwa (✉) · K. I. Ayinla · A. S. Ibrahim · A. F. Balogun · S. Girigisu · O. M. Adebola · J. Fasiku
Department of Industrial Chemistry, University of Ilorin, P.M.B. 1515, Ilorin 240003, Nigeria
e-mail: alafara@unilorin.edu.ng

D. T. Olaoluwa
Department of Science Laboratory Technology, The Federal Polytechnic, P.M.B. 231, Ede, Nigeria

A. F. Balogun
Department of Chemistry, Kogi State College of Education (Technical), P.M.B. 242, Kabba, Nigeria

S. Girigisu
Department of Science Laboratory Technology, The Federal Polytechnic, P.M.B. 420, Offa, Nigeria

F. Tesfaye et al. (eds.), *REWAS 2022: Energy Technologies and CO_2 Management (Volume II)*, The Minerals, Metals & Materials Series,
https://doi.org/10.1007/978-3-030-92559-8_8

major and fastest growing industrial application. Demand for this element results from the increased production of mobile electronic devices and the diversification of electric vehicles (EVs) [3]. Presently, the primary sources of lithium are ores and brine deposits. The brine exploration has been given more attention so far because the brine deposits are available and necessitate substantially lower operating costs [4, 5]. This has, however, resulted in the extraction of most of the Li-bearing minerals, like spodumene, lepidolite, and petalite, together with other silicates, being neglected. With the increasing interest in lithium, these sources are again taken into consideration for producing lithium compounds with high purity [6–8].

Different hydrometallurgical routes have been developed to extract lithium from lepidolite but because of the very refractory nature of Li-bearing silicates to chemical attack, the best of these routes involves roasting techniques such as chlorination roasting, sulfate roasting, limestone roasting, and sulfuric acid leaching. These methods work on the principle of a displacement reaction by roasting at moderated energies with some additives, i.e. chloride, sulfate, limestone, or digestion with concentrated sulfuric acid followed by leaching, to obtain a lithium-bearing solution [5, 9–15]. Consequently, the present study treated an indigenous Nigerian sourced lepidolite ore by moderate carbonate roasting and water leaching to obtain a product that could be used as a precursor in lithium-ion batteries while studying the ore: salt ratio, roasting temperature, and reaction time as the process progresses.

Materials and Methods

Materials

The lepidolite ore samples for this study were sourced from the Awe Local Government Area of Nassarawa State, Nigeria, through Ibrag Nigeria Limited, Ilorin, Nigeria. The sample was crushed, milled, and levigated into different particle dimensions ($-57 + 63$ μm, $-63 + 75$ μm, and $-75 + 90$ μm) using the ASTM standard sieves. The levigated samples were characterized using the Spectro Arcos ICP-OES equipped with the ORCA Optical System; MINI PAL 4 EDXRF spectrometer; and EMPYREAN X-ray diffractometer and scanning electron microscopy (SEM) model Leo1450 with LaB6 filament to determine the elemental composition, material purity, and the structural morphology of the ore, respectively.

Leaching and Dissolution Process

Lithium extraction was carried out by first mixing the ground ore sample with sodium carbonate at different molar ratios and then roasting at different temperatures for 1 h in a Carbolite CWF 3000 muffle furnace. After roasting, calcines were cooled to ambient temperature (27–29 °C), finely ground, and then water leached [12, 16–18].

Treatment of Roasted Products

The cooled and finely ground calcines were leached in a 250-mL, three-neck flask glass reactor connected with a condenser pipe and agitated by a mechanical stirrer with a temperature control unit that keeps the reaction temperature constant. All the experiments were conducted in batches with a solid-to-liquid ratio of 10 g/L. After the reaction, the slurry was separated by filtration and the leaching residue was washed, dried, and weighed. Selected residues after appropriate treatments were fully characterized [18, 19].

Results and Discussion

The elemental analysis by ICP-OES and EDXRF showed the ore sample to be made up of 12.75% Al_2O_3, 29.74% SiO_2, 0.43% P, 9.02% K, 3.64% Rb, and 1.60% Li, while the XRD as presented in Fig. 1 showed the main phases present in the ore sample as lepidolite (96–900–0629), albite (96–900–1633), and quartz (96–901–2604).

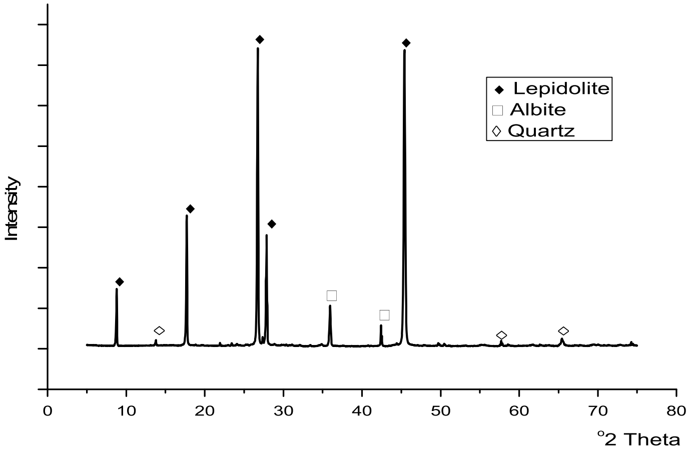

Fig. 1 XRD of raw lepidolite ore

Roast Leaching Studies

The mixture ratio of the lepidolite + Na_2CO_3 was studied over a range of 1:1 to 1:4 at 500 °C for 60 min. The calcines were then cooled and ground with subsequent leaching with distilled water for 120 min at 75 °C. The leaching results are summarized in Fig. 2 where L represents the % leached and R as the % residue obtained.

As shown in this figure, the results confirm the favorable influence of roasting on the leachability of Li from lepidolite as the leachability increases dramatically with an increase of the mixing ratio. The leachability increased steadily to 76.1% as the mixing ratio reached 1:3 and, subsequently, decreased slightly to 72.2% as the mixing ratio was adjusted to 1:4, even though the roasting temperature and leaching conditions remained constant.

A range of roasting temperatures from 500 to 900 °C was chosen for investigation while the leaching time (60 min) remained constant. The results shown in Fig. 3 indicate that roasting temperature has a considerable influence on lithium extraction. The extraction rate of lithium had its peak at 750 °C and then decreased. This could be attributable to the fact that as the roasting temperature increased, less leachable lithium compounds probably formed.

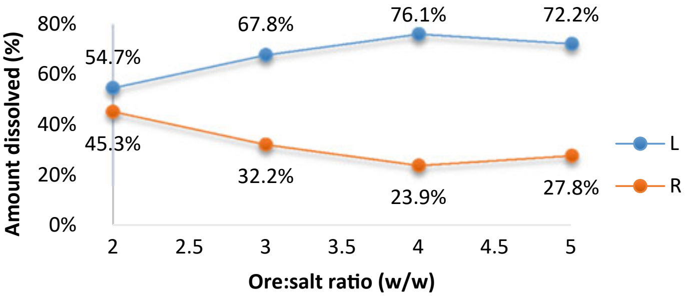

Fig. 2 Effect of lepidolite: Na_2CO_3 ratio (w/w)

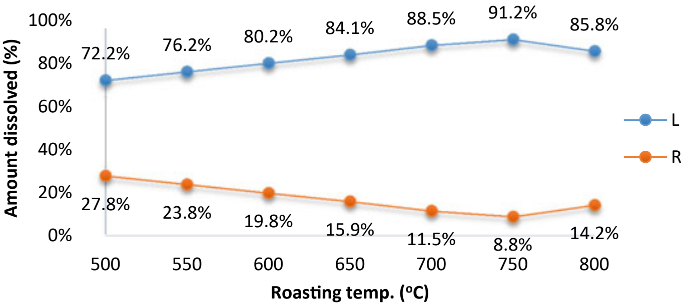

Fig. 3 Effect of roasting temperature

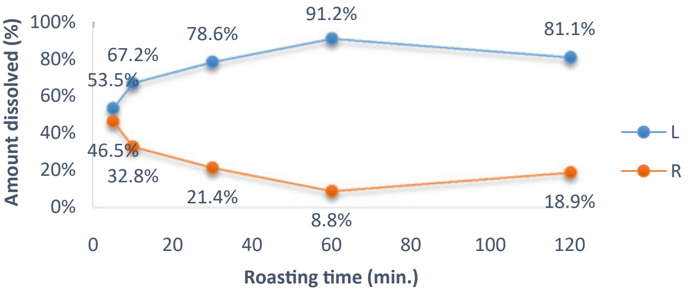

Fig. 4 Effect of roasting time

The effect of roasting time on lithium leachability at a fixed molar ratio of Li: Na_2CO_3 (1:3) (Fig. 4) showed similar trends to those of leachability at different roasting temperatures. As the roasting time increased, the efficiency of lithium extraction improved. However, there appeared a sharp decline at 120 min with the lithium recovery rate dropping to 81.1%. Therefore, the optimal roasting and leaching conditions were set at lepidolite: Na_2CO_3 molar ratio of 1:3, roasting temperature and time of 750 °C and 60 min, respectively, and leaching temperature and time of 75 °C and 120 min, respectively.

Residual Analysis

XRD analysis was performed to evaluate the components of the roasted samples. Figure 5 shows the XRD patterns of the ore and Na_2CO_3 after roasting with a molar ratio of Li: Na_2CO_3 of 1:3 at different roasting conditions. At a roasting temperature of 500 °C, the main components of the unleached sample + Na_2CO_3 (Fig. 5A) were Lepidolite (JCPDS file no. 96–900–0025), Calcite (JCPDS file no. 96–900–9668), and Quartz (JCPDS file no. 96–901–1496). In addition, peaks of Sanidine (JCPDS file no. 96–901–0842), Nepheline (JCPDS file no. 96–100–8762), and Lepidolite (JCPDS file no. 96–900–0835) appeared when the roasting temperature was increased to the optimum 750 °C (Fig. 5B) owing to phase transition at higher temperatures. Accordingly, after water leaching, the XRD pattern of the product (Fig. 5C) by the evaporation of the leaching solution gave peaks that correspond solely to Zabuyelite (JCPDS file no. 96–83–1454). This signifies that the whole process has successfully transformed the sample into a lithium-containing product.

The SEM image of the initial sample +Na_2CO_3, after being reground by a planetary ball mill, is shown in Fig. 6A, where it is seen that the particles exhibit a large unsmooth surface. Figure 6B shows that the calcined mixture after processing now possesses smaller, uneven, and porous surfaces, evidence of the complete and successful extraction and conversion of the lepidolite into an easily broken-down lithium-containing structure.

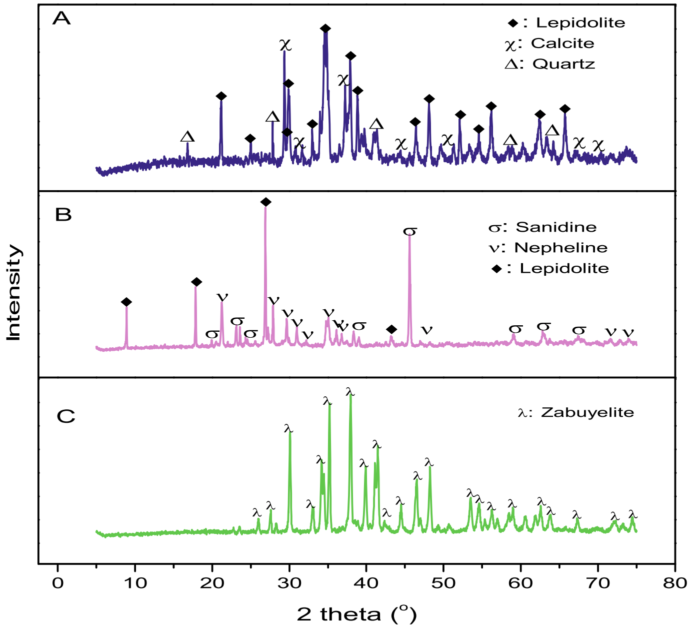

Fig. 5 XRD patterns of the **a** lepidolite + Na_2CO_3 at 500 °C; **b** lepidolite + Na_2CO_3 at 750 °C; C: leached product

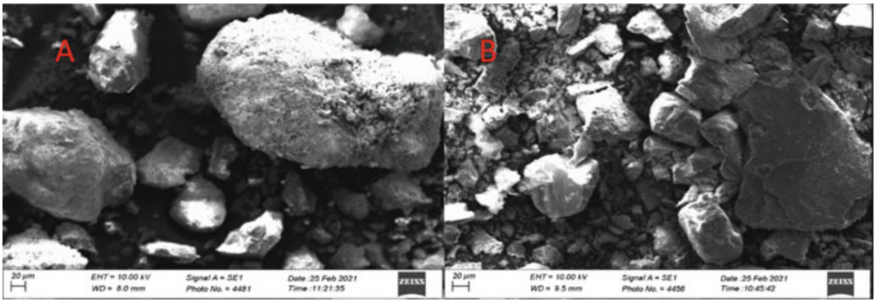

Fig. 6 SEM image **a** initial sample +Na_2CO_3, **b** calcined mixture after processing

Conclusion

In conclusion, the possibility of treating a Nigeria-sourced lepidolite ore by carbonate roasting and subsequent water leaching process was studied. The main components of the lepidolite ore were lepidolite, albite, and quartz. At optimal roast-leaching conditions of lepidolite: Na_2CO_3 molar ratio of 1:3, roasting temperature and time of 750 °C and 60 min, respectively, and leaching temperature and time of 75 °C and

120 min, respectively, 91.2% lithium extraction efficiency was established. Evaporation of the filtrate obtained gave zabuyelite of 99.1% purity, which could serve as a precursor in lithium-ion batteries.

References

1. Sedlakova-Kadukova J, Marcincakova R, Luptakova A, Vojtko M, Fujda M, Pristas P (2020) Comparison of three different bioleaching systems for Li recovery from lepidolite. Sci Rep 10:14594. https://doi.org/10.1038/s41598-020-71596-5
2. Goonan T (2012) Lithium use in batteries—US geological survey circular 1371. US geological survey circular, vol 1371. http://pubs.usgs.gov/circ/1371/
3. Tomascak P, Tomáš M, Ralf D (2016) Advances in Lithium Isotope geochemistry. Springer. https://doi.org/10.1007/978-3-319-01430-2
4. Ziemann S, Weil M, Schebek L (2012) Tracing the fate of lithium—the development of a material flow model. Res Conserv Recy 63:26–34
5. Nogueira CA, Margarido F, Vieceli1 N, Durão F, Guimarães C (2014) Comparison of processes for lithium recovery from lepidolite by H_2SO_4 Digestion or HCl Leaching. In: Proceedings of the international conference on mining, material and metallurgical engineering Prague, Czech Republic, Paper No 72, 1–4
6. Meshram P, Pandey BD, Mankhand TR (2014) Extraction of lithium from primary and secondary sources by pre-treatment, leaching and separation: a comprehensive review. Hydrometallurgy 150:192–208
7. Choubey PK, Kim M, Srivastava RR, Lee J, Lee J (2016) Advance review on the exploitation of the prominent energy-storage element: Lithium. Part I: From mineral and brine resources. Miner Eng 89:119–137
8. Gao L, Wang H, Li J, Wang M (2020) Recovery of Lithium from Lepidolite by Sulfuric Acid and Separation of Al/Li by Nanofiltration. Minerals 10(0981):1–17. https://doi.org/10.3390/min10110981
9. Barbosa LI, Gonzalez JA, Ruiz MD (2015) Extraction of lithium from beta-spodumene using chlorination roasting with calcium chloride. Thermochim Acta 605:63–67
10. Guo H, Kuang G, Wang H, Yu H, Zhao X (2017) Investigation of enhanced leaching of Lithium from α-Spodumene using Hydrofluoric and Sulfuric Acid. Minerals 7:205
11. Luong VT, Kang DJ, An JW, Dao DA, Kim MJ, Tran T (2014) Iron sulphate roasting for extraction of lithium from lepidolite. Hydrometallurgy 141:8–16
12. Yan Q, Li X, Wang Z, Wu X, Guo H, Hu Q, Peng W, Wang J (2012) Extraction of valuable metals from lepidolite. Hydrometallurgy 117–118:116–118
13. Yan Q, Li X, Yin Z, Wang Z, Guo H, Peng W, Hu Q (2012) A novel process for extracting lithium from lepidolite. Hydrometallurgy 121–124:54–59
14. Yan QX, Li XH, Wang ZX, Wang JX, Guo HJ, Hu QY, Peng WJ, Wu XF (2012) Extraction of lithium from lepidolite using chlorination roasting–water leaching process. Trans Nonferr Metals Soc China 22:1753–1759
15. Luong VT, Dong JK, An JW, Kim MJ, Tran T (2013) Factors affecting the extraction of lithium from lepidolite. Hydrometallurgy 134–135:54–61
16. Kong X, Ye H, Qin Y (2014) Factors of extracting lithium from lepidolite by sulfate roasting and dilute sulphuric acid leaching. Appl Mech Mater 522–524:1467–1470
17. Kuang G, Liua Y, Lia H, Xinga S, Lia F, Guo H (2018) Extraction of lithium from β-spodumene using sodium sulfate solution. Hydrometallurgy 177:49–56
18. Olaoluwa DT (2021) Hydrometallurgical processing of Nigerian montebrasite and lepidolite ores as battery and drug delivery agents. PhD Seminar Report, Department of Industrial Chemistry, University of Ilorin, Unpublished

19. Baba AA, Olaoluwa DT, Alabi AGF, Balogun AF, Ibrahim AS, Sanni RO, Bale RB (2018) Dissolution behaviour of a beryl ore for optimal industrial beryllium compound production. Can Metall Q 57(2):210–218. https://doi.org/10.1080/00084433.2017.1403107

Review on Hydrotalcite-Derived Material from Waste Metal Dust, a Solid Adsorbent for CO_2 Capture: Challenges and Opportunities in South African Coal-Fired Thermal Plant

Daniel Ogochukwu Okanigbe, Abimbola Patricia Popoola, Olawale Moshood Popoola, and Prudence Mamasia Moshokwa

Abstract The main contributor to global warming is carbon dioxide (CO_2), herewith referred to as a greenhouse gas, with a growth of nearly 2.7%, 60% above that recorded around late twentieth century. Globally, the regulation and minimization of CO_2 have consequently become a consensus. In South Africa (SA), most CO_2 releases are from burning coal and future forecasts show that CO_2 releases will increase more and more should there be no counter-progress in the creation of carbon capture technologies (CCT). Additionally, by integrating CCT into the main sources of anthropogenic CO_2 releases, like coal power plants (CPPs), challenges of CO_2 releases will be brought to the barest minimal. Despite the challenge it presents, yet an inherent research opportunity therein, with possibility of developing a novel CCT. Hence, this paper presented a review on the theme "hydrotalcite-derived material from waste metal dust, a solid adsorbent for CO_2 capture: Challenges and opportunities in SA's CPPs". This theme was subdivided into the following sub-themes: challenges and opportunities inherent in SA's CPPs; review of past and current publications on CO_2 capture from CPP. The conclusions reached are that the use of waste metal dust and/or coal fly ash to produce solid adsorbents will go a long way to saving significant cost of managing CO_2 emissions, while the conversion of this waste to product amongst other benefits will strengthen the goal of achieving a circular economy in the mining industry.

Keywords CO_2 emissions · Coal-fired thermal plant · Greenhouse gases · Global warming · Carbon capture technologies · Circular economy · Waste metal dust · Solid adsorbent

---

D. O. Okanigbe (✉) · A. P. Popoola · P. M. Moshokwa
Faculty of Engineering and the Built Environment, Department of Chemical Metallurgical and Materials Engineering, Tshwane University of Technology, Pretoria 0183, Republic of South Africa
e-mail: okanigbedo@tut.ac.za

O. M. Popoola
Centre for Energy and Electrical Power, Department of Electrical and Electronics, Tshwane University of Technology, Pretoria 0183, Republic of South Africa

F. Tesfaye et al. (eds.), *REWAS 2022: Energy Technologies and CO_2 Management (Volume II)*, The Minerals, Metals & Materials Series,
https://doi.org/10.1007/978-3-030-92559-8_9

Introduction

South Africa (SA) may not have 250 years [1] of coal reserves, nonetheless, SA is endowed with significant amount of coal to discover for export and domestic use. Premised on the availability of significant coal reserves, 95% of SA's electricity supply comes from non-renewable energy sources, of which coal-fired power plants (CPP) top the list [2]. There are currently 18 operating CPPs in SA (see Fig. 1) differing in producing ability. Twelve CPPs are situated in the Mpumalanga Province (MP), two CPPs are situated in the Limpopo Province, while the remaining four CPPs are situated in the Gauteng Province (GP). These CPPs are located in the highveld of SA. The highveld is known for its various human activities, which include power generation, coal dumps, transportation, petrochemical operations, agriculture, and metallurgical and mining operations [3, 4].

Based on the data obtained from Fig. 1, it can be deduced that SA is a fast-evolving country with an energy budget that is highly reliant on coal. Consequent upon this, according to a 2021 report by Kuang [5] and SA's environment department, which estimated that in 2017, SA emitted 556-million metric tonnes of greenhouse gases (GHG). The breakdown of this GHG showed that 84.75% was from CO_2, 9.28% from methane (CH_4), 4.81% from N_2O, and 1.16% from fluorinated gasses (i.e. hydrofluorocarbons (HCF_3), perfluorocarbons ($CHCl_2F$), sulfur hexafluoride (SF_6), and nitrogen trifluoride (NF_3). The sources of these four GHG (CO_2, CH_4, N_2O), and (HCF_3, $CHCl_2F$, SF_6, and NF_3) can be divided into five categories of economic sectors (Fig. 2).

Table 1 illustrates the countries that are accountable for the emission of CO_2 in a ranking series. According to Kuang [5], SA ranks amongst the 8 countries categorized as developing countries. Based on author's concept (Kuang [5]), developing countries account for 14.2 GT CO_2 emission, roughly 49.7% of the gross CO_2 emission for the 20 countries accounted for in Table 1, most of which (CO_2 emissions) come from the combustion of fossil fuel like coal in the CPPs [6].

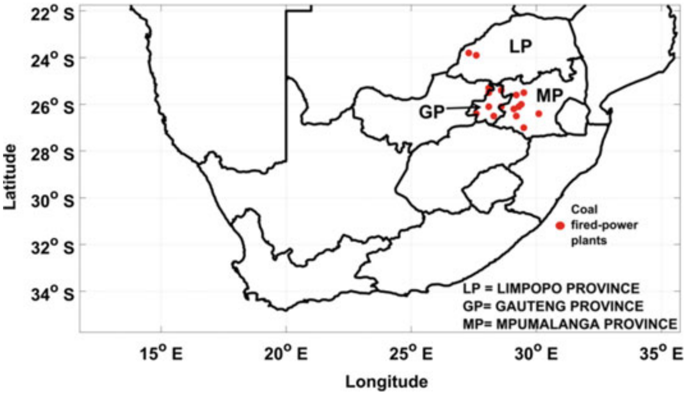

Fig. 1 Sites of CPPs in South Africa [7]

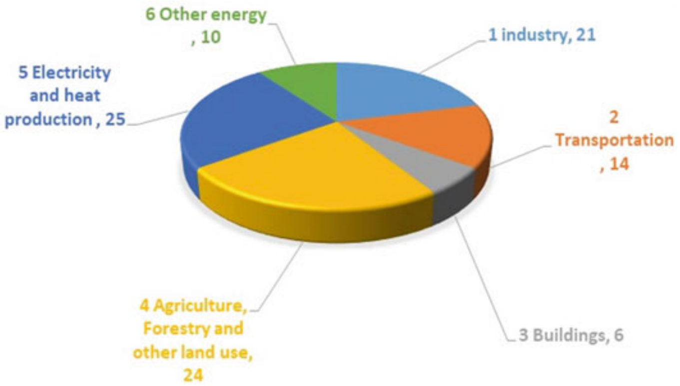

Fig. 2 Pie chart showing global GHG emissions according to economic sectors (adapted from Kuang [5])

Table 1 The 20 countries that emitted the most CO_2 in 2017 [5]

Rank	Country	CO_2 emissions (Total)	Rank	Country	CO_2 emissions (Total)
1	China	9.3 GT	11	Indonesia	0.5 GT
2	United states	4.8 GT	12	Mexico	0.4 GT
3	India	2.2 GT	13	Brazil	0.4 GT
4	Russian Federation	1.5 GT	14	South Africa	0.4 GT
5	Japan	1.1 GT	15	Australia	0.4 GT
6	Germany	0.7 GT	16	United Kingdom	0.4 GT
7	South Korea	0.6 GT	17	Turkey	0.4 GT
8	Islamic Republic of Iran	0.6 GT	18	Italy	0.3 GT
9	Canada	0.5 GT	19	Poland	0.3 GT
10	Saudi Arabia	0.5 GT	20	France	0.3 GT

In the most recent past, SA has been making efforts towards decreasing its carbon footprint by moving its focus to key sources of CO_2 emissions, such as the country's CPPs. More so, it has included carbon capture technologies (CCT) policies into its legislation and has mandated SA's Center for Carbon Capture and Storage (SACCCS) to oversee its implementation. This clearly brings to light that there is a huge potential of implementing CCT in the country's CPPs. So much so that the pressing challenges related to CO_2 emissions require research for clean and sustainable energy technologies, such as carbon capture and storage (CCS) in SA. However, according to Beck, Surridge, and Hietkamp [8], SA will require a portfolio of technologies to meet its climate change. Within this portfolio, carbon capture is amongst the important technology to mitigate CO_2 emissions from CPPs. Since 2009, SACCCS has been investigating the technical feasibility of CCT in SA. SA's CCS guideline, which was endorsed by the cabinet of SA on 4 May 2012, provides the overarching direction for the work of SACCCS. The key milestones of the SA's CCS guideline are as follows:

2004	Assessment of the potential for CCS in SA.
2010	Improvement of SA's CO_2 geological storage atlas.
2017	Inauguration of a CO_2 Test Injection Project (10,000−50,000tCO_2 stored).
2020	Enable start of a CCS demonstration plant (in the order of 100,000tCO_2/year).

2025^+ Update the operation of commercial CCS deployment (over 1,000,000tCO_2/year).

Hence, this paper will present a review on hydrotalcites-derived material from waste metal dust as a potential solid sorbent for CO_2 capture: challenges and opportunities in SA's CPPs.

Challenges and Opportunities Inherent in SA's CPPs

Challenges

In the most recent times, support has continually been given by way of encouraging the use of renewable sources to generate power. This is done with the intention of progressively countering the environmental impact posed through the use of coal to generate power. Energy from renewable sources made up 25% of the global energy combination in year 2017 [9], and their application to generate power is gathering momentum globally at a significant pace. Despite the consequential drop in global use of coal as an energy source, it remains the leading source of energy in the energy mixture in SA. In addition to the merits of CPPs in producing electricity, there are associated environmental impact with the operation, with particular mention of global warming, a consequence of releasing GHG into the atmosphere, the consequence of global warming [10]. Coal cycle (CC) makes up part of the cycles in electricity generation from CPPs [11], with capacity for substantial environmental threats. However, research into the environmental impacts as a result of CC, particularly in countries like SA endowed with coal deposits, is significantly minimal.

Opportunities

Several studies have attempted to evaluate environmental effects of CPPs and its associated processes with emphasis on GHG releases [12]. As a way of correcting these effects, several technologies, like the flue gas desulphurization (FGD), CCT, and selective catalytic reduction (SCR), have been appraised with the goal of determining how conceivable it is for them to reduce environmental pollution. Going by the complete life cycle modelling and comparative assessment of current clean power generation technologies in China that was investigated by Liang et al. [13], in which energy and environmental impact assessment with economic implications of electricity generation employing CPP in advance of final consumption was evaluated in the mining industry amongst others, the deductions made was that CCT has the capacity of bringing CO_2 releases from CPP to the barest minimal, notwithstanding the amount of CO_2 produced (significantly high) during operation of these technologies, a consequence of added energy consumption.

Hence, this literature review will strive to determine where the gap of knowledge is with respect to this area of study and through this knowledge establish a research focus that will aim to proffer a cost-effective and energy-efficient approach to CO_2 capture in SA. To achieve this objective, this literature review will be carried out under the following sub-sections:

1. Review of publications on technological routes for CO_2 capture.
2. Review of publications on different types of sorbents prepared and characterized from fly ash
3. Review of publications on other feedstocks for preparation and characterization of hydrotalcite-derived material.

Review of Past and Current Publications on CO_2 Capture from CPP

Review of Publications on Technological Routes for CO_2 Capture

Absorption Technology

The absorption technology (AT) requires use of solvents to capture CO_2, a practice that has been well researched [14–17], making it a robust, mature, and widely employed industrial technique for CO_2 capture. Despite its reputation for CO_2 capture, the use of chemical solvents (CS) makes it corrosive and the necessity to regenerate expensive CS often used makes it energy demanding. Hence, the use of liquid absorbents is not very suitable for adoption in the SA's CPPs.

Membrane Separation Technology

The membrane separation technology (MST) has potential of being used as a conventional membrane separation unit [18–20]. However, it requires further research to bring its high energy demand during separation to the barest minimal. Apart from its high energy demand, it also has challenge of poor selectivity [1, 21–23]. These setbacks present major disadvantages for CO_2 capture. Hence, the use of MST for post-combustion CO_2 capture is not suitable for implementation in SA's CPPs, because of high cost and difficulty of achieving high degree of CO_2 separation (i.e. high purity CO_2).

Cryogenic Separation Technology

The cryogenic separation technology (CST) for CO_2 capture is mainly based on the principle of condensation and cooling [24, 25]. It is mostly applied in CO_2 capture systems where the gas streams contain a high concentration of CO_2. Nevertheless, the challenge with using MST to capture CO_2 from CPPs is the high level of dilute CO_2 stream [25–28]. It is also an energy-intensive CCT, requiring high amounts of energy for CO_2 separation. Since the concentration of CO_2 from SA's CPPs is quite low, CST will be an inappropriate CCT to use in SA's CPPs.

Adsorption Technology

The adsorption technology (ADT) is a CCT that has been extensively used in chemical and environmental processes [29–31]. Amongst the adsorbents used in this CCT are zeolites, activated carbon, polyaspartamide, metal oxides; porous silicates, metal organic frameworks, and chitosan [7, 32–36]. Despite the low investment cost advantage inherent with using ADT to capture CO_2 [37, 38], ADT is limited by poor heat transfer, especially in packed beds and slow kinetics. Haven't said that, it is also important to state that the advantage of using ADT to capture CO_2 far out-weighs its disadvantages [39]. So, therefore, the use of ADT in SA's CPPs is encouraged, based on ease of regeneration of the adsorbent together with reduced energy requirements.

Review of Publications on Different Types of Sorbents Prepared and Characterized from Fly Ash

Potassium-Based Sorbents

In the work of Sanna and Maroto-Valer [40], the authors investigated the potential of potassium-fly ash (K-FA) sorbents for high-temperature CO_2 sorption. Based on their research findings, authors reported that increased uptake of CO_2 and faster reaction rates in the presence of K-FA can be ascribed to the formation of K-Li eutectic phase, which favours diffusion of potassium and CO_2 in material matrix. Cyclic experimental results show that K-FA materials sustained stable CO_2 uptake and reaction rates of over 10 cycles.

Activated Carbon

In words of Alhamed et al. [41], “power and desalination plants are one of the main anthropogenic sources for CO_2 generation, consequently GHG emitters and thus major contributors to global warming”. In their work fly ash (FA) generated in desalination and power plants were converted into activated carbon (AC) treated with KOH at higher temperature and tested for CO_2 capturing efficiency. The authors discovered that surface area of 161 m^2g^{-1} and adsorption capacity of 26 mg CO_2/g AC can be obtained by activation at KOH/FA ratio of 5 at 700 °C and activation time of 2 h. They therefore concluded that there is great potential in using AC from FA to reduce global warming.

Sodium Silicate Sorbents

According to Sanna and Maroto-Valer [42], Na silicates are good sorbent at ambient temperature, nevertheless the understanding of their potential as high-temperature CO_2 sorbent remains an area yet to be investigated thoroughly. Based on the results from their study authors suggested that carbonate-to-silica ratio used in production of sorbents significantly affects CO_2 sorption capacity and regeneration temperature. Authors also shared that calcination at 800 °C was preferred due to the formation of metastable sodium silicate phases, which resulted in higher CO_2 uptake. Among the developed sorbents, sodium silicate (Na)-to-fly ash ratio (FA) of 0.5:1 was preferred because it maintained CO_2 sorption/desorption capacity after five cycles (compared to 1:1 and 1.5:1). Additionally, NA-to-FA ratio of 0.5:1 presented good capacity at post-combustion conditions (12.5% CO_2, 12% H_2O, 700 °C). The presence of 20% Li_2CO_3 additive enhanced the CO_2 sorption of 20%. Generally, the Na to FA ratio of 0.5:1 sorbent showed a CO_2 capture capacity and recyclability comparable to those of other high-temperature sorbents.

Mesoporous Silica Materials

In the work by Panek et al. [43], the authors synthesized mesoporous silicate molecular sieve, MCM-41, from pulverized coal fly ash (PFA), using silicate filtrate which is a by-product hydrothermal zeolite production. In this study, rice husk ash was also used for comparison but fusion with sodium hydroxide was used to prepare the silicate filtrate, along similar lines to earlier reports of using PFA as a precursor for MCM-41 synthesis. After polyethyleneimine (PEI) impregnation for CO_2 capture, the ash-derived MCM-41 samples displayed higher uptakes than the commercial sample with the maximum achievable PEI loading of 60 Wt% PEI (dry basis) before particle agglomeration occurs, approximately 13 compared to 11 Wt%, respectively, the latter being comparable to earlier reports in the literature. The PFA sample that displays the fastest kinetics to achieve 90% of the equilibrium uptake had the largest mesopore volume of 1.13 cm^3 g^{-1}. Given that PFA-derived MCM-41 uses a waste silicate solution for hydrothermal preparation and no prior preparation is needed, production costs are estimated to be considerably lower where silicate solutions need to be prepared by base treatment, even if ash is used, as for the RHA-derived MCM-41 used here.

CO_2 Aluminosilicate Sorbents

Zeolites

In the works of Liu et al. [44], the authors prepared Zeolite A and A + X mixtures from coal fly ash procured from China by using an alkali fusion method. Authors shared that when comparison exercise was carried on both zeolites with 13X zeolites at higher temperature (~90 °C), both the zeolite A + X mixture and zeolite A prepared from fly ash showed better performance in CO_2 capture from flue gas because they have higher selectivity of CO_2 over N_2.

Hydrotalcites (HT)

As mentioned by Muriithi et al. [45], authors reported that synthesis of hydrotalcites (HT) from mineral waste (e.g. blast furnace slag) continues to receive increasing attention. In their study, a novel approach for preparing HT from SA's coal combustion fly ash (FA) was reported. According to findings from this investigation, authors shared that structural characteristics of HT produced from FA were similar to those of HT produced from analytical-grade chemicals, except for the presence of calcite. Authors therefore concluded by sharing that there is a potential in producing high-quality HT under the optimized process conditions for CO_2 capture.

Review of Publications on Other Feedstocks for Preparation and Characterization of Hydrotalcite-Derived Material

Oil Shale Ash

Galindo et al. [46] reported that hydrotalcite-like compounds were co-precipitated with diluted sodium hydroxide from an unconventional aluminium source: the aluminium waste generated by the tertiary aluminium industry, with the assistance of ammonia and triethanolamine at pH 10. These products were characterized by several techniques (XRD, FT-IR, UV–vis–NIR, SEM, DTA-TG, and BET methods) to compare results. The characterisation of products confirmed significant differences depending on basic reagent selected. Products co-precipitated with ammonia showed less crystal growth, a more significant iron content in the structure and higher internal surface area. Products from triethanolamine showed the entry of organic molecules into the layered structure. These findings were important for the improvement of methods based on waste treatment, transforming an aluminium hazardous waste into a value-added product as layered double hydroxides.

Coal Fly Ash

According to Muriithi et al. [44], very little information is available on the natural carbon capture potential of wet or dry ash dams. Hence their study focused on investigating the extent of carbon capture in a wet-dumped ash dam and the mineralogical changes that promote CO_2 capture, comparing this natural phenomenon with accelerated ex situ mineral carbonation of fresh fly ash (FA). Outcome shows that up to 6.5 wt% CO_2 was captured by the fresh FA with a 60% conversion of calcium to $CaCO_3$ via accelerated carbonation (carried out at 2 h, 4 Mpa, 90 °C, bulk ash, and a S/L ratio of 1). On the other hand, 6.8 wt% CO_2 was found to have been captured by natural carbonation over a period of 20 years of wet disposed ash. It was concluded that natural carbonation in the ash dumps is significant and may be effective in capturing CO_2.

Mullite-Rich Tailings From Density Separated Copper Smelter Dust

In the study conducted and reported by Linda et al. [47], the authors agreed that the high cost of metal powders like mullite prohibits use for certain engineering applications. Hence, authors recommended harnessing mullite from a secondary copper resource as an approach of countering the high cost of synthesized mullite. In line with this school of thought, and the outcome of a characterization exercise of the gravity separation of the copper smelter dust using the Knelson concentrator, authors reported that recovery of SiO_2 in concentrate was 33.04% and in Tailings (MRT) it was 67.66%, while recovery of Al_2O_3 into concentrate was 32.82% and into tailings it was 67.15%. Further characterization of the MRT revealed 80% of particles were below 75 μm, while SEM–EDS confirmed XRD patterns of quartz and aluminosilicate minerals (i.e. epidote, plagioclase, chlorite, and muscovite) as shown in Fig. 3. It was therefore recommended by authors based on enormity, potential, and possibility of MRT that it should be used to reduce the cost of mullite refined powders in subsequent engineering applications.

Conclusions

Researchers agree that the potential for CO_2 capture rest in the hands of key emitting sources, like the CPPs. Researchers also agree that most suitable CO_2 capture route

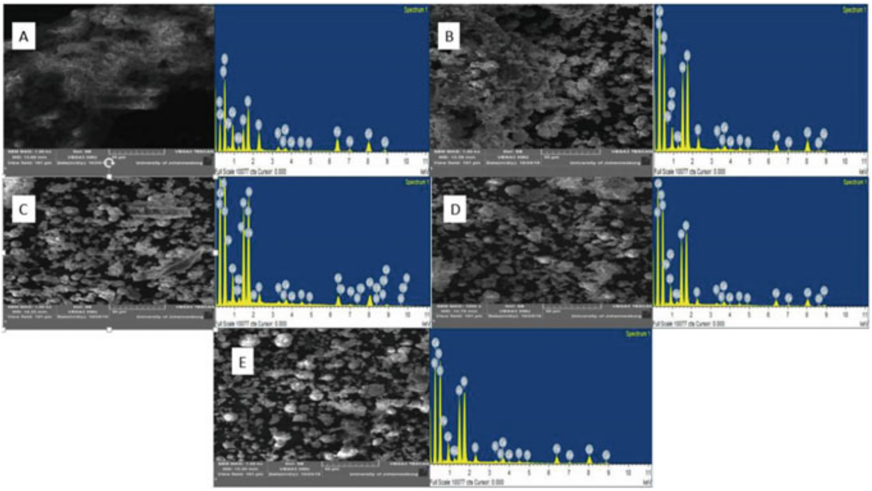

Fig. 3 SEM and EDS images of **a** 150 µm particles, **b** 106 µm particles, **c** 75 µm particles, **d** 53 µm particles, and **e**-53 µm/Pan particles [47]

for the SA's CPPs is post-combustion CO_2 capture. According to the reports from researchers, the suitability is premised on ease of retrofitting of capture devices in the existing CPPs. In line with this claim authors also agree that adsorption technology (ADT) using solid adsorbents will be ideal and more economically viable for CO_2 capture in the SA's CPPs. Based on reports on research that have been conducted on the ADT using solid adsorbents, hydrotalcites has been reported as a solid adsorbent with good promise for CO_2 capture even at the industrial scale. However, authors also agree that despite the ease of synthesizing HT in the laboratory using analytical-grade chemicals, which eliminate difficulties associated with multiple anions in the structural matrix, while allowing for trends and characteristics to be more readily determined, the use of pure chemicals increases their production costs. Authors agree that high cost of production of HT can be brought to the barest minimal by producing HT from alternative sources of starting materials. The authors agreed that alternative raw materials for production of HTs can be CFA and/or WMD. Authors also agreed that application of a waste material such as (CFA) and/or waste metal dust (WMD) to fabricate CO_2 adsorbents such HTs has its advantages. Hence a gap of knowledge has been identified in the area of using the SA's CFA and/or MRT for the synthesis of HTs. It is therefore recommended that future research should focus on preparation and characterization of HT-derived material from CFA and/or WMD for CO_2 capture from SA's CPPs.

Acknowledgements The authors wish to thank Tshwane University of Technology, Pretoria, South Africa for the support given during the preparation of this manuscript.

References

1. Kumar N, Mukherjee S, Harvey-Reid NC, Bezrukov AA, Tan K, Martins V, Vandichel M, Pham T, van Wyk LM, Oyekan K, Kuma A (2021) Breaking the trade-off between selectivity and adsorption capacity for gas separation. Chem 7(11):3085–3098
2. Thopil GA, Pouris A (2015) Aggregation and internalization of electricity externalities in South Africa. Energy 82:501–511
3. Dabrowski JM, Ashton PJ, Murray K, Leaner JJ, Mason RP (2008) Anthropogenic mercury emissions in South Africa: coal combustion in power plants. Atmos Environ 42(27):6620–6626
4. Freiman MT, Piketh SJ (2003) Air transport into and out of the industrial Highveld region of South Africa. J Appl Meteorol Climatol 42(7):994–1002
5. Kuang C (2021) Analysis of green house gases and positive impact of replacing traditional energy with clean energy. In: E3S Web of Conferences, vol 241. EDP Sciences, p 02005
6. AR5 Synthesis Report: Climate Change 2014 (n.d.). Accessed 10 Nov 2020. www.ipcc.ch/report/ar5/syr/
7. Shikwambana L, Mhangara P, Mbatha N (2020) Trend analysis and first time observations of sulphur dioxide and nitrogen dioxide in South Africa using TROPOMI/Sentinel-5 P data. Int J Appl Earth Observ Geoinf 91:102130
8. Beck B, Surridge T, Hietkamp S (2013) The South African centre for carbon capture and storage delivering CCS in the developing world. Energy Procedia 37:6502–6507
9. International Organization for Standardization (2006) Environmental management: life cycle assessment; principles and framework, vol 14044. ISO
10. Mbohwa C (2013) Life cycle assessment of a coal-fired old thermal power plant. Proc World Cong Eng 1:2078–958
11. Rathnayake M, Julnipitawong P, Tangtermsirikul S, Toochinda P (2018) Utilization of coal fly ash and bottom ash as solid sorbents for sulfur dioxide reduction from coal fired power plant: Life cycle assessment and applications. J Clean Prod 202:934–945
12. Mittal ML, Sharma C, Singh R (2012) August. Estimates of emissions from coal fired thermal power plants in India. In: 2012 International emission inventory conference pp 13–16
13. Liang X, Wang Z, Zhou Z, Huang Z, Zhou J, Cen K (2013) Up-to-date life cycle assessment and comparison study of clean coal power generation technologies in China. J Clean Prod 39:24–31
14. Liu Y, Dai Z, Zhang Z, Zeng S, Li F, Zhang X, Nie Y, Zhang L, Zhang S, Ji X (2021) Ionic liquids/deep eutectic solvents for CO_2 capture: reviewing and evaluating. Green Energy Environ 6(3):314–328
15. Ochedi FO, Yu J, Yu H, Liu Y, Hussain A (2020) Carbon dioxide capture using liquid absorption methods: a review. Environ Chem Lett 1–33
16. Shavalieva G, Kazepidis P, Papadopoulos AI, Seferlis P, Papadokonstantakis S (2021) Environmental, health and safety assessment of post-combustion CO_2 capture processes with phase-change solvents. Sustainable Prod Consumpt 25:60–76
17. Wang J, Liu L, Zeng X, Li K (2021) Solar-assisted CO_2 capture with amine and ammonia-based chemical absorption: a comparative study. Thermal Sci 25(1 Part B):717–732
18. Ahmad MZ, Fuoco A, (2021) Porous liquids–future for CO_2 capture and separation. Current Res Green Sustainable Chem 4:100070
19. Cannone SF, Lanzini A, A review on CO_2 capture technologies with focus on CO_2-enhanced methane recovery from hydrates. Energies 14(2):387
20. Janakiram S, Santinelli F, Costi R, Lindbråthen A, Nardelli GM, Milkowski K, Ansaloni L, Deng L (2021) Field trial of hollow fiber modules of hybrid facilitated transport membranes for flue gas CO_2 capture in cement industry. Chemi Eng J 413:127405
21. Kratky L, Kolacny J, Sulc R (2021) Experimental study on CO_2 membrane separation from slue gas. Chem Eng Trans 86:1075–1080
22. Wang Y, Lu J, Qi J, Lang X, Fan S, Yu C, Li G (2021) High selectivity CO_2 capture from biogas by hydration separation based on the kinetic difference in the presence of 1, 1-Dichloro-1-fluoroethane. Energy Fuels 35:10689–10702

23. Zunita M, Hastuti R, Alamsyah A, Khoiruddin K, Wenten IG (2021) Ionic liquid membrane for carbon capture and separation. Sep Purif Rev. https://doi.org/10.1080/15422119.2021.1920428
24. Koohestanian E, Shahraki F (2021) Review on principles, recent progress, and future challenges for oxy-fuel combustion CO_2 capture using compression and purification unit. J Environ Chem Eng 9(4):105777
25. Sun R, Tian H, Song C, Deng S, Shi L, Kang K, Shu G (2021) Performance analysis and comparison of cryogenic CO_2 capture system. Int J Green Energy 18(8):822–833
26. Kim S, Lim YI, Lee D, Seo MW, Mun TY, Lee JG (2021) Effects of flue gas recirculation on energy, exergy, environment, and economics in oxy-coal circulating fluidized-bed power plants with CO_2 capture. Int J Energy Res 45(4):5852–5865
27. Mosaffa AH, Farshi LG (2020) Novel post combustion CO_2 capture in the coal-fired power plant employing a transcritical CO_2 power generation and low temperature steam upgraded by an absorption heat transformer. Energy Convers Manag 207:112542
28. Muroyama AP, Beard A, Pribyl-Kranewitter B, Gubler L (2021) Separation of CO_2 fromdilute gas streams using a membrane electrochemical cell. ACS ES&T Eng
29. Cloete S, Giuffrida A, Romano MC, Zaabout A (2020) Economic assessment of the swing adsorption reactor cluster for CO_2 capture from cement production. J Clean Prod 275:123024
30. Dissanayake PD, Choi SW, Igalavithana AD, Yang X, Tsang DC, Wang CH, Kua HW, Lee KB, Ok YS (2020) Sustainable gasification biochar as a high efficiency adsorbent for CO_2 capture: a facile method to designer biochar fabrication. Renew Sustain Energy Rev 124:109785
31. Subraveti SG, Roussanaly S, Anantharaman R, Riboldi L, Rajendran A (2021) Techno economic assessment of optimised vacuumswing adsorption for post-combustion CO_2 capture from steam-methane reformer flue gas. Sep Purif Technol 256:117832
32. Aziz MA, Kassim KA, BakarWAWA, Jakarmi FM, Ahsan AA, Rosid SJM, Toemen S (2019) Traffic pollution: perspective overview toward carbon dioxide capture and separation method. In: Fossil free fuels. CRC Press, pp 149–186
33. Comfort SM (2017) Synthesis and evaluation of SOD-ZMOF-chitosan adsorbent for post combustion carbon dioxide capture. Doctoral dissertation, Faculty of Engineering and the Built Environment, University of the Witwatersrand, Johannesburg
34. Kamran U, Park SJ (2021) Chemically modified carbonaceous adsorbents for enhanced CO_2 capture: a review. J Clean Prod 290:125776
35. Mazari SA, Ali E, Abro R, Khan FSA, Ahmed I, Ahmed M, Nizamuddin S, Siddiqui TH, Hossain N, Mubarak NM, Shah A (2021) Nanomaterials: applications, waste-handling, environmental toxicities, and future challenges-a review. J Environ Chem Eng 9(2):105028
36. Nazarzadeh Zare E, Mudhoo A, Ali Khan M, Otero M, Bundhoo ZMA, Patel M, Srivastava A, Navarathna C, Mlsna T, Mohan D, Pittman CU Jr (2021) Smart adsorbents for aquatic environmental remediation. Small 17(34):2007840
37. Nie L, Mu Y, Jin J, Chen J, Mi J (2018) Recent developments and consideration issues in solid adsorbents for CO_2 capture from flue gas. Chin J Chem Eng 26(11):2303–2317
38. Pardakhti M, Jafari T, Tobin Z, Dutta B, Moharreri E, Shemshaki NS, Suib S, Srivastava R (2019) Trends in solid adsorbent materials development for CO_2 capture. ACS Appl Mater Interfaces 11(38):34533–34559
39. Cormos AM, Cormos CC (2017) Reducing the carbon footprint of cement industry by post combustion CO_2 capture: techno-economic and environmental assessment of a CCS project in Romania. Chem Eng Res Des 123:230–239
40. Sanna A, Maroto-Valer MM (2016) Potassium-based sorbents from fly ash for high-temperature CO_2 capture. Environ Sci Pollut Res 23(22):22242–22252
41. Alhamed YA, Rather SU, El-Shazly AH, Zaman SF, Daous MA, Al-Zahrani AA (2015) Preparation of activated carbon from fly ash and its application for CO_2 capture. Korean J Chem Eng 32(4):723–730
42. Sanna A, Maroto-Valer MM (2016) CO_2 capture at high temperature using fly ash-derived sodium silicates. Ind Eng Chem Res 55(14):4080–4088

43. Panek R, Wdowin M, Franus W, Czarna D, Stevens LA, Deng H, Liu J, Sun C, Liu H, Snape CE (2017) Fly ash-derived MCM-41 as a low-cost silica support for polyethyleneimine in post-combustion CO_2 capture. J CO_2 Utili 22:81–90
44. Liu L, Singh R, Xiao P, Webley PA, Zhai Y (2011) Zeolite synthesis from waste fly ash and its application in CO_2 capture from flue gas streams. Adsorption 17(5):795–800
45. Muriithi GN, Petrik LF, Doucet FJ (2020) Synthesis, characterisation and CO_2 adsorption potential of NaA and NaX zeolites and hydrotalcite obtained from the same coal fly ash. J CO_2 Util 36:220–230
46. Galindo R, López-Delgado A, Padilla I, Yates M (2015) Synthesis and characterisation of hydrotalcites produced by an aluminium hazardous waste: a comparison between the use of ammonia and the use of triethanolamine. Appl Clay Sci 115:115–123
47. Linda PL, Okanigbe DO, Popoola API, Popoola OM (2021) Characterization of density separated mullite rich tailings from a secondary copper resource, a potential reinforcement material for development of an enhanced thermally conductive and wear resistant ti-6al-4v matrix composite. In: The proceedings of the 60th international conference of metallurgist. Canada

Benefits of a Smart Electrical Energy Management Information System and Its Impact in Your CO_2 Footprint

Hector Linares

Abstract The use of “smart” power meters across a distribution network on an industrial facility can generate information for product cost allocation, operational efficiency improvement, reliability metrics (predictive maintenance), and Root Cause Fault Analysis (RCFA) or troubleshooting. To reach all the potential benefits of the network, it needs to be designed with a modern digitalization approach, able to convert electrical power measurement signals into useful business information. This session will explore the different units that a modern power measurement device can register and how they can be extrapolated to become useful business information, for example, power factor and utility bills, demand, curtailment restrictions, Total Harmonic Distortion (THD), and electrical failures. Then, it will discuss the optimal network architecture to optimize the level and amount of information collected the protocols to share that information and the security firewalls to prevent unauthorized access to the devices to close with the implications this may have in your CO_2 footprint.

Keywords Smart meter · Power network · Energy Management Information Systems (EMIS) · Digitalization · CO_2 footprint

Introduction

Current power distribution systems are becoming more complex to a point where power flow assumed to flow in one direction and generated by a single source of energy is becoming outdated. The strain on the power generation grid along with the increase of renewable distributed generation systems requires more advanced power meters on multiple measuring points with the ability to generate real-time dashboards to support operating decisions to optimize the use of energy. The traditional approach of single-point, once-a-month, manual capture readings is no longer effective for modern power distribution systems with upcoming digitalization requirements. New

---

H. Linares (✉)
Carmeuse, Innovation Center, Pittsburgh, PA 15220, USA

F. Tesfaye et al. (eds.), *REWAS 2022: Energy Technologies and CO_2 Management (Volume II)*, The Minerals, Metals & Materials Series,
https://doi.org/10.1007/978-3-030-92559-8_10

power meter networks need to have expanded metering capacity, digitization ability, and networking enabled to be able to evolve from a reporting tool to an Energy Management System foundation.

Smart Power Meters

New technology using solid-state components has expanded the functionality, accuracy, and connectivity of power meters from traditional electromechanical equipment.

Functionality

In addition to the instant power and energy consumption indication from first-generation power meters, current meters have the ability to display, record, and transmit a wide variety of measurements as shown in Table 1.

Other functionality can include the following:

11. Time real-time clock (Year, Month, Date, Hour, Minute, Second);
12. Alarming over/under limit alarming;
13. Data logging on internal memory;
14. I/O option;
15. Display screen;
16. Backup battery to maintain power meter operation during power outages; and
17. Bi-directional communication to perform actions remotely on the electrical system like disconnection, fault reset, and/or operation of a closing device.

Accuracy

Recent studies which were able to track the sources of meter bias or shifting allowed the creation of compensating circuitry for effects from under/overload, temperature, fast frequencies, and core saturation among other phenomena that can affect the electrical reading devices. This relates not only to the accuracy of the readings but also to the ability to capture very fast events related with power quality.

New power meters can be able to comply with standards like ANSI C 12.20; IEC62053-22 who specify different accuracy classes like 0.1% to 0.5%.

Some of the key standards are IEC 61,000–4-30 Class A and Class S, IEC61000-4–7 harmonic measurements, and IEC61000-4–15 for flicker. Industry standards establish a common understanding of power quality in real-world electrical networks and provide users confidence that they will have accurate data to solve problems and issues related to events.

Table 1 Electrical measurements

1. Energy	2. Current Demand
2.1.1. Active Energy Ep	2.1.2. Current Demand Total and each circuit
2.1.3. Reactive Energy Eq	2.1.4. Peak Current Demand Total and each circuit
2.1.5. Apparent Energy Es	Apparent Power Total and each circuit
3. Time Of Use (TOU) 4 Tariffs (sharp, peak, valley, and normal), 14 Schedules (14 segments, weekends, and 10-year holiday settings)	4. Power Factor Total and each circuit
5. Power Demand	6. Frequency F
6.1.1. Active Power Demand Demand_P	6.1.2. Power Quality
6.1.3. Reactive Power Demand Demand_Q	6.1.4 Total Harmonic Distortion THD
6.1.5. Apparent Power Demand Demand_S	6.1.6. Individual Harmonics 2nd ~ 31st (Voltage and Current)
6.1.7. Peak Power Demand Demand_P_max	6.1.8. Current K Factor KF
7. Real-Time Metering	8. Voltage Crest Factor CF
8.1.1. Phase Voltage V1, V2, V3	8.1.2. Voltage Unbalance U_unbl
8.1.3. Line Voltage V12, V23, V31	8.1.4. Current Unbalance I_unbl
9. Current Total and each circuit	10. Voltage and Frequency Sag/Swells log
10.1.1. Power Total and each circuit	10.1.2. Voltage and Frequency Sag/Swells log
10.1.3. Reactive Power Total and each circuit	10.1.4. Voltage and Frequency Sag/Swells log

Connectivity

The previous more common analog measurements of voltage and current that were translated into power and demand can be digitized now using Analog/Digital (A/D) converters and signal microprocessors, once the information is converted into digital data, this can be transferred to big data handling systems, able to log, trend, and store large amounts of information but this needs to be integrated and transmitted via an effective communication network that is capable of delivering accurate and reliable streams of data in a timely manner.

Protocols

There are many protocols currently used for these networks and the definition of the proper protocol to be used depends on many factors like the hardware compatibility, distances, media available, number of ports, bandwidth, operating cost, and service agreements among others. Table 2 shows a list of some of the most used protocols.

Table 2 Network protocols

+ Built-in Standard Modbus-RTU via RS485	+ Dual Ethernet	+ Wi-Fi
+ Modbus-TCP/IP	+ HTTPs Webserver	+ HTTP/HTTPs Post
+ BACnet-IP	+ FTP Post	+ SMTP
+ SNMP	+ SNTP	+ MQTT

Is not uncommon to have networks that use more than one communication protocol and media depending on the hierarchy level (front or backbone), media (radio, fiber optic, Ethernet, etc.), and meter generation (legacy families tend to use serial protocols while new meters come with Wi-Fi, Cellular, or Ethernet configuration).

Architecture

Depending on the number of nodes, bandwidth, distance, and capacity to serve other needs, the network architecture more commonly could be point-to-point mesh configuration, redundant ring, or hierarchical star.

Cybersecurity

Modern power metering networks cannot longer exist as isolated local area networks, in order to process the data and generate business decision guidelines, they need to be connected with process control systems and business wide area networks, this also expose them to cyberattacks, a reliable firewall needs to be incorporated into the network to ensure that only approved users and applications can get access to the information generated by the meters, one of the most effective approach that have worked with large metering networks like the smart grids is a distributed firewall framework [1], with the ability to inspect packets from the different layers and identify security events and critical states, generating real-time event alarms.

The location of the elements of the firewall is critical, most commonly where the borderline between private and public networks is. An efficient configuration process as well as appropriate diagnostic tools are essential elements of an adequate firewall.

Energy Management Information Systems

Recent increasing demands are pushing for an integrated network with the automation, operation, business, and power metering properly segmented, this is the base for modern digitalization strategies, but collecting and storing the information is just the first step of the process.

Conversion

How much impact can have a lower than 80% power factor in the production cost of a company? What is the impact in the expected life of an electrical equipment if the THD is greater than 5%? These and other questions require the conversion of electrical measurements into operational and business implications, a proper analysis on a case-by-case scheme needs to be performed in order to identify the correlation between them. In many cases, with enough historical data and depth process and equipment knowledge, a correlation can be established and this information is very useful to create standard operating procedures, focus capital investments, design automated controls, and set benchmarks. This process enables the next sections of this topic.

Digitalization

It is defined as the use of digital technologies to change a business model and provide new revenue and value-producing opportunities; it is the process of moving to a digital business. A concrete example of this could be a production model adapted to the different tariff levels and schedules in order to minimize the cost of the electrical energy with automated production controls that prioritize the use of electrical power to maintain peak demand to the lowest level.

This requires consolidation of production indicators, business priorities, benchmarks, power measurements, and reliability parameters, the concept of an isolated-dedicated power network is no longer viable to achieve these goals.

There is a formal tool to implement this digitalization strategy using smart power metering networks, this tool is described next.

EMIS

An energy management information system (EMIS) is a performance management system that enables individuals and organizations to plan, make decisions, and take effective actions to manage energy use and costs. This system makes energy performance visible to different levels of the organization by converting energy and utility driver data at energy account centers into energy performance information. It does this by using performance equations that are compared with the organization's energy targets.

Benefits

Here are some examples of how this data can be converted into useful business strategic information.

Product Cost Allocation

With the proper distribution of the power meters and using real-time production rates, the system can calculate electrical energy cost per ton or unit of the different products of a manufacturing line, this supports accurate cost allocation resulting on a better price structure impacting revenues of the company, it can also help to find areas of opportunity in the process when product benchmarks across different producing facilities are not met.

Efficiency

Real-time monitoring of the use of electrical energy can help to identify inefficiencies in the system due to wear, leaks, idle time, sub-optimal rates, re-handling, and bottlenecks, triggering corrective actions focused on the real issue that will bring immediate improvements in the process.

Reliability

Power monitoring can track wear trends on pumps, fans, crushers, compressors, elevators, and other types of equipment, enabling Condition Base Monitoring and Reliability Centered Maintenance systems to make adequate decisions on interventions; proper setting of alarms can help to identify abnormal conditions before they become an extended shutdown.

RCFA

If the worst come to the worst and production is impacted by a shutdown, finding the root cause is key to restore operations and prevent this to happen again, having historical information about the health of the equipment, operating conditions, and external phenomena that can influence the equipment like power quality issues can be a valuable tool to expedite the Root Cause Fault Analysis (RCFA).

CO_2 Footprint

Almost every source of energy used by the industry has implications on its CO_2 footprint. This is a strong incentive to optimize the use of energy across the company but how can you improve what you cannot measure?

Distributed Power Metering Network

With the deployment of smart MCCs, solid-state starters, and variable frequency drives, the electrical current used for each one of these pieces of equipment is more readily available, this is not a complete power measurement but, in many cases, can serve as a very good approximation. Every year there are new instruments available to measure electrical variables, more advanced, more accurate and smarter, making it easier and cheaper to deploy a highly segmented network of power meters, allowing companies to identify major and more variable loads where higher impacts can be achieved to optimize the use of electrical energy.

Energy savings cannot be directly measured since they represent the absence of energy use. Instead, savings are determined by comparing measured use before and after implementation of a project, making appropriate adjustments for changes in conditions. This implies that a distributed power metering network is the first step required to implement and evaluate energy saving projects which are becoming more and more important as the industrial electrical energy cost increases above the inflation rate [2]. The average component cost for similar projects based on 56 study cases of utility companies reflects a 47% cost on the power meter, 21% of cost on the communication network, 17% on the data management, and 15% on other costs [3].

Net Metering

Legislation to improve the adoption of net metering (where power produced in excess by an industrial facility can be sold back to the utility company) [4] creates a larger incentive for companies to invest in energy-recovering projects, biomass, waste-heat recovery, solar, and wind are some examples, traditional electrical energy consumers are evolving to become e-consumers/generators of electricity, being able to monitor on real time the flow of energy, the total power, and its distribution across the project, which requires more advanced metering networks and energy management information systems, under this circumstances, these systems evolve from cost optimization tools to strategic business decision support platforms.

Conclusions

Electrical energy has evolved to become a commodity with the particularities that it cannot be stored, and it is interchangeable regardless of its origin, but when you take in consideration its CO_2 footprint, the source of electricity makes a large difference. Also, energy costs had increased five times faster than total inflation in the US during 2021 [5].

These two facts are encouraging largest users (industry) to find better ways to optimize the use of energy, migrate from traditional sources of energy like coal or oil to renewable electricity or alternative fuels taking advantage of new technologies, and, in some cases, become generators of electricity taking advantage of its own recovered energy sources.

In summary, measuring electrical energy in real time is becoming a critical decision tool. The two main pillars for a reliable, accurate, and advanced system are a modern power metering network and a powerful Energy Management Information System.

There are other sources of energy and utilities used in the industry: fuel, coal, gas, biomass, compressed air, water, etc. All of them can be measured and incorporated to an Energy Management Information System, expanding the applicability of these concepts to make this a comprehensive system, multiplying the identification of areas of opportunity in energy use, and this has a double positive impact for the company, reduction of energy costs, and reduction on the CO_2 footprint simultaneously. For example, every kwh that these projects can reduce will have an impact of up to 1.6 CO_2 pounds, for every Million Cubic Meters (MCM) of natural gas used, 121 pounds of CO_2 is generated, for every gallon of gasoline, 19.6 pounds of CO_2 is generated, and for every pound of coal, 9.8 pounds of CO_2 is generated [6]. If these numbers look small, just multiply them for the actual energy an average company is using. If we all focus on the same goal, optimize the use of energy, the impact we can make into this world in terms of sustainability and CO_2 reduction is going to be significant.

References

1. Radoglou-Grammatikis P, Sarigiannidis P, Liatifis T, Apostolakos T, Oikonomou S (2018) An overview of the firewall systems in the smart grid paradigm. Paper presented at Global Information Infrastructure and Networking Symposium (GIIS 2018), Thessaloniki, Greece
2. eia.gov/electricity/data/browser/#/topic/7?agg=2,0,1&geo=g&freq=M. Accessed 10 Mar 2021
3. US Department of Energy (2016) Advanced metering infrastructure results from the smart grid investment grant program, Sept 2016, pp 26–70
4. US Senate (2009) Net metering hearing before the committee on energy resources, pp 5–7
5. Inflation (CPI) by the OECD. https://data.oecd.org/price/inflation-cpi.htm. Accessed 10 Mar 2021
6. US Energy Information Administration (2021) Electricity data browser, June 2021
7. Accuenergy AcuRev Multi-Circuit Power Meter November (2020) pp 4–5
8. Henriot P, Munuera L, Warichet J (2021) Power system's digital transformation international energy agency, pp 5–10

9. Yi-Hui X, Zhen-Hua L (2016) Analysis of present state of the digital power meter field
10. Calibration Technology MATEC 61, pp 1–4
11. CEATI International (2008) Energy savings measurement guide, pp 5–6
12. Environmental Protection Agency Greenhouse gas equivalencies Calculator (2021). https://www.epa.gov/energy/greenhouse-gas-equivalencies-calculator Accessed 10 Mar 2021

Modes of Operation, Design, and Experiments in a Laboratory Solar Convective Furnace System

Vishwa Deepak Kumar, Laltu Chandra, Piyush Sharma, and Rajiv Shekhar

Abstract The concept of a laboratory-scale solar convective furnace system (SCFS) has been proposed in a previous publication (Patidar et al. in *JOM* 67:2696–2704, 2015). In the present work, hot air generated from concentrated solar radiation heats ingots in an aluminium soaking furnace. The SCFS consists of the following components: an open volumetric air receiver (OVAR) to heat ambient air, thermal energy storage to address the intermittency of solar radiation, and a retrofitted soaking furnace. The TES is charged by hot air from the OVAR. Hot air recovered from the TES heats ingots in the retrofitted furnace. The present paper has three objectives. First, the modes of operation of a SCFS will be explored. Herein, the possible circuits which depict the interconnection between the components of a SCFS for day and night operations will be discussed. Second, the design basis and results of a laboratory-scale SCFS will be shown. Third, a preliminary mathematical model of a SCFS circuit will be presented.

Keywords Solar convective furnace · Thermal energy storage · Open volumetric air receiver

Introduction

To minimize the use of fossil fuels, Patidar et al. [1] have proposed a solar convective furnace system (SCFS). Here, hot air from an open volumetric air receiver (OVAR) is used as the heat source in an aluminium soaking furnace. The OVAR, located at the top of a tower, receives concentrated solar radiation (~ 500 kW.m^{-2}) from a surrounding,

---

V. D. Kumar
Indian Institute of Technology Jodhpur, Jodhpur 342037, RJ, India

L. Chandra
Indian Institute of Technology (BHU) Varanasi, Varanasi 221005, UP, India

P. Sharma · R. Shekhar (✉)
Indian Institute of Technology (ISM) Dhanbad, Dhanbad 826004, JH, India
e-mail: vidtan@iitism.ac.in

F. Tesfaye et al. (eds.), *REWAS 2022: Energy Technologies and CO$_2$ Management (Volume II)*, The Minerals, Metals & Materials Series,
https://doi.org/10.1007/978-3-030-92559-8_11

concentric, heliostat field. An OVAR consists of several metal or ceramic, porous, absorbers. These absorbers are exposed to the concentrated solar radiation, which, in turn, heats the ambient air drawn through the pores of the absorbers. Air temperatures up to 700 °C have been achieved in a 1.5 MWe demonstration plant [1]. Details of OVAR design are given in [2, 3]. To address the intermittency of solar radiation and ensure 24 × 7 operation, the SCFS is also equipped with thermal energy storage (TES). TES is a packed-bed reactor containing high heat capacity solids. The TES is charged by introducing hot air from OVAR during daytime. During the off-sun hours, the TES is discharged using ambient air, and the obtained hot air is used for soaking aluminium ingots.

This study has three objectives. First, the modes of operation of a SCFS will be explored. Herein, the possible circuits, which depict the interconnection between the components of a SCFS, for day and night operations will be discussed. Second, the design basis and results of a laboratory-scale SCFS will be shown. Third, a preliminary mathematical model will be presented for calculating the SCFS efficiency.

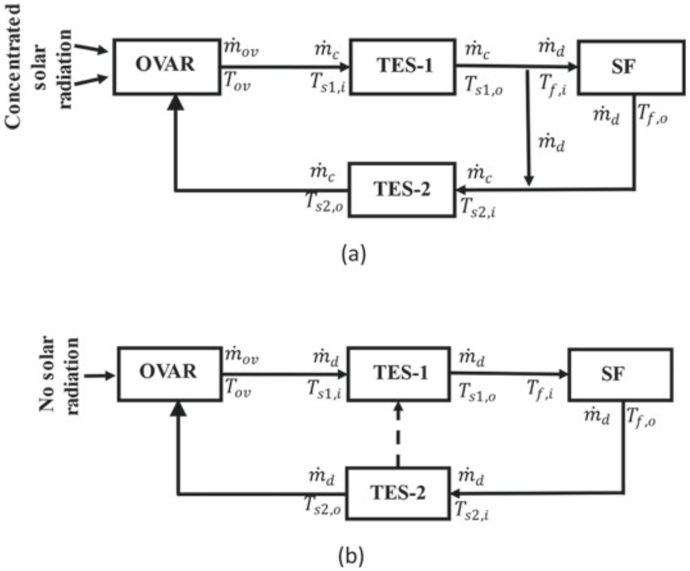

Fig. 1 One possible mode of operation of SCFS between **a** 8 AM to 4 PM (sunny hours) and (**b**) 4 PM to 8 AM (off-sun hours)

Modes of SCFS Operation

Figure 1 shows one of the possible modes for operating the SCFS. Here, the day is divided into two parts: (i) 8 AM to 4 PM when adequate solar radiation, more specifically direct normal irradiance (DNI), is available and (ii) the off-sun hours, 4 PM to 8 AM. This means 8 "sunny" hours are available for charging the TES and 16 h for discharging. Thus, the charging time is half the discharging time. Consequently, the air mass flow rate during charging ($\dot{m}_c$) is twice that of the discharging mass flow rate ($\dot{m}_d$), thatis, $\dot{m}_d = 0.5\dot{m}_c$. In Fig. 1, $\dot{m}$ and T represent the mass flow rates and temperatures at the inlet and outlet of each unit. Subscripts ov, $s1$, $s2$, and f represent the OVAR, TES-1, TES-2, and the soaking furnace (SF), respectively. The inlet and outlet of each unit in Fig. 1 is denoted by subscripts i and o, respectively.

Between 8 AM and 4 PM (see Fig. 1a), hot air from the OVAR charges TES-1, the output from which is split into two streams. One stream is fed into the SF, while the other stream is fed to the inlet of TES-2. Air stream from the outlet of the SF is also directed to the inlet of TES-2. Therefore, TES-2 also serves as an in situ heat recovery system. Since DNI is sufficiently high during 8 AM to 4 PM, hot air from OVAR is fed to the SF through TES-1. This ensures minimum variation in the air temperature at the SF inlet, $T_{f,i}$ [4]. During 4 PM to 8 AM, TES-1 and TES-2 are discharged to provide hot air to the SF (see Fig. 1b). The mode of operation adopted in the laboratory-scale SCFS is relatively simple. Different modes of operation and their viability will be presented in detail in subsequent publications.

Experimental Setup

Figure 2 is a schematic diagram of the experimental setup, which shows the components of an SCFS. Because of the absence of a solar simulator, the absorbers were electrically heated, details of which are given by Sharma et al. [2]. The blower sucks air into the OVAR. Hot air from the OVAR is used to charge TES-1. Air from the

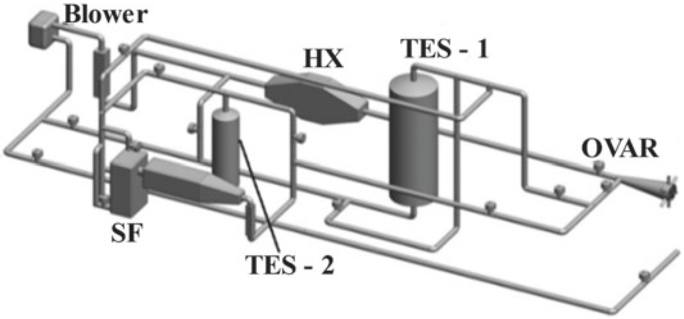

Fig. 2 Schematic diagram of SCFS facility

TES-1 outlet, which will be higher than the ambient temperature, is returned to the OVAR, where a part of the return air is mixed with ambient air and sucked back into the OVAR. After charging TES-1, electrical heating in the OVAR is switched off. Thereafter, ambient air is sucked in for discharging TES-1 for providing hot air to the SF. Air from the SF exit charges the secondary TES-2, and the relatively cooled air is released to the atmosphere.

A brief description of the SF and TES-1 setups is given below. Details of the OVAR are given elsewhere [1–3].

Soaking Furnace

The industrial aluminium soaking furnace at Aditya Birla Group, the world's largest aluminium rolling company, has two sections, namely, heater and hearth. It operates in a batch mode wherein air is recirculated within the furnace between the heater and hearth sections [1]. Air is heated electrically in the heater section, which then heats the ingots. Figure 3 is a schematic diagram of the laboratory SF, which is a 1:15 scale-down model of the Aditya Birla furnace. It is similar to the Aditya Birla furnace except that it operates in a continuous mode. Hot air enters the furnace in the heater section and exits from the hearth section. To ensure uninterrupted soaking of ingots, back-up electrical heaters have been mounted in the heater section along with an external heating unit (EHU). Based on dynamic similarity with the Aditya Birla furnace, a 2-mm-thick steel sheet has been used for the soaking experiments [1].

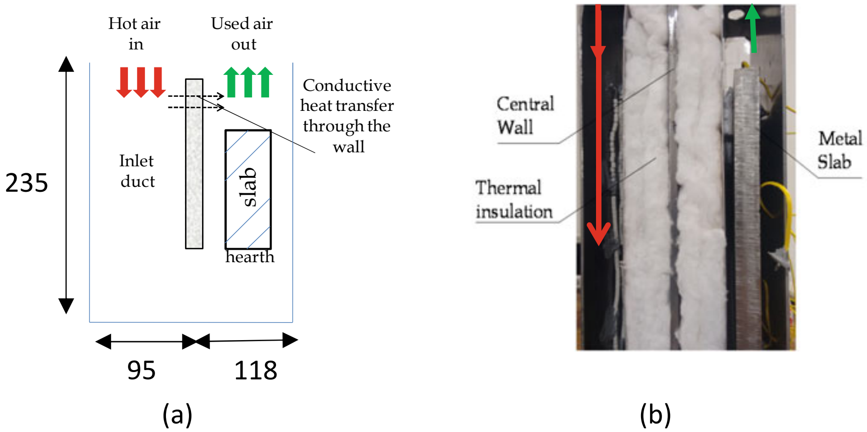

Fig. 3 The laboratory soaking furnace. Dimensions are in mm

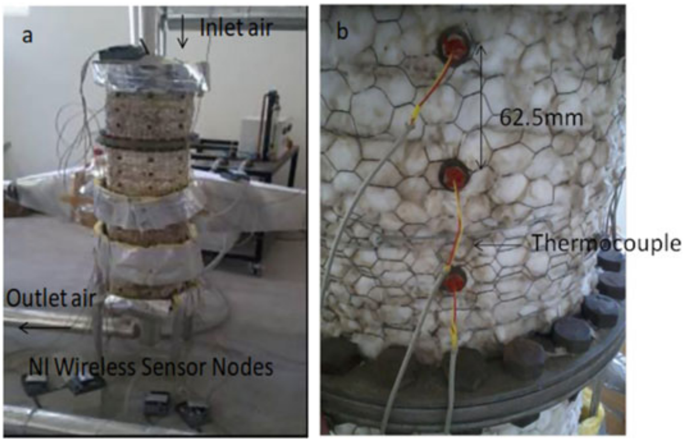

Fig. 4 Photographs of the primary energy storage, TES-1

Thermal Energy Storage

Meier et al. [5] have demonstrated the feasibility of a packed bed of rocks for thermal energy storage with air. Here, the details of the primary thermal energy storage, TES-1, are presented. Figure 4 shows a photograph of TES-1 (height = 1.0 m, inner diameter = 0.25 m, insulation thickness = 0.075 m). The inner and outer insulating layers are resin bonded silicon sealant and ceramic wool, respectively. TES-1 is divided into four chambers (PC1–PC4), with PC1 being the topmost chamber. Each chamber is filled with sandstone pebbles with the following physical properties: $\rho = 2200$ kg.m^{-3}, $c_p = 0.7$ kJ.kg^{-1}.K^{-1}, and $k = 1.3$ W.m^{-1}.K^{-1} [6]. Pebbles with a maximum dimension of 20 mm were selected to ensure Newtonian heating. The bed porosity was 0.39. A total of 48 thermocouples were installed to measure temperature in different sections of TES-1. TES-2, the secondary thermal energy storage, is a 1:4 scale-down model of TES-1. Details of TES design are given in [6].

Operation of SCFS

The sequence of operation in the laboratory SCFS is: (i) charging TES-1 with hot air from the OVAR, (ii) discharging hot air from TES-1 with ambient air for supplying to the SF. The charging and discharging air flow rates are 0.012 kg.s^{-1} and 0.00625 kg.s^{-1}, respectively.

Figure 5 illustrates that ambient air is heated in the OVAR from 32 °C to 250 °C in the first 50 min and then its temperature slowly increases to 310 °C in the next 2.25 h. Lower temperatures at the TES-1 inlet suggests heat loss from the 3-m-long piping between the OVAR and TES-1. As expected, the temperature of pebbles in

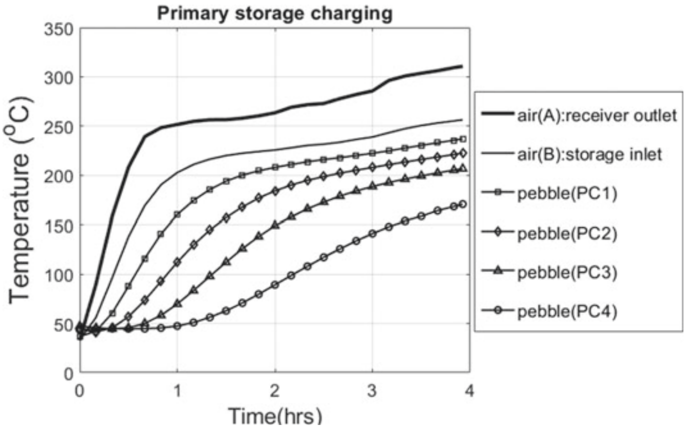

Fig. 5 The measured air and pebble temperatures during the charging of TES-1

the topmost chamber (PC1) is highest. The temperature of air exiting TES-1 will be close to the pebble temperature in PC4.

The charging efficiency (η_C) is defined as the ratio of the energy stored in TES-1 to the sum of energy supplied by air and the energy required for pumping air through TES-1 during the charging period. Experimentally, $\eta_C = 70\%$.

During discharging of TES-1, ambient air enters the lowermost compartment PC4 and leaves from the topmost chamber, PC1. Figure 6 depicts the temperature profiles during the discharging of TES-1. Ambient air is being drawn in through the OVAR with electrical heating switched off. Surprisingly, initial temperature at the TES-1 inlet rises to 120 °C, then drops to 50 °C in 1.3 h, after which it remains unchanged. The initial high air temperature is caused by the transfer of heat to the ambient air

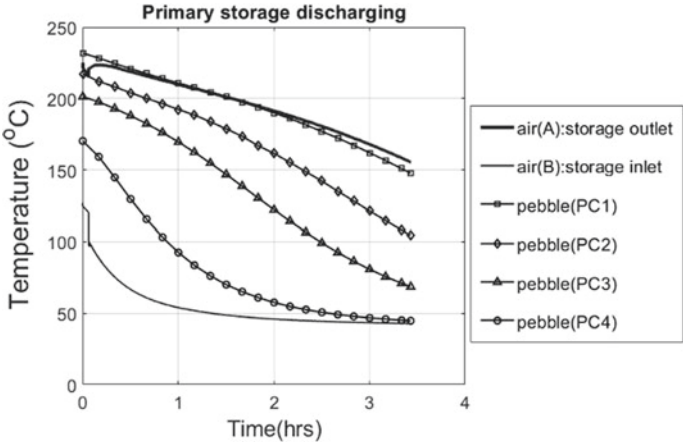

Fig. 6 The measured air and pebble temperatures during the discharging of TES-1

from the preheated 3-m-long pipeline between the OVAR and TES-1. Pipe preheating takes place during TES-1 charging. With time, the pipeline temperature decreases to the ambient temperature. The discharge air temperature at the TES-1 outlet, which is fed to the SF, decreases from 225 °C to about 170 °C. This phenomenon is expected considering the decreasing pebble bed temperature with time.

The experimentally determined discharging efficiency (η_D) was about 75%. η_D is the ratio of total energy recovered from storage by air and the sum of pumping energy and energy stored in storage at the end of the charging period.

During discharging, hot air from the TES-1 outlet flows continuously to the SF. The soaking experiment is divided into two phases: preheating and soaking. During preheating, hot air heats the heater section of the SF. Figure 7 shows the time-dependent air temperature profile at the furnace inlet/outlet and along the height of the steel sheet. Ideally, the temperature profile of air at the furnace inlet should mirror the temperature profile of air at the TES-1 outlet. A comparison of Figs. 5 and 6 clearly shows that the relatively cold 6-m-long piping network from TES-1 to the SF results in a significant drop in the air temperature at its inlet. Figure 7 also shows that there is a 25% drop in temperature in the heater section of the SF. It may be pointed out that the electrical heaters were switched off during the experiments.

The efficacy of the EHU was also tested. Ambient air at 32 °C was directly fed to the SF through the EHU. TES-1 was bypassed. Experiments showed that the EHU increased the ambient air temperature to 130 °C.

The efficiency of the SF (η_F) is defined as the ratio of the energy required to achieve a specific temperature increase in the metal sheet and energy supplied to the furnace by hot air from TES-1 during the discharge period. In the performed experiment, $\eta_F \cong 62\%$.

One major shortcoming of the SCFS has been the low air temperatures in the furnace, primarily due to heat losses in the piping network and the heater section of

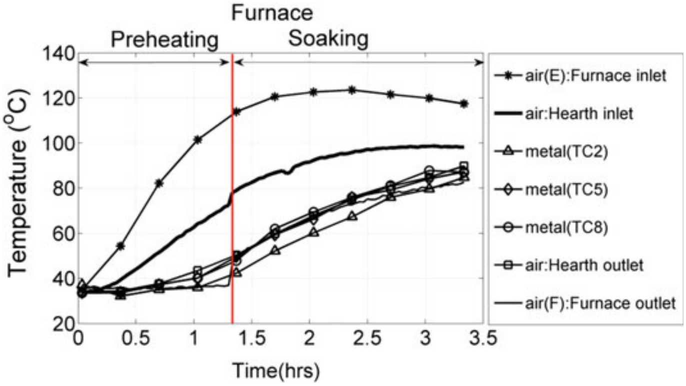

Fig. 7 Temperature profile of (i) air at the retrofitted SF inlet/outlet and (ii) steel sheet as a function of height (TC2, TC5, TC8). Thermocouples TC2 and TC8 are located near the top and bottom of the steel sheet, respectively

the laboratory SF. Consequently, the secondary storage was not analysed in detail. However, the main purpose of these experiments was to demonstrate the implementation of a SCFS and collect data for the development of a mathematical model for designing an industrial SCFS.

Mathematical Model of SCFS Efficiency

The SCFS efficiency (η_{SCFS}) can be defined in terms of the efficiencies of the subsystems, namely, OVAR (η_{OV}), TES-1 charging (η_C), TES-1 discharging (η_D), and the SF (η_F):

$$\eta_{SCFS} = \eta_{ov}\eta_C\eta_D\eta_F \tag{1}$$

where η_{OV} is the fraction of concentrated solar irradiance ($\dot{Q}$ in W.m^{-2}) incident on the OVAR that is absorbed by air, an expression for which is given below [7]:

$$\eta_{OV} = 0.99\left(\dot{Q}/\dot{m}_{ov}\right)^{-0.08}(1-\gamma)^{-0.34} \tag{2}$$

In Eq. 2, γ is the absorber porosity and $\dot{m}_{ov}$ is the air mass flow rate through the OVAR (see Fig. 1). Thus, η_{OV} can be calculated as a function of the design (γ) and operating parameters ($\dot{Q}$, $\dot{m}_{ov}$) of an OVAR.

In a subsequent publication, the procedure for calculating η_{SCFS} for more realistic modes of operation, such as that shown in Fig. 1, will be presented. This will require detailed fluid flow and heat transfer simulation of thermal energy storage and the retrofitted SF.

Conclusions

This work presents the design and operation of a laboratory-scale SCFS. Experiments demonstrated that SCFS is a viable concept. Incorporation of multiple soaking furnaces in the SCFS, as in industrial practice, will also be a subject of further studies.

Acknowledgements The authors are grateful for financial support from the Ministry of New and Renewable Energy, Govt. of India through Grant No. 15/40/2010-11/ST.

References

1. Patidar D, Tiwari S, Sharma P, Pardeshi R, Chandra L, Shekhar R (2015) JOM 67:2696–2704
2. Sharma P, Sarma R, Chandra L, Shekhar R, Ghoshdastidar PS (2015) Sol Energy 111:135–150
3. Sharma P, Chandra L, Ghoshdastidar PS, Shekhar R (2020) Sol Energy 204:246–255
4. Zanganeh G, Pedretti A, Haselbacher A, Steinfeld A (2015) Appl Energy 137:812–822
5. Meier A, Winkler C, Wuillemin D (1991) Sol Energy Mater 24:255–264
6. Kumar D (2013) Design and evaluation of experimental thermal energy storage, Master of Technology Thesis. Indian Institute of Technology Jodhpur, India
7. Singh G, Dhurwe P, Kumar R, Kumar L, Vaghela N, Chandra L (2018) INAE Lett 4:161–169

Part III

Thermal Management and Hydrogen Technology

Heat Island Mitigation Strategy for Urban Areas Using Phase Change Materials (PCM)

Ganesan Subramanian and Neale R. Neelameggham

Abstract Heat islands are urbanized areas that experience significantly higher day and night time temperatures than the surrounding rural areas on account of the influence of the buildings, roadways, and industries on the local weather. Heat island mitigation strategy depends on the weather patterns at the urban geographical location. Mitigation of heat island effect has been demonstrated by increased use of shade and materials that alter the reflectance and emissivity of the surfaces impacted by solar radiation. Interest in the use of PCM for urban infrastructure for further enhancing the mitigation through heat storage and liberation is more recent. Key physical properties needed for PCM use are the latent heat of fusion, thermal conductivity, density, and specific heat. This paper reviews the physics involved in choosing the right PCM for buildings, placement of PCM in the infrastructure, and modeling methods for optimal energy costs.

Keywords Heat island mitigation · PCM

Introduction

The heat island effect [1, 2] is a well-studied phenomenon in urban areas where the concentration of buildings, roadways, and industries generates local weather conditions that are more extreme than the surrounding rural areas, leading to thermal discomfort or extreme events like flooding. Mitigation of heat island effect has been demonstrated by increased use of shade and materials that alter the reflectance and emissivity of the surfaces impacted by solar radiation. Local weather patterns are further influenced in recent times on account of global climate change. PCM incorporation into urban infrastructure is an efficient, reliable, and inexpensive way to further mitigate the heat island effect and ensure thermal comfort, at the same time

---

G. Subramanian (✉)
SaiSim LLC, Bellaire, TX, USA

N. R. Neelameggham
Ind LLC, South Jordan, UT, USA

F. Tesfaye et al. (eds.), *REWAS 2022: Energy Technologies and CO_2 Management (Volume II)*, The Minerals, Metals & Materials Series,
https://doi.org/10.1007/978-3-030-92559-8_12

reducing emissions from the use of fossil fuels and reducing heating and cooling loads.

Building construction and operations accounted for the largest share of both global final energy use (36%) and energy-related CO_2 emissions (39%) in 2018 [3] (Fig. 1). Construction industry is the portion (estimated) of overall industry devoted to manufacturing building construction materials such as steel, cement, and glass. Indirect emissions are emissions from power generation for electricity and commercial heat. The buildings and construction sector should therefore be a primary target for GHG emission mitigation efforts, as it accounted for 36% of final energy use and 39% of energy- and process-related emissions in 2018. Growth of urban areas will increase this share in the future (Fig. 2).

Thermal energy storage (TES) is the equivalent of a battery that stores electrical energy and can be used to store heat or cold during overproduction of heat or electricity for use at a later time, thus improving system efficiency by reducing peak cooling and heating demands. Thermal energy storage using PCMs takes advantage of their high energy density available as latent heat at constant temperature with practical applications using the solid-to-liquid transition. The high latent heat of fusion allows PCMs to store 5–14 times more heat per unit volume than common sensible heat storage materials like rock or water [4, 5]. Common applications of different type of PCMs are shown in Fig. 3.

Any candidate material to be used as PCM shall have first of all large latent heat and ideally high thermal conductivity. There is however no perfect PCM, and the

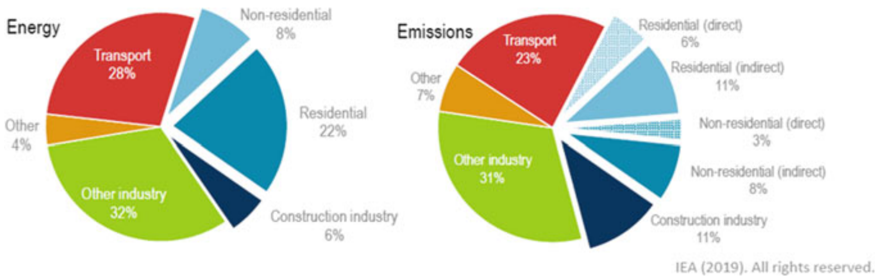

Fig. 1 Building industry global share of energy and emissions in 2018 [3]

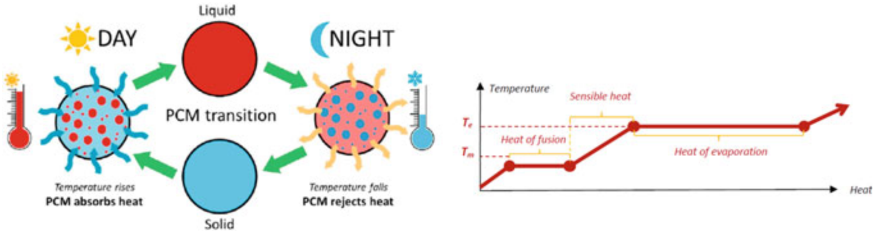

Fig. 2 How PCMs work as thermal storage materials [6, 4]

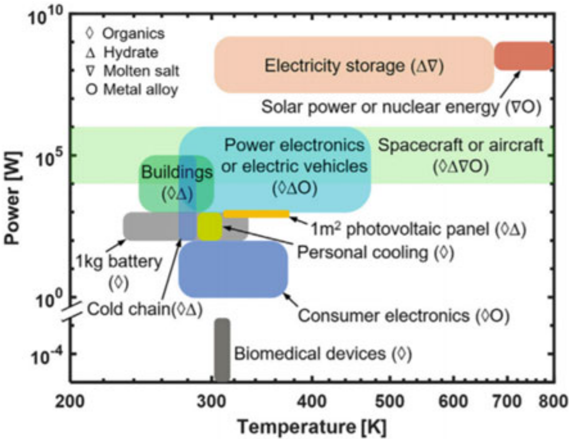

Fig. 3 Emerging applications of PCM thermal storage with PCM types and temperature ranges [20]

choice of material is always a compromise. The main characteristics required for a useful PCM are as follows:

Thermo-physical properties:

- Phase change temperature within the range appropriate to the application.
- Large latent heat per unit volume.
- Large sensible heat per unit volume.
- High thermal conductivity in both phases.
- Small volume changes due to the phase transition.
- Congruent phase change (no component segregation in the solid phase).
- Sharpness of latent heat release and absorption: should occur over a narrow temperature.
- Range, depending on the application [8].

Nucleation and crystal growth:

- High nucleation rate (to avoid supercooling of the liquid during solidification and consecutive temperature hysteresis between solidification and melting).
- High crystal growth rate (enabling fast charging/discharging of the PCM reservoir).

Chemical properties:

- Entirely reversible solidification/melting process.
- No chemical degradation with time and number of charging/discharging cycles.
- No corrosive properties to the construction/encapsulation materials.
- Non-toxic, non-flammable, and non-explosive.

Economics and usability:

- Easily available at low cost.
- Easily recyclable.
- Good environmental parameters based on Life Cycle Assessment.

Characteristics of the different types of PCM are summarized in the table below:

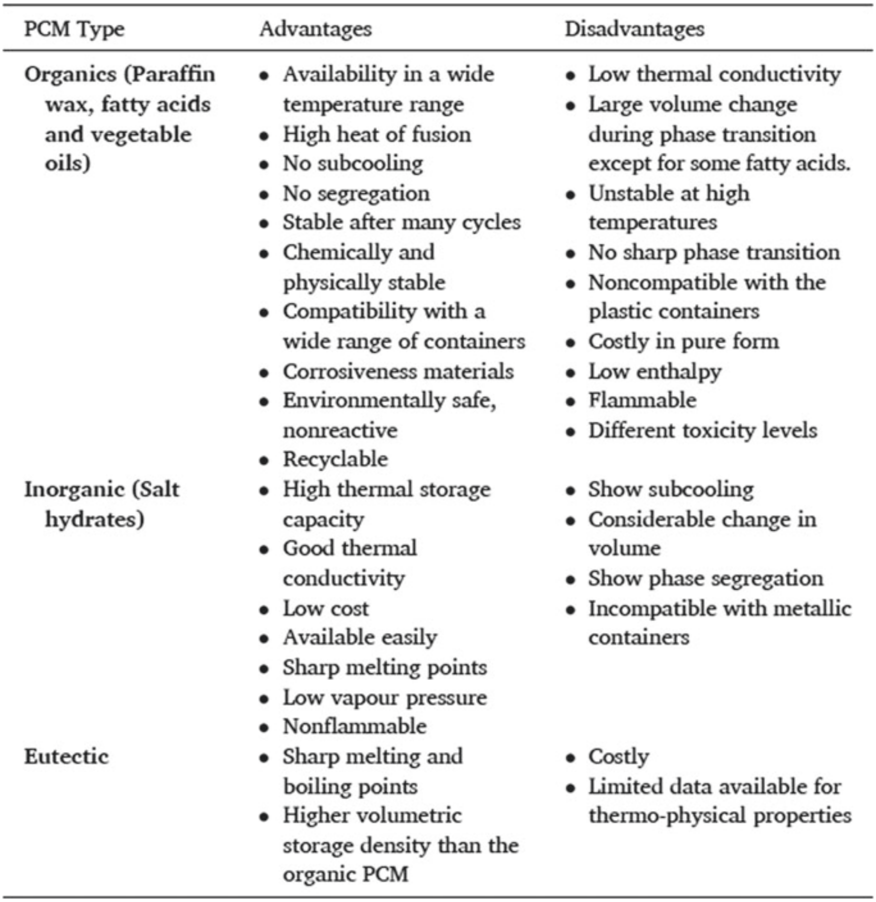

PCM Type	Advantages	Disadvantages
Organics (Paraffin wax, fatty acids and vegetable oils)	• Availability in a wide temperature range • High heat of fusion • No subcooling • No segregation • Stable after many cycles • Chemically and physically stable • Compatibility with a wide range of containers • Corrosiveness materials • Environmentally safe, nonreactive • Recyclable	• Low thermal conductivity • Large volume change during phase transition except for some fatty acids. • Unstable at high temperatures • No sharp phase transition • Noncompatible with the plastic containers • Costly in pure form • Low enthalpy • Flammable • Different toxicity levels
Inorganic (Salt hydrates)	• High thermal storage capacity • Good thermal conductivity • Low cost • Available easily • Sharp melting points • Low vapour pressure • Nonflammable	• Show subcooling • Considerable change in volume • Show phase segregation • Incompatible with metallic containers
Eutectic	• Sharp melting and boiling points • Higher volumetric storage density than the organic PCM	• Costly • Limited data available for thermo-physical properties

For "Green" buildings, inorganic PCMs are preferred if they can be incorporated into the building infrastructure easily. In practice, however, modifications to overcome the disadvantages are done through mixing the different types in the form of composites, encapsulation (macro and micro), or foams, when it becomes a challenge to estimate the basic physical properties of latent heat, density, specific heat, and thermal conductivity. In such cases, there are many experimental techniques available for direct determination of these properties. Temperature range of different PCM types is shown in Fig. 4 from [6].

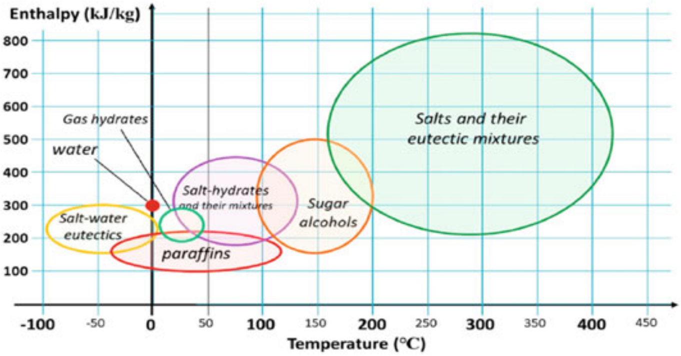

Fig. 4 Working range of enthalpy and temperature of various PCMs [6]

PCM Incorporation into Buildings

Practically, PCMs are incorporated into building envelope elements by one of the following methods: (a) direct incorporation, (b) immersion, (c) encapsulation (micro- or macroencapsulation), (d) shape-stabilized PCMs, and (e) form-stable PCM composites. In the *direct incorporation* method, the PCM in powder or liquid state is added directly to the construction material, such as gypsum mortar, cement mortar, and concrete mixture. This method is the easiest and most economical because it does not require any experience and is easy to incorporate. On the contrary, the major drawback of this method is the leakage of PCM during the melting phase. This leakage causes incompatibility of mixed materials and increases the risk of fire (for flammable PCMs). In addition, this method weakens the mechanical properties of constructed elements during high temperatures given that the PCM is added to the mixture in a liquid state, thereby decreasing the water content ratio. In the *immersion method*, a porous construction material immerses into the liquid PCM; it is absorbed due to capillarity. The main drawbacks of this method are leakage, construction incompatibility, and the corrosion of reinforced steel when incorporated with concrete elements, thereby affecting its service life. *Encapsulation* is a suitable method to avoid the leakage issues of PCM and to enhance its compatibility with the building structure. Encapsulation is performed by covering the PCM by a shell for protection from the outside environment as well as for leakage prevention. This method is also essential to increase the heat transfer area and, hence, the thermal conductivity of PCM to ensure effective utilization of its storage capacity. The PCM can be macroencapsulated using shells, tubes, channels, and thin plates or microencapsulated when the microsized PCM is covered by unique polymeric material [7, 8, 13]. In both methods, the encapsulation material should have unique characteristics, such as preventing leakage, retaining all thermal characteristics of PCM, not reacting with PCM, compatible with PCM and its application, providing structural stability and securing handling [9]. Furthermore, it should control any volumetric change of PCM during phase changes and provide appropriate protection for the PCM against environmental degradation and good thermal conductivity and mechanical strength over PCM life cycles [10]. Pipes, panels, and foils made from aluminum, copper, and stainless steel are commonly used for macroencapsulation because they offer excellent thermal conductivity, compatibility, and support to the mechanical strength of building materials [11]. More macroencapsulation forms are shown in Fig. 5. The *shape-stabilized* method contains the PCM inside a carrier matrix. This method is promising because it provides better thermal conductivity, large specific heat, and maintain the shape over many cycles of phase transition. More information regarding its configurations and preparation techniques have been described by Refs. [12]. The *form-stabilized* PCM is also an advanced method of incorporation. It is a specific definition of composite material, retaining the maximum amount of one or more types of PCM and showing no leakage at melting temperatures. Although the two latter methods are expensive to implement, they are the most reliable amongst others. Reliability indicates that the PCM cycles (melting/solidification) are repeated in high performance without degradation, and this feature is crucial for applications that require high performance for long term, such as buildings.

Recently, Peiran Wei et al. [14] examined the direct insertion of PCM into a building material using 3D printing for scalability. Paraffin wax as PCM was mixed with liquid resin as the supporting structure, creating a soft, paste-like material that can be shaped as needed. Once it's in the desired shape, it can be cured with UV light to harden the resin. The end result is a solid material strong enough to build with, containing pockets of PCM inside. Without the need for extra shells, the PCM can be packed in more densely, comprising up to 63 weight percent of the material, which boosts its ability to regulate the ambient temperature. But perhaps most importantly, the material is now easier to make in bulk. Its squishiness means it can be made into a 3D-printable ink, which could then be made into whatever shape or size is desired, for much lower cost than other PCM building materials (Fig. 6).

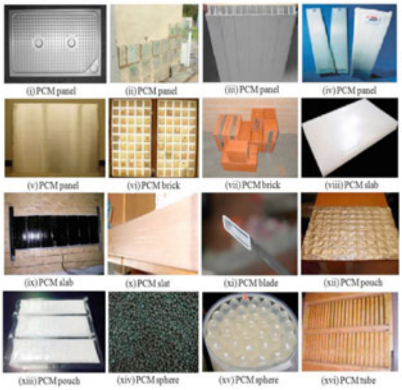
(i) PCM panel
(ii) PCM panel
(iii) PCM panel
(iv) PCM panel
(v) PCM panel
(vi) PCM brick
(vii) PCM brick
(viii) PCM slab
(ix) PCM slab
(x) PCM slat
(xi) PCM blade
(xii) PCM pouch
(xiii) PCM pouch
(xiv) PCM sphere
(xv) PCM sphere
(xvi) PCM tube

Commercially available PCMs

PCM type	PCM symbol	PCM from manufacturer's data sheet (°C)	Manufacturer
Bulk	RT21 HC	21	Rubitherm
	RT22 HC	22	Rubitherm
	RT25 HC	25	Rubitherm
	RT27	27	Rubitherm
	PureTemp 23	23	Entropy Solutions
Microencapsulated	Micronal DS5040X	23	BASF
	Micronal DS5008X	25	BASF
	MPCM24D	24	BASF
	Micronal DS5038X	25	Microteklabs
Microencapsulated	MacroPCM28	28	Microteklabs
	MacroPCM24	24	Microteklabs

Fig. 5 Different macroencapsulation forms used with building structure [6]

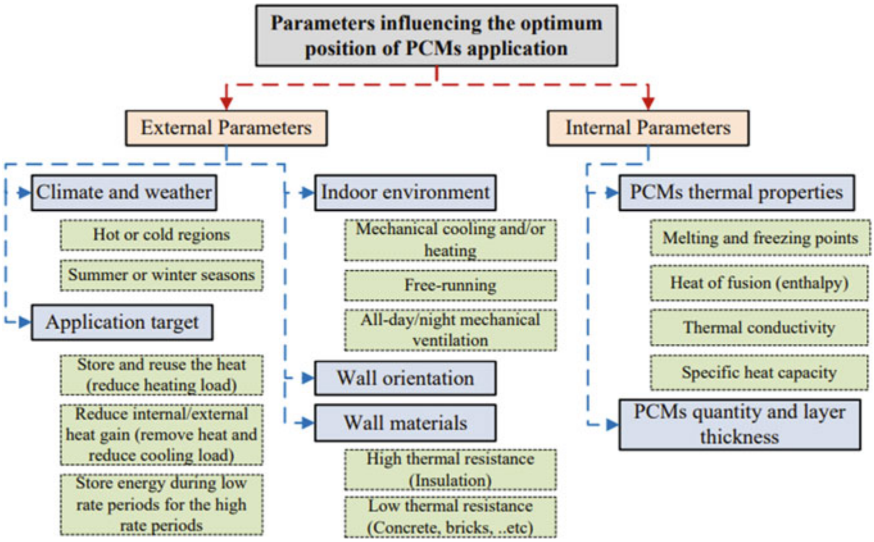

Fig. 6 Main parameters that influence the optimum position of the PCM application in building [6]

Air Conditioning Application with PCM as Air Heat Exchanger

So far we have reviewed PCMs in a passive mode as part of the building infrastructure. Chaiyat and Kiartsiriroot [19] experimentally demonstrated that the active mode use of PCM (Paraffin wax Rubitherm20, RT-20) as an air heat exchanger in conjunction with the air conditioning system can result in reducing cooling loads as much as 10%. The air conditioner controls the room temperature at around 15–20 °C. The return air with temperature of around 22–25 °C, slightly higher than the PCM melting point of 20 °C, is fed to the PCM bed (Fig. 7c) and would enter the evaporator at 20 °C, lower than the ambient, thus reducing the cooling load. In the charging mode (Fig. 7b), the supply air from the evaporator is bypassed through the PCM bed, allowing it to freeze.

Experimental Measurement of PCM Physical Properties

Experimental measurement of specific heat, thermal conductivity, and density can be done by various techniques and for complex PCMs, for example, microencapsulated or composites, this is the only reliable method [7]. Common methods are conventional calorimetry, differential thermal analysis (DTA), and differential scanning calorimetry (DSC). Although DTA and DSC methods are well developed, the

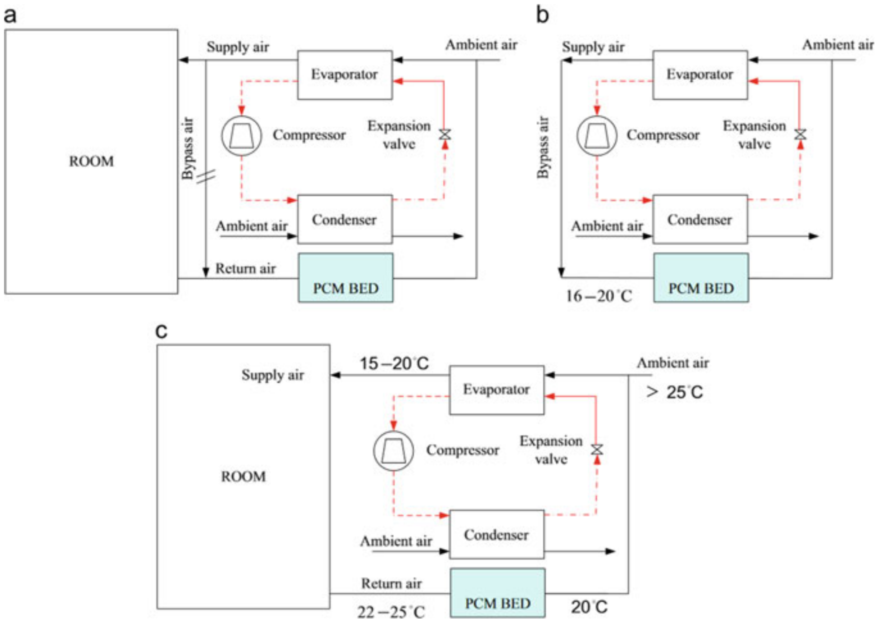

Fig. 7 Air conditioning scheme with PCM air heat exchanger [19]

samples tested by them are very small (1–10 mg) and the thermophysical properties of samples are usually different from those of the bulk materials used in practical systems. DTA and DSC measurement rigs are complicated and expensive; they cannot measure heats of fusion, specific heats, and thermal conductivities of several PCM samples simultaneously. Besides, the phase change process of a PCM sample during a measurement is hard to observe clearly when using conventional methods. Zhang et al. [15] have developed a "T-history" method, of determining the melting point, degree of supercooling, heat of fusion, specific heat, and thermal conductivity of several PCM samples simultaneously. It is especially useful for the selection from a list of candidate PCMs or for the preparation of new PCMs for use in practical systems.

Modelling of PCM-Enhanced Building Envelope

In recent years, different types of modelling and simulation tools have been applied to describe the thermal behavior of PCM and energy saving gained from its incorporation with building components. Experimentally, some researchers work on a laboratory-scale level whilst others work on whole-building level to validate the tools. The most widely used tools for modelling and simulating PCM behavior are compared by Vadiee et al. [16]. ANSYS FLUENT, COMSOL multiphysics, EnergyPlus, TRYNSYS, MATLAB, ABAQUS™ solver, and DIANA–finite element analysis. Although many researchers reported good agreement of computational tools with the experimental results, IEA states that the confidence level of these tools is still low and cannot be adapted for designing and coding. To model PCM-incorporated buildings, most researchers deal with the building element as a 1D convective heat transfer, unsteady-state without internal heat source to describe the heat behavior of PCM [16]. Zhang et al. [17] developed a new approach to model the building envelope that picks the optimum PCM that satisfies the material and energy balances in the building environment within the thermal comfort constraints (Fig. 8). Some of their results comparing the savings with PCM are shown in Fig. 9.

Multiphysics modeling of PCMs at different length scales is governed by different scale-dependent mechanisms. Based on these mechanisms and empirical parameters, computational methods are developed to predict, design, and optimize materials, devices, and systems. Experimental methods provide approaches that enable material synthesis and characterization, property measurements, and manufacturing and

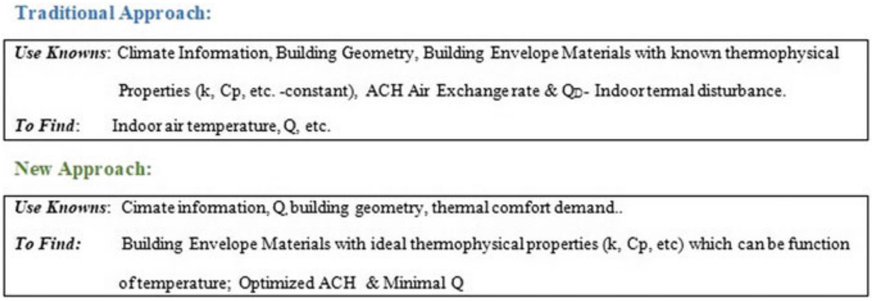
Traditional Approach:

Use Knowns: Climate Infomation, Building Geometry, Building Envelope Materials with known thermophysical Properties (k, Cp, etc. -constant), ACH Air Exchange rate & Q_D- Indoor termal disturbance.

To Find: Indoor air temperature, Q, etc.

New Approach:

Use Knowns: Cimate infomation, Q building geometry, thermal comfort demand..

To Find: Building Envelope Materials with ideal thermophysical properties (k, Cp, etc) which can be function of temperature; Optimized ACH & Minimal Q

Fig. 8 Modeling method for choosing the best PCM by optimizing the right variables (Derived from [17])

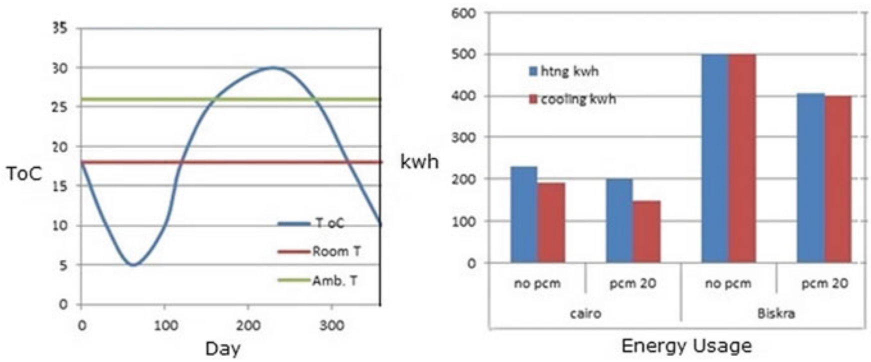

Fig. 9 Results for thermal comfort range and energy savings using new approach for optimal PCM (derived from [17])

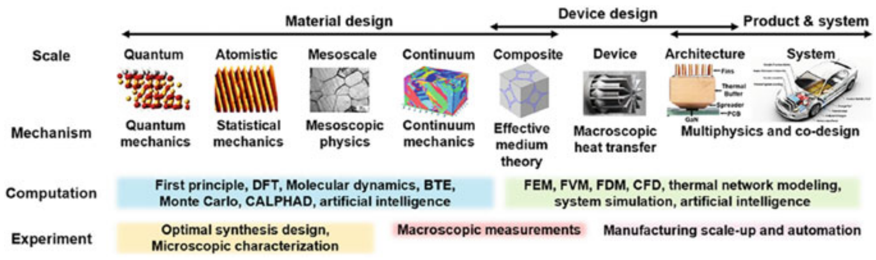

Fig. 10 Length scales and associated modeling, design, and test methods for PCMs, devices, and systems [20]

prototype testing. BTE, Boltzmann transport equation; CFD, computational fluid dynamics; and FDM, finite difference method.

Summary

This paper has surveyed the role of phase change material incorporation into buildings as an inexpensive means of mitigating the heat island effect that has been exacerbated in recent times on account of climate change. Recent advances in micro- and macroencapsulation technology have made the incorporation of PCMs into building infrastructure practical and economical. The research and development opportunity for material and building scientists and engineers from the material design stage through device design to the product and system is captured in Fig. 10 from [20].

Declaration The authors declare no commercial use of the figures referenced and used in this review paper for personal gain.

References

1. Kalnay E, Cai M (2003) Impact of urbanization and land-use change on climate. Nature 423(6939):528–531
2. https://www.epa.gov/heatislands
3. Global share of buildings and construction final energy and emissions (2019) 2018 IEA. https://www.iea.org/reports/global-status-report-for-buildings-and-construction-2019
4. Sevault A, Kauko H, Bugge M, Banasiak K, Haugen NE, Skreiberg Ø (2017) SINTEF energy research report TR A7638
5. Memon SA (2014) Phase change materials integrated in building walls: a state of the art review. Renew Sust Energy Rev 31:870–906
6. Al-Yasiri Q, Szab´o M (2021) Incorporation of phase change materials into building envelope for thermal comfort and energy saving: a comprehensive analysis, vol 36, April 2021, Article 102122. https://doi.org/10.1016/j.jobe.2020.102122

7. Saxena R, Rakshit D, Kaushik SC (2020) Experimental assessment of Phase Change Material (PCM) embedded bricks for passive conditioning in buildings, Renew. Energy 149:587–599. https://doi.org/10.1016/j.renene.2019.12.081
8. Liu Z, Yu Z(Jerry), Yang T, Qin D, Li S, Zhang G, Haghighat F, Joybari MM (2018) A review on macro-encapsulated phase change material for building envelope applications. Build Environ 144:281–294. https://doi.org/10.1016/j.buildenv.2018.08.030
9. Lu S, Li Y, Kong X, Pang B, Chen Y, Zheng S, Sun L (2017) A review of PCM energy storage technology used in buildings for the global warming solution. In: Zhang X, Dincer I (eds) Energy solutions to combat global warming. Springer International Publishing, Cham, pp 611–644. https://doi.org/10.1007/978–3–319–26950–4_31
10. Pereira da Cunha J, Eames P (2016) Thermal energy storage for low and medium temperature applications using phase change materials—a review. Appl Energy 177:227–238
11. Mili´an YE, Guti´errez A, Gr´ageda M, Ushak S (2017) A review on encapsulation techniques for inorganic phase change materials and the influence on their thermophysical properties. Renew Sustain Energy Rev 73:983–999. https://doi.org/10.1016/j.rser.2017.01.159
12. Bland A, Khzouz M, Statheros T, Gkanas EI (2017) PCMs for residential building applications: a short review focused on disadvantages and proposals for future development. Buildings 7:78. https://doi.org/10.3390/buildings7030078
13. Singh Rathore PK, Shukla SK, Gupta NK (2020) Potential of microencapsulated PCM for energy savings in buildings: a critical review. Sustain Cities Soc 53:101884. https://doi.org/10.1016/j.scs.2019.101884
14. Wei P, Cipriani CE, Pentzer EB (2021) Thermal energy regulation with 3D printed polymer-phase change material composites. Matter 4:1975–1989. https://doi.org/10.1016/j.matt.2021.03.019
15. Yinping Z, Yi J, Yi J (1999)A simple method, the T –history method, of determining the heat of fusion, specific heat and thermal conductivity of phase-change materials. Meas Sci Technol 10:201–205
16. Vadiee A, Dodoo A, Gustavsson L (2019) A comparison between four dynamic energy modeling tools for simulation of space heating demand of buildings. In: Johansson D, Bagge H, Wahlström Å (eds) Cold climate HVAC 2018. CCC 2018. Springer Proceedings in Energy. Springer, Cham, pp. 701–711. https://doi.org/10.1007/978-3-030-00662-4_59
17. Zeng R, Wang X, Di H, Jiang F, Zhang Y (2011) New concepts and approach for developing energy efficient buildings: ideal specific heat for building internal thermal mass. Energy Build 43:1081–1090
18. Al-Absi ZA, Mohd Isa MH, Ismail M (2020) Phase change materials (PCMs) and their optimum position in building walls. Sustainability 12:1294. https://doi.org/10.3390/su12041294
19. Chaiyat N, Kiatsiriroat T (2014) Energy reduction of building air-conditioner with phase change material in Thailand. Case Stud Thermal Eng 4:175–186
20. Yang T, King WP, Miljkovic N (2021) Phase change material-based thermal energy storage. Cell Rep Phys Sci 2:8, article 100540. https://doi.org/10.1016/j.xcrp.2021.100540

Geomimicry-Inspired Micro-Nano Concrete as Subsurface Hydraulic Barrier Materials: Learning from Shale Rocks as Best Geological Seals

Cody Massion, Vamsi S. K. Vissa, Yunxing Lu, Dustin Crandall, Andrew Bunger, and Mileva Radonjic

Abstract Wellbore cement is the primary hydraulic barrier material used in wellbore construction, with properties similar to the formation rock. It serves multiple purposes such as providing mechanical support and zonal isolation, maintaining well performance, and restoring sealing barriers during the wellbore abandonment. However, Portland cement can have a brittle nature making it subject to mechanical failure at downhole conditions. To improve wellbore cement properties that impact it resistance to failure, three materials are explored as additives: (1) olivine to prevent chemical attack from CO_2-rich geofluids, (2) zeolite for its water storage and slow moisture release that can potentially prevent drying shrinkage, thus allowing secondary cement hydration and potentially promoting self-healing capabilities, and (3) graphene to increase strength and/or decrease tendency of the material to brittle fracture. Investigation of the mechanism for how each of these micro-nano aggregates contributes to the enhanced performance of the cement matrix indicates that all can have positive impact on cement properties that enable effective and resilient zonal isolation.

Keywords Hydraulic barrier materials · Graphene cement · Zeolite cement · Olivine cement · High-temperature high pressure · Plugging and abandonment

---

C. Massion · V. S. K. Vissa · M. Radonjic (✉)
Hydraulic Barrier Materials Lab, The School of Chemical Engineering, Oklahoma State University, Stillwater, OK 74078, USA
e-mail: mileva.radonjic@okstate.edu

Y. Lu · A. Bunger
Civil and Environmental Engineering, University of Pittsburgh, Pittsburgh, PA 15261, USA

A. Bunger
Chemical and Petroleum Engineering, University of Pittsburgh, Pittsburgh, PA 15261, USA

D. Crandall
US Department of Energy, National Energy Technology Laboratory, Morgantown, WV 26507, USA

F. Tesfaye et al. (eds.), *REWAS 2022: Energy Technologies and CO_2 Management (Volume II)*, The Minerals, Metals & Materials Series,
https://doi.org/10.1007/978-3-030-92559-8_13

Introduction

It has been observed that leakage from oil and gas wells, in 2018, resulted in the U.S. Environmental Protection Agency Greenhouse Gas Inventory (GHGI) reporting 281 kilotons of methane gas being released into the atmosphere [1]. Further studies indicate that the amount of leaking methane could be higher than this number by 60–100 percent [2, 3]. Because of this, one of the most important parts in any wellbore construction or decommission is maintaining the well integrity. This is achieved with the use of cement to hold the casing in place, uphold zonal isolation, prevent circulation loss, and seal the reservoir for plugging and abandonment. A shortcoming of using cement is its brittle nature that can lead to fracturing and failure when subject contamination by the drilling fluid, cyclic high temperatures and pressures the well encounters in subsurface operations [4–8]. To endure these conditions and improve cement performance, the use of graphene nanoplatelets (GNPs), geothermally formed zeolite, and olivine are proposed as additives to the cement slurry to form a stronger and more resilient cement material.

Graphene is made of carbon atoms in a flat two-dimensional hexagonal lattice that link up to create a honeycomb-like sheet structure that is the thinnest and strongest material known at this time [9]. The intrinsic properties of these graphene-based materials, that have high strength, flexibility, surface area, thermal and electrical conductivity although being lightweight, makes them suitable for applications in new technologies and material composites [10, 11]. To help prevent fracturing and failure of the cement, it has been proposed that low percentages ($<0.1\%$) of graphene nanoplatelets can be added to transfer some of its intrinsic mechanical properties to the cement matrix.

Zeolite has seen uses in the cement industry beginning with research on chabazite and clinoptilolite in cement [12–15]. More recent studies have included property enhancements by the use of zeolites like Ferrierite which had even shown self-healing in geothermal cements [16, 17]. We aim to achieve an improved cement blend with enhanced performance properties by the addition of these two materials.

Olivine, which is abundant in high-temperature igneous rock with forsterite and fayalite endmembers of the $(Mg, Fe)_2SiO_4$ olivine series, is a nesosilicate having equal bond strengths in all directions with a specific gravity between 3.27 and 4.37 and hardness of 6.5–7.0 [18]. The purpose of adding olivine into cement is taking the advantages of olivine's enhanced carbonation rate at high temperature and high pressure which will convert CO_2 to stable carbonate minerals mitigating the risk of CO_2 leakage and reducing the concerns over long-term monitoring and liability issues [19, 20].

Thus, the objective of the study reported in this paper is to investigate the impact of graphene nanoplatelets, micronized zeolites, and olivine as additives to wellbore cement, understanding the additive impact to mechanical and microstructural properties that translate to the required field performance. Experiments were carried out to evaluate the effects of these three additives on reinforcement on the Young's modulus, confined compressive strength, and hardness. At the same time, pore-scale measurement and imaging were carried out to trace the micromechanical origins of the observed impacts for these additives on cement properties.

Materials and Methods

Three additives used in this study were purchased from different suppliers. The graphene was derived from refined biomaterials remanence that supplied by CarbonEra Platinum. The olivine sand was ground from ultramafic rock and supplied by Reade Advanced Materials. Zeolites were received from the Trabits group as rocks and were ground into fine micron-sized powders with a particle size of ~95 μm to be added in cement.

All three additives were first examined as received for nanostructure, composition, and chemical stability by methods of scanning electron microscopy (SEM) and Energy-Dispersive X-ray Spectroscopy (EDS). They were then added to Class-H wellbore cement at 0.008, 0.016, and 0.05% by weight of cement (bwoc) for graphene and 5, 15, and 30% bwoc for zeolite, and 5, 15, and 30% bwoc for olivine, along with D-air 5000 at 0.25%bwoc, dispersant CFR-3 at 0.30% bwoc, and bentonite at 2.0%bwoc to make cement at a slurry of density 16.4ppg (1.94 g/cm^3) and a water to cement ratio of 0.38.

Cement Curing and Pre-test Preparations

Cement slurry was cast in both 1 inch and 30 mm diameter molds in order to suit dimensional requirements of testing equipment. The molds were covered with cling wrap to prevent any fluid loss by evaporation and set to hydrate at ambient conditions for 24 h. After 24 h, they were demolded and immediately submerged in calcium hydroxide solution of ~pH13 and covered with aluminum foil and sealed with saran wrap. The samples in solution were placed in an environmental chamber and cured at 90 °C and 95% relative humidity to simulate subsurface wellbore conditions. Samples were cured at these conditions for 28 days. Hydrated (set) cement cores were first wet cut using a band saw to trim uneven edges and create flat parallel ends. Samples used for SEM and indentation were polished starting with a 600-grit silicon carbide (SIC) abrasive disc used for grinding to remove initial deformations. After each step, the surfaces are inspected under the microscope to ensure a uniform scratch pattern. Grinding induced deformation is removed using 6 μm diamond suspension on Gold Label polishing cloth and 1 μm diamond suspension on White Label polishing cloth, with Purple-Lube. Samples are sonicated with isopropyl alcohol in a tabletop sonicating bath for 5 min at the end of each step to remove fragmented cement, residual diamond suspension, and colloidal silica. The polished samples are then dried overnight in a drying oven at 50 °C, and further water removal is done prior to SEM, as samples are coated and analyzed.

Scanning Electron Microscopy (SEM) and Energy-Dispersive Spectroscopy (EDS)

A flat and smooth surface for the polished samples of cement was achieved by following the polishing procedure listed below in Sect. 2.2. Polished and fractured cement surfaces were iridium-coated to prevent charging effects before imaging with Thermofisher Scios2 SEM, using secondary electron (SE) at 20 keV and backscatter electron (BSE) at 12 keV, and EDS, using 12 keV and acquisition time of approximately 30 min.

Triaxial Compression Test

In this study, a triaxial test was used to determine the ultimate axial strength and stiffness of the specimen. The triaxial tests are performed in a temperature-controlled Hoek-type triaxial compression cell, which consists of three main parts: axial loading system, confining stress system, and temperature system. The experimental approach entailed applying confining pressure and temperature replicating downhole conditions while simultaneously imposing the increasing axial (deviatoric) load until the specimen fails. The deviatoric loading was controlled by an INSTRON-600DX load frame, up to 600KN. The confining stress was maintained by a high-pressure syringe pump (ISCO-260D), which also allowed precise measurement of the volume change of the specimen associated with a given confining stress up to 70 MPa. The temperature was provided by wrapping the Hoek cell with the heating tape that provided a controlled temperature up to 180 °C. After the desired system temperature was achieved and stabilized, the confining pressure and vertical load were increased to the targeted downhole pressure value, so the specimen was initially loaded isotropically, and then the deviatoric load was increased until the specimen failed. Following ASTM-D7012, the specimen was tested at a constant rate (3.3×10^{-6} m/s) so that specimen failed approximately 10–15 min into the testing [21–23]. During the test, the load frame recorded the axial position of the top piston. These data were used to derive the axial strain ($\mathbf{e_A}$) of the specimen.

Computed Tomography Scanning

Samples were scanned using a North Star Imaging M-5000 Industrial Computed Tomography (CT) scanner after triaxial compression tests. The samples were received at the National Energy Technology Laboratory submerged in the hydraulic oil that they were tested in, and they were not removed from the oil for scanning. Two-dimensional radiographs were captured with the Feinfocus FXE source at 185 kV and 200 mA, with 12 frames averaged for each radiograph. A 360-degree rotation of the sample was performed with 1440 images captured. These scans were reconstructed with North Star Imaging efX-CT® software and the resultant 3D images had a voxel resolution of (32.9 mm)^3. Image segmentation of the open voids and fractures from the cement matrix was performed using pixel segmentation with ilastik [24]. Further post-processing of the images and visualization was performed using ImageJ/FIJI [25]. Analysis of these images is ongoing.

Results

Scanning Electron Microscopy of Hydrated Cement

SEM imaging of hydrated cement polished surfaces was used to observe the microstructure and to view where and how the proposed enhancing materials behaved within the cement matrix.

In graphene cement, the platelets are seen within pore spaces and crevices, protruding from the pore walls. The clusters of platelets appear to be broken up into mono or multilayered platelets during the slurry mixing or hydration process. Figure 1 shows graphene in a micropore, occupying the space in a variety of orientations to strengthen the weakest points in the cement matrix.

For ferrierite cement, hollow ferrierite crystals were observed and identified within the cement matrix using EDS showing the elemental composition (Fig. 2).

Figure 3 shows an open-faced crystal from cutting and polishing the sample. In higher magnification, the crystal appears intact after a surface mechanical test from

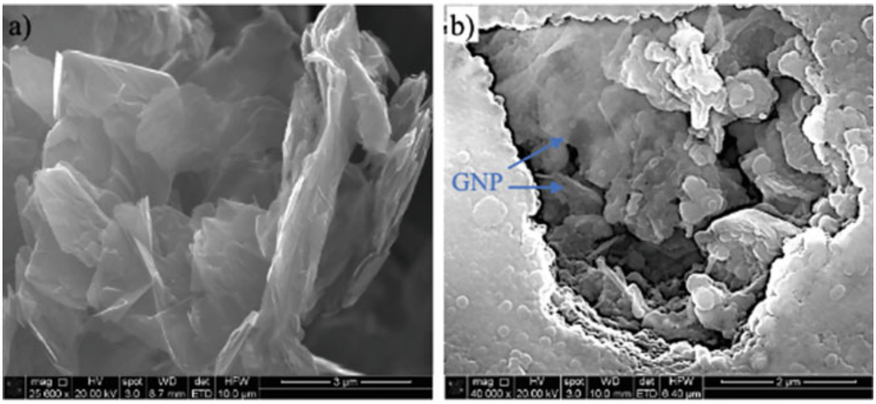

Fig. 1 **a** As-received graphene nanoplatelets imaged before adding to cement. Mono- and multi-layered platelets stack and cluster together. **b** Graphene nanoplatelets observed within micro- and nanopore space of cement

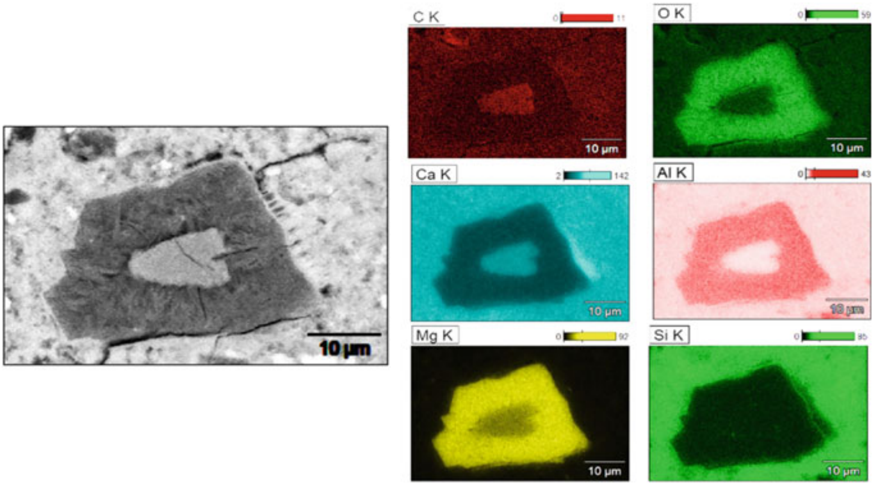

Fig. 2 EDS maps of cement matrix showing area rich in alumino silicate mineral (Zeolite) confirming its presence in cement matrix. High magnification at the grain boundaries needs to be conducted to understand the exact interaction of zeolite with cement

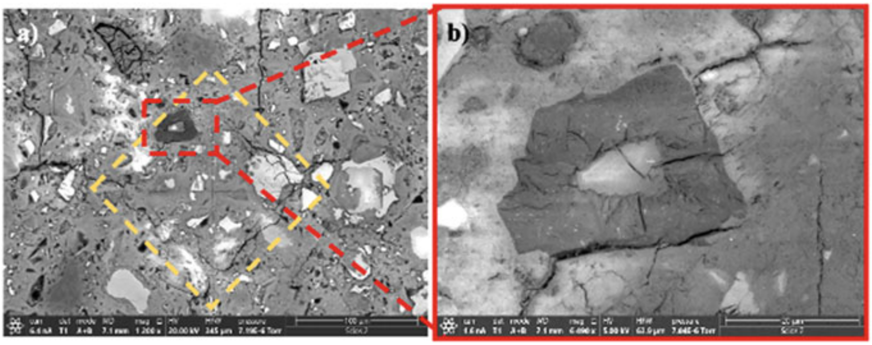

Fig. 3 **a** Scanning electron micrograph of a single indent done by the indenter on 5% FER added sample at 1200 × magnification containing ferrierite. **b** SEM image showing the FER crystal at a magnification of ~ 6500 × next to the indenter mark highlighting failure of cement on indentation with the fracture diverting around the ferrierite crystal and could be an indication of how the overall strength is enhanced in the cement at the macroscale

indentation had been conducted with the cement matrix fracturing around the crystal rather than breaking through it.

Ultimate Axial Stress in Triaxial Compression Test

To observe how the enhanced cements will perform in their downhole application, various percentages of each additive in cement were mechanically tested, simulating downhole pressure and temperature. For graphene, increasing the graphene content showed an increasing axial strength with the highest in 0.05%. It was also observed that GNP cement had a reduced brittle failure even after passing the maximum stress, indicated by a sharp reduction in axial stress. The highest axial stress of all samples was seen in 5% ferrierite, with a decreasing maximum stress with further increasing the ferrierite percentage. The same trend was observed for the olivine cement, with the 5% olivine sample having the highest ultimate axial stress.

Discussion

The addition of three different additives increases the strength of the cement sample at various levels but the mechanism by which this is accomplished is not completely resolved and the optimal additives percentages are still required the detailed studies. However, the transition from brittle to a stronger and more resilient cement in the triaxial loading test is the most likely the result of mechanisms by positioning of strong GNPs in micropores, bridging of fractures, as well as weak van der Waals forces between platelets allowing them to slide over one another Berman et al. [26]. All of these enable graphene to act as nano springs within the cement matrix which led to reducing the brittle failure behavior (Fig. 4). In our samples, we observed thin layers of received graphene stacked together under SEM images. Imaging of graphene

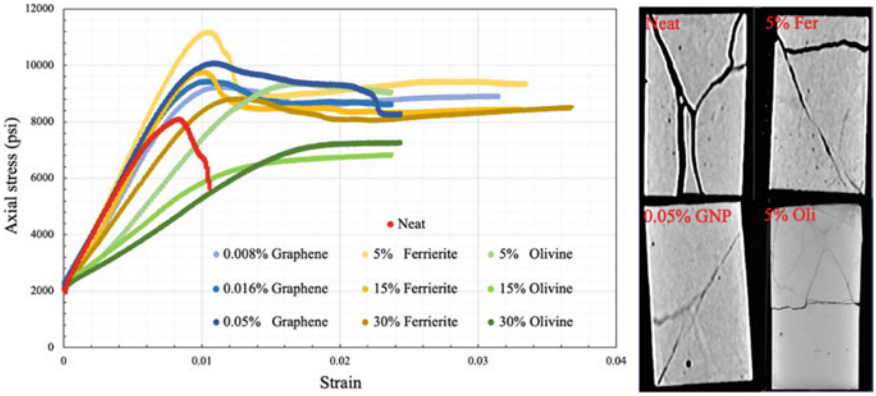

Fig. 4 Axial stress–strain curve of neat, graphene, and ferrierite cement at simulated wellbore conditions of 13.7 MPa confining pressure and 90 °C. Neat cement (red) shows a lower failure strength compared to graphene cement (blue) and ferrierite (yellow) and olivine (green). Post-failure CT scans are taken to view the fracture network of for each cement type (right)

mixed with the cement indicated that most of the graphene is distributed within the pore spaces or weakest parts of the material (Fig. 1), which alters the fracture initiation and propagation during mechanical stress and thus altering the failure behavior. In addition, all ferrierite cement samples showed improved strength with 5% having the greatest ultimate stress for all the samples tested. This possibly achieved by the hollow needle crystals of the ferrierite that are imbedded throughout the cement matrix. Olivine added showed to have reduced the cement brittleness with greater percentages added, but with only 5% resulting in withstanding a higher stress than the baseline of neat cement. The addition of these three additives shows encouraging results to improve the mechanical properties of cement with other potential benefits of reducing fracture propagations, leakage, and chemical attack.

Conclusion

From this study, the following conclusions were made for the performance of wellbore cement with the addition of graphene nanoplatelets, micronized ferrierite, and micronized olivine to mitigate the risks of well leakage:

- Graphene nanoplatelets were identified within the walls of the pore structure to reinforce weak points in the cement.
- Ferrierite crystals were observed to strengthen the cement microstructure.
- All cases of cement enhancement resulted in increased ultimate stress compared to neat cement when mechanically loaded at simulated downhole conditions of 13.7 MPa and 90 °C.
- The addition of GNPs in 0.05% or less resulted in an increased ultimate stress of 12–25% when tested at simulating conditions.
- All percentages of GNPs reduced the abrupt brittle failure seen in neat cement.
- 5% ferrierite and 5% olivine cement resulted in the highest ultimate strength of all samples.

Acknowledgements This research is supported by the National Academy of Science and Mathematics Gulf Research Program (NASEM-GRP) grant# 10002358 and the Project Research Team Members: Raissa Ferron group from University of Texas Austin, Ipsita Gupta group from Louisiana State University and Pierre Cerasi from SINTEF. A special thanks to Daniel Bour of Bour Consulting for bringing this study of graphene addition to cement to our attention as well as providing support and feedback. We thank Paul Beasant of Nova graphene for providing graphene. Gratitude goes to Halliburton for providing Class-H cement, D-air 5000, and CFR-3 dispersant. We appreciate the support from Lisa Whitworth and Brent Johnson at Oklahoma State University Microscopy Laboratory. Thank you, Tatiana Pyatina at Brookhaven National Laboratory, for your helpful observations. Special thanks to George King for valuable technical feedback of research and its relevance to field application. Gracious thanks to Mercy Achang for guidance and assistance. And last but not the least, we are grateful to our Hydraulic Barriers Team at OSU as well as the postdoc scholar and graduate students from NASEM GRP funded project: Mercy Achang (OSU), Vamsi Vissa (OSU), Tamitope Ajayi (LSU), Farzana Rahman (UTA), and especially Hope Asala, who is no longer with us due to a tragic accident.

References

1. Groom N (2020) Special report: millions of abandoned oil wells are leaking methane, a climate menace. Reuters, Thomson Reuters, 16 June 2020, 6:14 AM. www.reuters.com/article/us-usa-drilling-abandoned-specialreport-idUSKBN23N1NL
2. Alvarez RA, Zavala-Araiza D, Lyon DR, Allen DT, Barkley ZR, Brandt AR, Davis KJ, Herndon SC, Jacob DJ, Karion A (2018) Assessment of methane emissions from the US oil and gas supply chain. Science 361(6398):186–188
3. Gorchov Negron AM, Kort EA, Conley SA, Smith ML (2020) Airborne assessment of methane emissions from offshore platforms in the US Gulf of Mexico. Environ Sci Technol 54(8):5112–5120
4. Nelson EB, Guillot D (2006) Well cementing. Schlumberger, Sugar Land, TX
5. Petty S, Gastineau J, Bour DL, Ravi K (2003) Life cycle modeling of wellbore cement systems used for enhanced geothermal system development. In: 28th workshop on geothermal reservoir engineering, Stanford U, 27–29 Jan 2003 (Citeseer)
6. Vrålstad T, Saasen A, Fjær E, Øia T, Ytrehus JD, Khalifeh M (2019) Plug & abandonment of offshore wells: ensuring long-term well integrity and cost-efficiency. J Petrol Sci Eng 173:478–491
7. Katende A, Lu Y, Bunger A, Radonjic M (2020) Experimental quantification of the effect of oil based drilling fluid contamination on properties of wellbore cement. J Nat Gas Sci Eng 79, 103328
8. Horst DJ, Duvoisin CA, Vieira DAR (2018) An overview on properties, production mechanisms and applications of graphene. Int J Eng Trends Technol 61:156–160
9. Massion C, Lu Y, Bunger A, Crandall D, Achang M, Radonjic M (2021) Improvement of wellbore cement by addition of graphene nanoplatelets. Geotherm Res Coun 45:236
10. Mohan VB, Lau K-T, Hui D, Bhattacharyya D (2018) Graphene-based materials and their composites: a review on production, applications and product limitations. Compos B Eng 142:200–220
11. Massion C, Radonjic M, Lu Y, Bunger A, Crandall D (2021) Impact of graphene and the testing conditions on the wellbore cement mechanical and microstructural properties. Paper presented at the 55th US rock mechanics/geomechanics symposium, Virtual, June 2021, paper number: 2021–2089
12. Snellings R, Mertens G, Cizer Ö, Elsen J (2010) Early age hydration and pozzolanic reaction in natural zeolite blended cements: reaction kinetics and products by in situ synchrotron X-ray powder diffraction. Cem Concr Res 40(12):1704–1713
13. Jana D (2007) A new look to an old pozzolan, clinoptilolite–a promising pozzolan in concrete. In: Proceedings of the 29th ICMA conference on cement microscopy, Curran Associates Inc Quebec City
14. Uzal B, Turanlı L, Yücel H, Göncüoğlu MC, Çulfaz A (2010) Pozzolanic activity of clinoptilolite: a comparative study with silica fume, fly ash and a non-zeolitic natural pozzolan. Cem Concr Res 40(3):398–404
15. Vissa SVK, Lu Y, Bunger A, Crandall D, Radonjic M (2021) Natural zeolite cement blend for geothermal wellbore applications: the zeolite mechanism in making resilient cement formulations. Geoth Res Coun 45:236
16. Yılmaz B, Uçar A, Öteyaka B, Uz V (2007) Properties of zeolitic tuff (clinoptilolite) blended Portland cement. Build Environ 42(11):3808–3815
17. Pyatina T, Sugama T, Ronne A, Trabits G (2018) Self-repairing properties of OPC clinker/natural zeolite blend in water and alkali carbonate environments at 270 °C. Adv Cem Res 30(1):8–23
18. Achang M, Radonjic M (2021) Adding olivine micro particles to Portland cement based wellbore cement slurry as a sacrificial material: A quest for the solution in mitigating corrosion of wellbore cement. Cement Conc Compos (121):104078

19. Lu Y, Spencer-Williams I, Chang-Frizzell N, Bunger A (2020) Evidence for self-healing of carbonated olivine for wellbore cementing and plugging under high temperature high pressure (HTHP) reservoir conditions. Geother Res Coun Trans 44 (153):58–66. Proceedings of geothermal research council annual meeting & expo, 18–23 Oct 2020, Reno, Nevada
20. Lu Y, Radonjic M, Crandall D, Bunger A (2021) Evidence for self-restoration of olivine based cement under geothermal conditions: olivine micro-aggregate as mitigation to portland cement acidic attack. Geother Res Coun Trans 44(186). Geothermal Rising Conference (GRC), San Diego, CA, 3 Oct 2021
21. API RP-10B, Recommended Practice for Testing Well Cements, 22nd, Washington, DC: API, 2
22. ASTM (2010) Standard test method for compressive strength and elastic moduli of intact rock core specimens under varying states of stress and temperatures, ASTM International
23. ASTM (2014) Standard test method for static modulus of elasticity and poisson's ratio of concrete in compression (ASTM C469/C469M-14). American Society for Testing and Materials West Conshohocken
24. Berg Kutra SD, Kroeger T, Straehle CN, Kausler BX, Haubold C, Schiegg M, Ales J, Beier T, Rudy M, Eren K (2019) Ilastik: interactive machine learning for (bio) image analysis. Nat Methods 16:1226–1232
25. Schindelin J, Arganda-Carreras I, Frise E, Kaynig V, Longair M, Pietzsch T, Preibisch S, Rueden C, Saalfeld S, Schmid B, Tinevez JY (2012) Fiji: an open-source platform for biological-image analysis. Nat Methods 9:676-682
26. Berman D, Erdemir A, Sumant AV (2014) Graphene: a new emerging lubricant. Mater Today 17:31–42

Solidification of Salt Hydrate Eutectics Using Multiple Nucleation Agents

Sophia Ahmed, Robert Mach, Haley Jones, Fabiola Alamo, and Patrick J. Shamberger

Abstract Salt hydrates are a class of phase-change materials (PCMs) capable of storing thermal energy at a high volumetric energy density for a low cost (<\$10/kWh$_{th}$), making them of interest for improving the energy efficiency of buildings and displacing peak load associated with environmental control systems. However, select salt hydrates are susceptible to irreversible degradation associated with phase segregation, and to undercooling—the occurrence of a metastable liquid below the melting point due to a lack of nucleation sites for the crystalline solid. Here, we present a study of phase-specific epitaxial nucleation agents which mitigate undercooling in eutectic nitrate salt hydrate systems. While eutectics can depress melting temperatures into favorable ranges, metastable eutectics experience undercooling. We demonstrate that the nucleation of multiple phases in systems which are susceptible to undercooling can increase the potential for phase segregation and chemical stratification to occur. Furthermore, we illustrate the utility of multiple nucleation agents in these systems to co-crystallize multiple crystalline phases.

Keywords Salt hydrates · Solidification · Thermal energy storage · Eutectic · Phase segregation · Thermophysical properties

Introduction

Phase-change materials (PCMs) are a class of materials that absorb and release a large amount of heat during reversible phase transformations and are great for thermal energy storage (TES) applications. Thus, PCMs offer an approach to (1) buffer transient temperature rises in pulsed power electronics [1], automotive [2], and aerospace systems [3], with minimal additional mass and volume to a system, or (2) to displace load on environmental control systems for buildings, allowing for shifting of load demand on the power grid, and ultimately, improving the penetration or intermittent renewable power sources. Salt hydrates are a class of inorganic PCMs

---

S. Ahmed (✉) · R. Mach · H. Jones · F. Alamo · P. J. Shamberger
Texas A&M University, 3003 TAMU, College Station, TX 77843, USA
e-mail: ahmed.sophia97@tamu.edu

F. Tesfaye et al. (eds.), *REWAS 2022: Energy Technologies and CO$_2$ Management (Volume II)*, The Minerals, Metals & Materials Series,
https://doi.org/10.1007/978-3-030-92559-8_14

of particular interest due to their high volumetric energy density, moderate thermal conductivity, and low cost [4]. Furthermore, stoichiometric salt hydrate and anhydrous salt endmembers can be combined to form a large number of eutectic systems, allowing for fine control of the melting temperature of the material, and affording an approach to develop customized PCMs for particular applications. Despite this potential, salt hydrates are subject to two principal limitations: (1) phase segregation can potentially result in irreversible changes to the melting behavior with cycling and (2) nucleation limitations in salt hydrate systems can require additional undercooling prior to the onset of solidification on cooling. The confounding effects of phase segregation and undercooling on the stability of salt hydrate eutectics is poorly understood.

Phase segregation refers to the physical separation of liquid and solid phases due to buoyancy-driven processes and tends to occur during periods in which both solid and liquid phases coexist (i.e., during solidification and melting processes). Thus, phase segregation is associated with repeated cycling of a PCM between solid and liquid states. Phase segregation is problematic, in that it has the potential to result in chemical stratification, or compositional inhomogeneity within the system, *when the phases that segregate have dissimilar compositions*. Compositional inhomogeneity can cause the overall melting behavior of a volume to change, as thermal equilibrium is achieved at different temperatures within different portions of the volume. This situation occurs in some salt hydrate systems, most notably sodium sulfate decahydrate (Glauber's salt) [5], but is not an intrinsic property of all salt hydrates. Several approaches have been taken to avoid issues associated with phase segregation, most notably including the use of additives which increase the viscosity of a PCM, or form a viscoelastic gel, thereby limiting the separation of phases in the phase segregation process [6]. Despite these attempts, in systems that are thermodynamically predisposed to phase segregate, degradation of properties with cycling can be delayed, but generally not entirely avoided [7].

In addition, salt hydrates are susceptible to undercooling, which refers to a phenomenon where a material does not solidify at the equilibrium melting temperature, but rather requires additional cooling before a solid phase nucleates. Undercooling results from a nucleation-limited process, in which substantial energetic barriers to nucleation limit the initiation of solidification. To overcome undercooling, additional solid phases may be introduced into a system, which are selected due to their tendency to nucleate the solid phase of interest [8]. One of the principal approaches to identify active nucleation agents is the use of materials with epitaxial relationships with the PCM phase that is solidifying; this approach affords a convenient approach to identifying candidate phases and has shown broad utility across multiple classes of materials. Nucleation agents with epitaxial relationships have been demonstrated in different classes of PCMs (e.g., the addition of borax to sodium sulfate decahydrate [5]), as well as in the processing of polymers (e.g., the addition of talc to PET [9]) and metals (e.g., seeding during casting of metals [10]).

In this publication we assess the potential impact of phase segregation, together in concert with metastable solidification, to result in changes in the melting behavior of eutectic systems. It has previously been noted that eutectics, due to their tendency to solidify multiple solid phases simultaneously and often in an inseparable interpenetrating manner, are robust to issues associated with phase segregation. However, this claim neglects the potential impact of metastable solidification. Here, we assess the issue from a rigorous consideration of solidification behavior and phase relationships and illustrate with examples from different salt hydrate eutectic systems. We demonstrate that metastable solidification can result in chemical segregation and degradation of melting properties and assess the use of multiple nucleation agents to help mitigate this issue.

Solidification in Multi-component Salt Hydrate Systems

As a salt hydrate solidifies or melts, different solidification reactions can occur depending on the composition of the system and the characteristics of the phase diagram (Table 1). In all cases, coexistence of a liquid phase and one or more solid phases can potentially result in phase segregation, as solid phases generally have dissimilar densities from the liquid brine phase. However, the primary mechanism which results in degradation of the thermophysical properties of a PCM is not the phase segregation process itself, but rather the tendency for phase segregation to result in chemical stratification. Furthermore, this chemical stratification can be exacerbated by the formation of additional metastable phases which are very weakly soluble in water (e.g., lower hydrates of the salt), but which do not undergo the desired phase transition process at the invariant reaction temperature. Thus, the tendency for phase segregation to result in irreversible changes to the melting and solidification behavior in a PCM depends on (1) the tendency for phase segregation to result in compositional stratification and (2) the potential for additional metastable phases to form that don't readily revert to stable phases above or below the transition temperature. Three main types of melting/solidification reactions have been considered for potential use as PCMs, and are discussed here: congruent melting, eutectic melting, and incongruent melting (Fig. 2). The relative behavior of these three systems is described below.

Table 1 Comparison of various types of melting reactions that can occur in salt hydrate systems

Type of melting reaction	Example (Fig. 2)	Reaction	Type of Eutectic composition	Phase Segr. possible?	Compositional strat. possible?
Congruent	C	$L \leftrightarrow \beta$		Yes	No. $X_\beta = X_{Liq}$
Eutectic	E_1	$L \leftrightarrow \beta + \gamma$	Equilibrium	Yes	No. $X_{eutsol.} = X_{\beta+\gamma} = X_{Liq}$
	E_2	$L \leftrightarrow \beta(+\gamma)$	Metastable	Yes	Yes. $X_{sol.} = X_\beta \neq X_{Liq}$
Incongruent (peritectic)	I	$L + \delta \leftrightarrow \gamma$		Yes	Yes. $X_\gamma \neq X_\delta \neq X_{Liq}$

Congruent solidification occurs when the liquid phase transforms into a single solid phase at an invariant temperature, where the solid phase and the liquid have the same compositions (e.g., $L \leftrightarrow \beta$, Fig. 2, point C) [7]. In this case, during melting or during solidifying, phase segregation may occur, due to buoyancy differences between the two coexisting phases (L, β). However, as these two phases have the same chemical composition, phase segregation cannot result in compositional stratification (Fig. 2). Furthermore, in a congruent reaction, there is no tendency for additional metastable phases to form. Thus, materials which exhibit congruent melting reactions are robust over large numbers of cycles and exhibit no change in melting/solidification behavior as a result of phase segregation. It is worth stressing that, while phase segregation still occurs in these cases, it does not generally impact the reversibility of the system. One example of a congruently melting PCM, lithium nitrate trihydrate ($LiNO_3·3(H_2O)$) melts congruently at 30.1 °C [11]. While solid $LiNO_3·3(H_2O)$ has a greater density than the liquid phase, and therefore phase segregation may occur, chemical stratification will not result. Thus, this reaction is stable over hundreds of cycles with no measurable change in melting behavior [12]. Other examples of phases of interest in salt hydrates which exhibit congruent melting include zinc nitrate hexahydrate, $Zn(NO_3)_2·6(H_2O)$ [13], and magnesium nitrate hexahydrate, $Mg(NO_3)_2·6(H_2O)$ [14].

Incongruent solidification occurs when a solid phase melts, producing a compositionally different liquid than the original solid. This occurs at a peritectic point, where the liquid phase and one solid phase together transforms to form a solid phase at an invariant temperature (e.g., $L + \delta \leftrightarrow \gamma$, Fig. 2, point I). Importantly, the liquid and the solid (δ) have different compositions in the region of phase coexistence above the peritectic point. Phase separation can occur with this reaction due to buoyancy differences between phases, and compositional inhomogeneity would result. This results in melting over a broader range of temperature, and in extreme cases will cause some portions of the volume to no longer melt. Additionally, if the solid (δ) is weakly soluble in water, its dissolution above the liquidus can be kinetically limited, resulting in some volume not participating in transformations during future cycles. One example of a salt hydrate that experiences incongruent solidification if brought to temperatures above its melting point of 31.9 °C is sodium sulfate decahydrate, $Na_2SO_4·10(H_2O)$ [15]. It undergoes a peritectic reaction as it incongruently solidifies, making it unstable for use throughout many cycles.

Eutectic solidification occurs when a liquid phase transforms to two or more solid phases at an invariant temperature and composition (e.g., $L \leftrightarrow \beta + \gamma$, Fig. 2, point E_2). In the case of a eutectic, the composition of the liquid is the same as the composition of the aggregate solid mass. Phase segregation may occur due to buoyancy differences as well as how the eutectic solidifies. In the case of equilibrium solidification, both solid phases crystallize simultaneously, often in an intimately interpenetrating fashion. In this case, the aggregate composition of the solid mass is the same as the composition of the liquid, and chemical inhomogeneities do not result (Fig. 1a). In the case of metastable solidification, one phase nucleates and begins solidifying, while the second phase is kinetically limited. This results in a liquid line of descent that moves away from the eutectic composition (Fig. 2, dashed

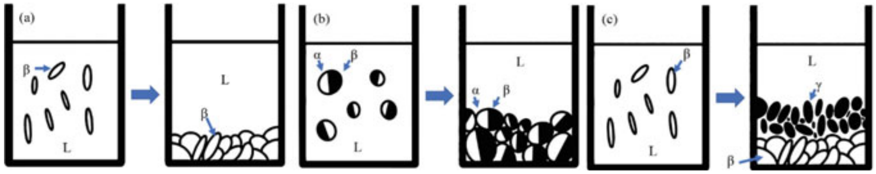

Fig. 1 α and β phases segregating from the liquid brine phase due to differences in density. Composition will be uniform as there is a lack of compositional stratification occurring. **a** Represents solidification, **b** eutectic solidification under equilibrium conditions, and **c** eutectic solidification with metastable solidification at one phase

line), and can result in compositional heterogeneities (Fig. 1c). Unlike incongruent melting, additional solid phases are not introduced at the eutectic reaction, and thus eutectics do not tend to be susceptible to formation of weakly soluble phases which no longer transform. An example of an equilibrium eutectic is the $LiNO_3$–$LiClO_4$–H_2O pseudobinary eutectic where it melts at a local minimum of 27 °C [16]. A metastable eutectic is studied with the $LiNO_3 \cdot 3(H_2O)$–$LiNO_3$–$NaNO_3$ system described below, which experiences a high degree of undercooling without the aid of nucleation agents.

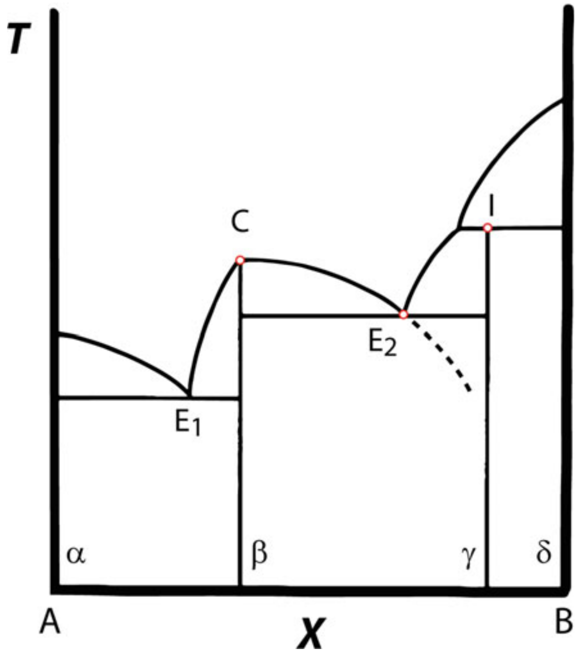

Fig. 2 Example phase diagram demonstrating congruent (C), eutectic (E_1, E_2), and incongruent melting (I) at a peritectic. The dashed line near E_2 represents the metastable extension for the liquidus of phase β below E_2. In the case where solidification of phase γ is kinetically limited at E_2, this line represents the change in the liquid composition with cooling. This is an original figure made for this publication by the authors

Case Study: $LiNO_3$–$NaNO_3$–H_2O Eutectic

$LiNO_3{\cdot}3(H_2O)$ has been identified as a salt hydrate of interest for near room-temperature heating and cooling applications because of its melting temperature of 30.1 °C and also its relatively large specific heat of fusion of 287 J/g [11]. The eutectic composition of binary and ternary systems based on $LiNO_3{\cdot}3(H_2O)$ has been predicted using a modified BET method [17, 18]. Based on these predictions, we synthesized the ternary eutectic in the system $LiNO_3$–$NaNO_3$–H_2O that corresponds with equilibrium solidification of the phases: $LiNO_3{\cdot}3(H_2O)$–$LiNO_3$–$NaNO_3$ (henceforth referred to as the LiNaW eutectic). Solidification behavior in this system was investigated through both DSC (Fig. 3), and by tracking the internal temperature of a 3 mL volume cooled and heated continuously (at 0.1–1 ºC/min) in a recirculating water bath (Fig. 4).

Nucleation agents were added to the solution to decrease the undercooling observed in the solidification of the LiNaW eutectic. Nucleation agents are materials which introduce low interfacial energy between the solid particle and the solidifying material, which serve as nucleation sites and therefore, reduce undercooling. The nucleation agents, zinc hydroxy nitrate hydrate, $Zn(OH)(NO_3){\cdot}H_2O$, and $Cu_3(NO_3)(OH)_5{\cdot}2(H_2O)$, otherwise known as the mineral likasite, have been demonstrated to reduce undercooling in $LiNO_3{\cdot}3(H_2O)$ systems down to 6.3 °C [19]. Here, we illustrate the solidification behavior of both the pure LiNaW eutectic and in the presence of the nucleation agent likasite, which reduces undercooling specifically in the solidification of $LiNO_3{\cdot}3(H_2O)$. In both cases, solidification is observed to occur in two distinct pulses, each associated with distinct exothermic peaks (Fig. 3). Addition of likasite decreases the primary undercooling, ΔT_1, which is defined as the temperature difference between the equilibrium melting temperature

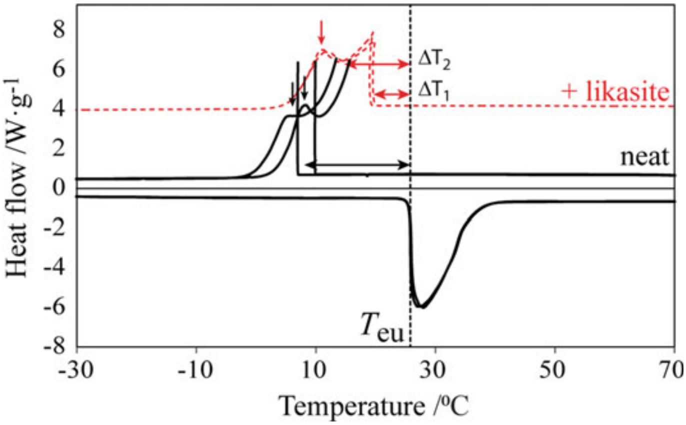

Fig. 3 DSC Curves of two cycles of neat $LiNO_3{\cdot}3(H_2O)$–$LiNO_3$–$NaNO_3$ and two cycles of the same neat $LiNO_3{\cdot}3(H_2O)$–$LiNO_3$–$NaNO_3$ including the nucleation agent likasite. In both cases, two distinct peaks are observed on cooling, suggesting that solidification occurs

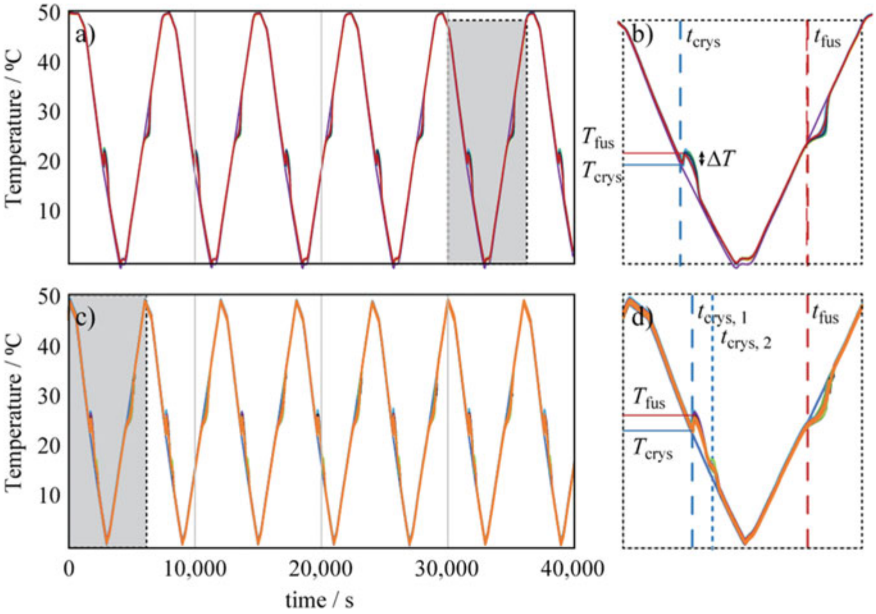

Fig. 4 Cycling of $LiNO_3{\cdot}3(H_2O)$–$LiNO_3$–$NaNO_3$ eutectic with likasite and $BaCO_3$, $CaCO_3$, and $SrSO_3$. **a** Features a more stressed system with cycling occurring at a higher temperature than (**c**). **b** and **d** are individual cycles of (**a**) and (**c**), respectively

and the onset of solidification. However, the impact of likasite on the temperature of the secondary solidification peak is relatively minor. This observation supports the observations that in systems which are subject to metastable nucleation-limited solidification, solidification of a eutectic does not necessarily result in simultaneous solidification of all equilibrium phases.

To determine the impact of metastability on the cycling behavior of the LiNaW eutectic, a larger volume (3 mL) was sealed in a stainless-steel tube and cycled for hundreds of cycles. Importantly, the system was intentionally stressed by cooling to progressively higher and higher minimum temperatures, to attempt to induce solidification of just one phase at the eutectic point, and therefore, push the system into a regime in which phase segregation can induce compositional heterogeneities (Fig. 4). Over a sufficiently large number of cycles under stressing conditions, melting is observed to occur over a larger range in temperature, and solidification is observed to occur at two distinct temperatures, suggesting that compositional heterogeneities have been induced within the solidifying volume, resulting in degradation of cycling behavior.

Conclusion

Degradation in thermal properties in PCMs due to phase segregation is a known challenge in incongruently melting systems. It is generally assumed that eutectic systems are robust to this issue, due to the tendency for all phases to co-solidify at equilibrium in a eutectic system. However, in the case where one or more phases are kinetically delayed, relative to other phase(s) solidifying at the eutectic, the opportunity exists for phase segregation to result in composition inhomogeneities within a volume, and for this to result in unstable behavior with cycling. We demonstrate these potential challenges in one candidate ternary eutectic system: $LiNO_3{\cdot}3(H_2O)$–$LiNO_3$–$NaNO_3$. Despite the inclusion of nucleation agents included expressly to decrease the magnitude of undercooling, the system illustrates solidification of different phases at different temperatures on cooling, and furthermore, after cycles which are intentionally designed to push the system into a metastable solidification regime, melting behavior changes with progressive cycling, and the system no longer exhibits a single well-defined solidification or melting temperature. Thus, phase segregation can still represent a technical limitation in at least some eutectic systems. Further exploration of this phenomena is required to assess how general or specific of a case the illustrated case represents, as well as approaches to best mitigate the issue for technological applications.

References

1. de Bock HP et al (2020) A system to package perspective on transient thermal management of electronics. J Electr Pack 142(4). https://doi.org/10.1115/1.4047474
2. Kim K-B, Choi K-W, Kim Y-J, Lee K-H, Lee K-S (2010) Feasibility study on a novel cooling technique using a phase change material in an automotive engine. Energy 35(1):478–484, 2010/01/01/. https://doi.org/10.1016/j.energy.2009.10.015
3. Mulligan JC, Colvin DP, Bryant YG (1996) Microencapsulated phase-change material suspensions for heat transfer in spacecraft thermal systems. J Spacecr Rocket 33(2):278–284. https://doi.org/10.2514/3.26753
4. Lorsch HG, Kauffman KW, Denton JC (1975) Thermal energy storage for solar heating and off-peak air conditioning. Energy Conv 15(1–2):1–8
5. García-Romero A, Diarce G, Ibarretxe J, Urresti A, Sala JM (2012) Influence of the experimental conditions on the subcooling of Glauber's salt when used as PCM. Solar Energy Mater Solar Cells 102:189–195. 2012/07/01/ 2012. https://doi.org/10.1016/j.solmat.2012.03.003
6. Royon L, Karim L, Bontemps A (2013) Thermal energy storage and release of a new component with PCM for integration in floors for thermal management of buildings. Energy Build 63:29–35, 2013/08/01/ 2013. https://doi.org/10.1016/j.enbuild.2013.03.042
7. Lane GA, Shamsundar N (1983) Solar heat storage: Latent heat materials, vol. I: background and Scientific Principles. J SolEnergy Eng 105(4):467–467. https://doi.org/10.1115/1.3266412
8. Vonnegut B (1947) The Nucleation of ICE formation by Silver Iodide. J Appl Phys 18(7):593–595. https://doi.org/10.1063/1.1697813
9. Haubruge HG, Daussin R, Jonas AM, Legras R, Wittmann JC, Lotz B (2003) Epitaxial Nucleation of Poly(ethylene terephthalate) by Talc: Structure at the Lattice and Lamellar Scales. Macromolecules 36(12):4452–4456, 2003/06/01. https://doi.org/10.1021/ma0341723

10. Xing LQ, Chen B (1995) Phase-seeded solidification of undercooled Ni-B-Si alloy. J Mater Sci Lett 14(7): 480–482, 1995/01/01. https://doi.org/10.1007/BF00665908
11. Shamberger PJ, Reid T (2012) Thermophysical properties of Lithium Nitrate Trihydrate from (253 to 353) K. J Chem Eng Data 57(5): 1404–1411, 2012/05/10 2012. https://doi.org/10.1021/je3000469
12. Tamraparni A, Shamberger PJ, Felts JR (2020) Cyclic stability of lithium nitrate trihydrate in plate fin heat exchangers. Appl Therm Eng 179:115476, 2020/10/01/ 2020. https://doi.org/10.1016/j.applthermaleng.2020.115476
13. Sieverts A, Petzold W (1933) Binäre Systeme: Nitrate von Metallen der zweiten Gruppe des periodischen Systems und Wasser. II. $Be(NO_3)_2–H_2O$, $Zn(NO_3)_2–H_2O$ und $Cd(NO_3)_2–H_2O$. Z Anorg Allg Chem 212(1):49–60. https://doi.org/10.1002/zaac.19332120108
14. Sieverts A, Petzold W (1932) Binäre Systeme: Nitrate von Metallen der zweiten Gruppe des periodischen Systems und Wasser. I. $Mg(NO_3)_2–H_2O$. Z Anorg Allg Chem 205(1–2):113–126. https://doi.org/10.1002/zaac.19322050110
15. Carlsson B, Stymne H, Wettermark G (1979) An incongruent heat-of-fusion system—$CaCl_2·6H_2O$—Made congruent through modification of the chemical composition of the system. Solar Energy 23(4), 343–350, 1979/01/01/ 1979. https://doi.org/10.1016/0038-092X(79)90129-4
16. Lovera-Copa JA, Ushak S, Reinaga N, Villalobos I, Martínez FR (2020) Design of phase change materials based on salt hydrates for thermal energy storage in a range of 4–40 °C. J Thermal Anal Calorim 139(6):3701–3710, 2020/03/01 2020. https://doi.org/10.1007/s10973-019-08655-1
17. Zeng D, Voigt W (2003) Phase diagram calculation of molten salt hydrates using the modified BET equation. Calphad-Comput Coupl Phase Diag Thermochem 27:243–251
18. Stokes RH, Robinson RA (1948) Ionic hydration and activity in electrolyte solutions. J Am Chem Soc 70(5):1870–1878
19. Shamberger PJ, O'Malley MJ (2015) Heterogeneous nucleation of thermal storage material $LiNO_3·3H_2O$ from stable lattice-matched nucleation catalysts. Acta Mater 84: 265–274, 2015/02/01/ 2015. https://doi.org/10.1016/j.actamat.2014.10.051

Thermoeconomics and Dynamics of Orange Hydrogen Production, an Energy Matter

Neale R. Neelameggham, Ganesan Subramanian, and Praveen Kalamegham

Abstract Multiple reports exist on the range of cost of production of hydrogen from about \$1.20/kg to about \$12.00/kg. Hydrogen exists mainly as part of compounds and the elemental hydrogen has to be produced from these compounds and/or mixtures of compounds by spending energy. A detailed thermodynamic analysis revealed that this spectrum of costs exist primarily from the energy conversion costs and economics of such energy conversions. This analysis leads to the simple low-cost possibilities of hydrogen from hydrocarbons called 'orange' hydrogen, which is CO_2-free, along with the ease of making it from the ground using present-day renewable energy as needed.

Keywords Thermoeconomic-dynamics · Orange hydrogen · Energy efficient hydrogen · METZERO

Extended Abstract

Multiple reports exist on the range of cost of production of hydrogen from about \$1.20/kg to about \$12.00/kg. Hydrogen exists mainly as part of compounds and the elemental hydrogen has to be produced from these compounds and/or mixtures of compounds by spending energy. A detailed thermodynamic analysis revealed that this spectrum of costs exist primarily from the energy conversion costs and economics of such energy conversions. This analysis leads to the simple low-cost possibilities of hydrogen from hydrocarbons called 'orange' hydrogen, which is CO_2-free, along with the ease of making it from the ground using present-day renewable energy as needed.

N. R. Neelameggham (✉)
Ind LLC, South Jordan, UT, USA

G. Subramanian
Sai Systems, Houston, TX, USA

P. Kalamegham
Ind LLC, Austin, TX, USA

F. Tesfaye et al. (eds.), *REWAS 2022: Energy Technologies and CO_2 Management (Volume II)*, The Minerals, Metals & Materials Series,
https://doi.org/10.1007/978-3-030-92559-8_15

The basis of 'Energy Technology and Carbon Dioxide Management' is energy efficiency and manage of CO_2 in a gainful manner or avoid formation of CO_2, using Energy Conservation law, Thermodynamic Equilibrium principles, and most of all noting that it costs money to convert matter or energy from one form to another. Waste thermal energy causes Global Anthropogenic warming, as atmospheric air mass is a finite known constrained quantity [1, 2].

Orange H_2 is a pragmatic path to a carbon neutral future, based on sound *thermoeconomics and dynamic*s. Orange Hydrogen is a low-cost, energy-efficient, easily instrumented, chemical process that breaks down traditional hydrocarbon and biofuels (e.g., crude oil, natural gas, gasoline, biogas, etc.) into hydrogen with no carbon dioxide byproduct [3]. While other solutions to produce H_2 exist, such as Blue Hydrogen and Green Hydrogen, Orange Hydrogen is superior because: no CO_2 byproduct, portable implementation, minimal energy requirements, it provides byproduct battery graphite, carbon nanotubes, ink grade or other specialty carbons. In the net zero emissions 2050 world, Orange Hydrogen will play an important role. It is necessary to understand all forms of hydrogen production to appreciate the benefits of Orange Hydrogen. Most important is to note that the activation energy and the process heat can all be supplied to these using present day renewable electricity—similar to what can be applied to water electrolysis.

Our comprehensive study of multiple ways of making hydrogen, simple schematic shown in Fig. 1, and in little more details are shown in three technical pagelets which can be seen from the Orange Hydrogen website courtesy of Ind LLC [3], with follow-up notes. Pagelet 1 describes a look at many colors of hydrogen with the described thermochemistry model Table in Pagelet 2 following Hess's Laws of component additivity [4]. The thermoeconomic dynamics of different colors of hydrogen are summarized in Pagelet 3 along with estimates of cost of hydrogen production and CO_2 to sequester. There are limited amounts of native hydrogen found worldwide. The thermochemistry table highlights the free energy of formation of several naturally found compounds from which hydrogen is typically produced—such as water, H_2O, hydrocarbons, HC, and hydrogen sulfide, H_2S. Higher negative value for the compound's free energy of formation means, the reversal into its elements will be a higher positive value for the free energy of reaction of splitting, and the reaction

Hydrogen Production is mostly from Compounds HpXq

X in natural hydrogen compounds are usually C, S and O - others are usually man-made

Chemical Equation: HpXq = p/2 H2 + q X

Thermodynamic Energy Required = - [Free Energy of Formation of Compound HpXq]

[Thermoeconomics] Economic Equation: Production Cost = Raw material + Energy + Labor

Fig. 1 Schematic of Hydrogen production Thermoeconomics Dynamics is endothermic. The compound is in a stable form with higher negative free energy of formation. In addition to providing, the endothermic energy, one has to supply activation energy to initiate the reaction. All hydrocarbons are alloys of hydrogen and carbon, they have different element to element bonds with distinct bond energies. We will not go into that—here we follow simple Hess's Law principle in our discussions.

The presentation discuss historic costs of different ways of making hydrogen and have found that time and again the highest cost method is mainly due to highest cost of energy to convert the compound of hydrogen, mainly due to thermodynamic constraint of highest energy required. This has not changed in 130 years of industrial hydrogen production including using renewable energy. Water electrolysis costs are the highest as one has to split the most stable compound H_2O unlike less stable and meta-stable hydrocarbons. Thermodynamic energy required decreases in the order of splitting water > splitting hydrocarbons with water or an oxidant > splitting hydrocarbons into other hydrocarbons, hydrogen, and carbon. Sustainable production will come from processes which consume less energy, *near zero effluents* of matter and energy following METZERO principles.

Pyrolysis of hydrocarbons containing more than one carbon atom with their metastable positive free energy of formation is anticipated to take the lead in future hydrogen production along with co-products and near zero wastes. More references are shown about work done in this field, including novel approaches using adiabatic thermodynamic principles of compression expansion work during chemical splitting, which are usable in storage of renewable energy which are of intermittent nature [5–10]. Another method with minimal follow-up work is the protolytic decomposition of n-octane near room temperature. [11]. Variations of these approaches may be applicable in extracting the stored energy in the alloys of carbon and hydrogen. It is also possible to make bio-hydrogen from natural carbon–hydrogen crude oils by applying principles studied in biodegradation of paraffins [12]. It is of value to read the recent article on uncovering the true cost of hydrogen by a lifecycle monetisation approach which includes besides the operating costs, the monetized costs of environmental impacts on human health, ecosystem quality, and resources [13].

The overall costs of raw material, its energy content, and energy costs of conversion dictates the economics, and the energy costs of conversion is dictated by thermodynamics. Once the world and industry realize the basic thermoeconomics and dynamics we may find more applications of the silent 'orange hydrogen' which has been produced and used for over a century. Economic stability also follow thermodynamic stability and minimization of entropy increases.

References

1. Neelameggham N, Davis B (2015) 21st century global anthropogenic convective model. J. Nanomater Energy. https://doi.org/10.1680/jnaen.15.00014

2. Subramanian G, Neelameggham NR (2017) Modeling anthropogenic heat flux in climate models. In: Zhang L et al (eds) Energy technology 2017. The minerals, metals & materials series. Springer, Cham. https://doi.org/10.1007/978-3-319-52192-3_6
3. Orange Hydrogen Website (2021). https://indllc.wixsite.com/orangeh2. Accessed 2 Aug 2021
4. Hess's Law—Chemistry LibreTexts (2021). https://chem.libretexts.org. Accessed 28 Aug 2021
5. Pasquali M, Mesters C (2021) We can use carbon to decarbonize—and get hydrogen for free. https://www.pnas.org/content/118/31/e2112089118#comment-5490160212. Accessed 15 Aug 2021
6. Labanca A, Silva C, Sacorague L (2020) Atmospheric plasma for carbon nanotubes production. Int J Astronaut Aeronautical Eng 5:042 ISSN: 2631–5009
7. Muradov N (2004) Final report—thermocatalytic CO_2-free production of hydrogen from hydrocarbon fuels, DOE contract No DE-FC36–99GO10456, 1999–2003. Jan
8. Atakan B (2019) Compression-Expansion processes for chemical energy storage: thermodynamic optimization for methane. Ethane Hydrogen Energies 12:3332. https://doi.org/10.3390/en12173332,www.mdpi.com/journal/energies
9. Rudolph C, Atakan B (2021) Pyrolysis of methane and ethane in a compression–expansion process as a new concept for chemical energy storage: a kinetic and exergetic investigation. Energy Technol 2000948. https://doi.org/10.1002/ente.202000948
10. Drost S, Schießl R, Maas U (2019) Feasibility of natural gas pyrolysis for production of unsaturated hydrocarbons: an RCM study. In: Proceedings of the 27th international colloquium on the dynamics of explosions and reactive systems. http://www.icders.org/ICDERS2019/abstracts/ICDERS2019-257.pdf
11. Kawashima Y, Iwamoto M (2016) Protolytic decomposition of n-octane on graphite at near room temperature Sci Rep 6, Article number: 28493
12. Adlan NA, Sabri S, Masomian M, Mohamad Ali MS, Zaliha Raja Abd Rahman (2020) Microbial biodegradation of paraffin wax in malaysian crude oil mediated by degradative enzymes, frontiers in microbiology, Sep 2020, vol 11, Article 565608
13. Al-Qahtani A, Parkinson B, Hellgardt K, Shah N, Guillen-Gosalbez G (2020) Uncovering the true cost of hydrogen production routes using life cycle monetization. https://doi.org/10.1016/j.apenergy.2020.115958

Power to Hydrogen: The Prospects of Green Hydrogen Production Potential in Africa

Nour Abou Seada and Tarek M. Hatem

Abstract Africa is rich with an abundance of renewable energy sources that can help in meeting the continent's demand for electricity to promote economic growth and meet global targets for CO_2 reduction. Green hydrogen is considered one of the most promising technologies for energy generation, transportation, and storage. In this paper, the prospects of green hydrogen production potential in different countries in Africa are investigated along with its usage for future implementation. Moreover, an overview of the benefits of shifting to green hydrogen technology is presented. The current African infrastructure and policies are tested against future targets and goals.

Keywords Green · Hydrogen · Electrolysis · Power to X · Renewable energies · Policy · Hydrogen

Introduction

The world is facing many challenges regarding climate changes coming from greenhouse gases and CO_2 emissions which threaten Earth's viability for individuals [1]. Based on the Paris Agreement, for limiting of the global warming issue below 2 °C, the greenhouse gas emissions must be declined by 25% in 2030, while it's preferable to limit them below 1.5 °C for reaching net zero gas emissions by 2050 [1, 2]. Due to the increase of world population and high energy consumption, the world researchers are exerting efforts for exploring ecofriendly renewable energy resources

---

N. A. Seada · T. M. Hatem (✉)
Centre for Simulation Innovation and Advanced Manufacturing, The British University in Egypt (BUE), El-Sherouk City, Cairo 11837, Egypt
e-mail: tarek.hatem@bue.edu.eg

N. A. Seada
e-mail: nourabouseada@bue.edu.eg

Faculty of Energy and Environmental Engineering, The British University in Egypt (BUE), El-Sherouk City, Cairo 11837, Egypt

F. Tesfaye et al. (eds.), *REWAS 2022: Energy Technologies and CO_2 Management (Volume II)*, The Minerals, Metals & Materials Series,
https://doi.org/10.1007/978-3-030-92559-8_16

as green hydrogen to be sustainable and withstand the development of nations and for investigating economically a clean energy technology for storing, converting, and generating electricity [3, 4].

According to the world agreements and many partnerships across borders green hydrogen started to be gradually implemented in many regions, countries as the European Union, Japan, Spain, Australia, Finland, France, Germany, Portugal, Chile, and Norway [5]. According to IEA's Hydrogen Projects Database, green hydrogen demonstration projects accounts with a weekly basis increase around 320 projects worldwide. In case of Africa, it has a great potential for green hydrogen implementation since it is a well-suitable place that is rich with abundant energy sources [4]. Additionally, maintaining a clean hydrogen economy would not only decrease exposure to geopolitical and oil price instability but also decrease the cost of energy for countries which depend on diesel [3]. In order to overcome weakness and disparity in some areas and to provide them with permanent energy supply, excess renewable energy will be stored to green hydrogen's capacity [6].

Benefits of Implementing Green Hydrogen to the African Infrastructure

Green hydrogen will be an ideal solution to be the long-term promising alternative for fuel cells but with providing a cleaner energy economy that fossil fuel cell has failed to deliver as well as solving the electrification problems in Africa. According to [6], As shown, Fig. 1 describes different regions facing different challenges in Africa. It was indicated that about half of the people on West Africa, 60% of South Africa, 2% of North Africa, and most of Eastern and middle Africa lack the access to electricity. Besides, the Gross Domestic Product (GDP) per capita is the highest in North Africa [7].

The present infrastructure might be repurposed for green hydrogen production since that 1 kg of green hydrogen production can serve about 57 kwh/kg H2 [range

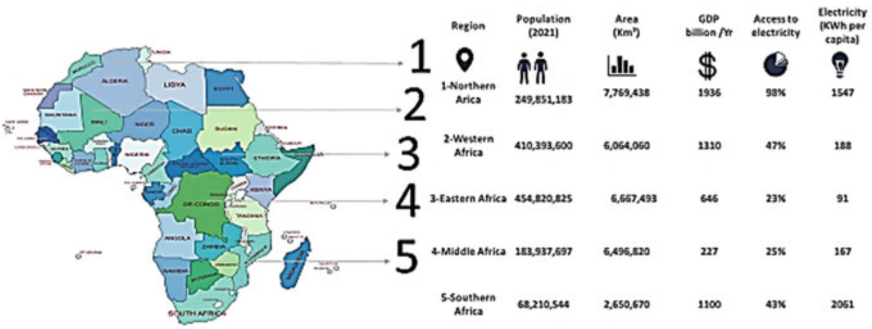

Region	Population (2021)	Area (Km²)	GDP billion /Yr	Access to electricity	Electricity (KWh per capita)
1-Northern Arica	249,851,183	7,769,438	1936	98%	1547
2-Western Africa	410,393,600	6,064,060	1310	47%	188
3-Eastern Africa	454,820,825	6,667,493	646	23%	91
4-Middle Africa	183,937,697	6,496,820	227	25%	167
5-Southern Africa	68,210,544	2,650,670	1100	43%	2061

Fig. 1 Africa energy landscape [7]

51–84 kwh/kg H2] which means that the electrification problem in most of the African region as shown in Fig. 1 can be solved by producing a range of 2–10 kg H2 per capita using renewable energy [8].

With no efforts, integrating hydrogen into the African energy delivery infrastructure can be done easier than other energy storage technologies because of the hydrogen high specific testing, preparation and characterization of promising materials such as metal oxides, energy content between all conventional fuels [9]. Hydrogen is utilized as a fuel source and light energy carrier [5]. In the African future eras, it will be a promising alternative energy path that can be used in various applications as shown in Fig. 2 and will be a key for decarburization to numerous pathways with applications across many sectors such as chemical production, e.g. oil refining methanol, ammonia and iron and steel production, power sector and transportation, e.g. aviation shipping and heavy-duty vehicle market. In addition to that, it can be injected with a certain share to the existing natural gas grids up for minimizing the consumption of natural gas, thereby reducing gas emissions in end-use sectors as gas turbines in the power sector and heat demand in buildings [10–15].

Besides, the green hydrogen can be utilized in the decarburization of the iron and steel industry with direct reduction of iron ore with green hydrogen. In a study, a mass and energy flow model was done using Python, which is an open-source software for testing the viability for utilization of hydrogen as a direct reduction of iron ore (HDRI) coupled with electric arc furnace (EAF) for carbon-free steel production, it showed that this model will decrease the emissions of steel industry by 35%. However, the energy consumption for one ton of liquid steel (tls) production

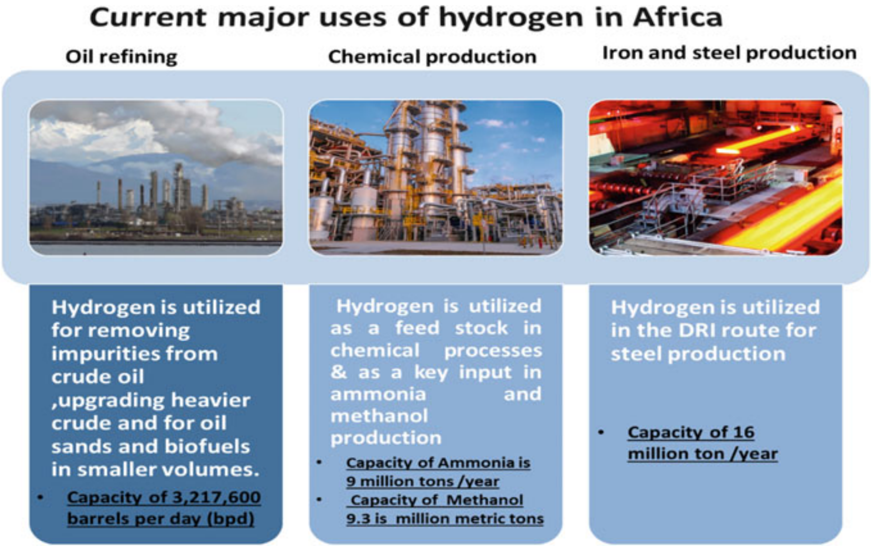

Hydrogen is utilized for removing impurities from crude oil ,upgrading heavier crude and for oil sands and biofuels in smaller volumes.

- Capacity of 3,217,600 barrels per day (bpd)

Hydrogen is utilized as a feed stock in chemical processes & as a key input in ammonia and methanol production

- Capacity of Ammonia is 9 million tons /year
- Capacity of Methanol 9.3 is million metric tons

Hydrogen is utilized in the DRI route for steel production

- Capacity of 16 million ton /year

Fig. 2 Current major uses of hydrogen in Africa [19–21] using the process of blast furnace (BF) basic oxygen furnace route (BOF) is 3.48 MWh, while for HDRI-EAF route was found to be slightly more by 3.72 MWh [16].

Furthermore, hydrogen can be used on the approaches for enhancing the photo-catalytic water splitting towards hydrogen production in Africa by developing the photo-catalysts, fabrication of novel-heterojunction constructions, titanium dioxide, TiO_2, and graphitic carbon nitride, g-C_3N_4, with other semiconductors with Z-scheme was found to be a promising and an efficient photo-catalyst in water splitting [17]. Also, it can be used in the generation of liquid fuels by means of solar energy coupled with their use in direct liquid fuel cells. Moreover, the performance of the CO_2 reduction products, for instance, methanol and formaldehyde, nitrogen fixation (e.g., ammonia and hydrazine), used a as solar liquid fuels and hydrogen storage materials [18]. Moreover, there are some polices that are driving the use of green hydrogen for future implementation including the joint effort and partnership across borders such as (AHP), “Agenda 2063” and European Hydrogen Strategy [5].

The Performance of Green Hydrogen in Different Countries of Africa

The production of green hydrogen economy potential from renewable sources in many countries was investigated by different studies. First, a study was done in Pakistan showing the availability of different renewable resources available in Pakistan such as wind, solar, biomass, geothermal, and municipal solid waste. Also, regarding the estimation of generating hydrogen form the current technologies which showed that the most viable feedstock for generating hydrogen supply chain is as follows: biomass with 6.6 million tonnes of hydrogen’s annual production, solar photovoltaic (PV) with 2.8 million tonnes of hydrogen’s annual production, and municipal solid waste with 1 million tonnes of hydrogen’s annual production Similarly, for Argentina, the same estimation was analyzed. This shows that Argentina has only 10% of land proper for the renewable projects, and this is enough for replacing the total fuel used in transportation [21]. Additionally, green hydrogen production potential was tested in Venezuela using electrolysis of water from wind and mini hydro energies. It was obtained that a total production of 2.073×1010 kg of H_2 per year, which is approximately 95% of solar photovoltaic energy [22]. In Algeria, an analysis of renewable energies (i.e., solar photovoltaic and wind) was done both statically and graphically using geographical information system (GIS) to test the potential for the hydrogen production. The analysis showed the following: (1) the highest irradiation was found in Tamenrasset equal to 2413 KiloWatt Hours (kWh)/m^2/year; (2) the highest wind speed was found in Adrar equal to 6.38 m/s; (3) the lowest irradiation was found in Al-Taref equal to 1692 kWh/m2/year; and (4) the lowest wind speed was found in Tizi Ouzou equal to 1.6 m/s [23]. While in South Africa, Egypt, and Nigeria, comparing the availability of different renewable sources available such as hydro, solar, wind, and biomass [28]. It was found that

South Africa is a very promising model for solving energy challenge utilizing wind and solar energy. On the other hand, Egypt has high potential in using hydropower and emergent solar power base, and Nigeria has promising sectors of hydro, solar, and wind power respectively [24].

Likely, under several Moroccan climate zones, the yield and making cost for electrolytic hydrogen obtained from different solar technologies was studied. This study showed that Morocco have high competitive potential in generating green hydrogen specifically for PV technology with a levelized cost of Hydrogen production LCO_{H2} of 5.57 $/Kg, and the optimal technology for hydrogen production is the 1-axis tracking because it is capable in generating high amounts of hydrogen close to the amount of 2-axis PV with lower cost [25]. Additionally, an assessment was studied in Durban, South Africa for building of the solar resource that showed that Durban contain a significant solar energy source [7]. Furthermore, an estimate in Ukraine on resource potential for wind–hydrogen power was done, which shows that wind power plants will generate 2174 billion kWh that can produce (43 million tons) of green hydrogen per year. This estimation is nearly about 15 times greater than the yearly electricity consumption in Ukraine [26]. Moreover, the potential in Ecuador was analyzed, which tested the production of green hydrogen by a PEM electrolizer of 75% efficiency. The results showed a production of 4.55×10^8 kg/year [27]. Finally, an overview for South African hydrogen infrastructure (HySA-infrastructure) for fuel cells and energy storage showed that the associated hydrogen infrastructure and fuel cells will be promising new market that will not only enhance the growth for platinum but also will found significant new opportunities internationally and locally in RSA since that. SA is rich with extraordinary amount of platinum deposits found in SA which represents 75% of the world platinum deposits [28].

Conclusion

Regarding the catastrophic climate changes and global warming issue, the steady stream of greenhouse gases and CO_2 emissions have to be widely reduced by replacing the fossil fuels by any source of renewable energy. As agreed to many experts the implementation of green hydrogen will meet the Paris Agreements goals and electrolysis which is powered using the renewable energy can be used for the novel development of green hydrogen evolution in Africa. This approach, if successful, will provide a new generation of green hydrogen which will shift Africa to a whole new level. Some of key findings showed that as green hydrogen is carried out in Africa with a massive range, there are lots of challenges that will take place; however, many benefits will occur socially and economically such that it will implement a clean mode of water, transportation and air; furthermore, the electrification rate will gradually increase. Africa can also use electricity or thermal energy from renewable sources to direct cooking, where it may be more energy-efficient avoiding energy consumed in compressing, storing, and transporting compressed energy in hydrogen for basic needs. Finally, the most important benefit is that this prospective will create a lot of job opportunities thus will increase the wealth and bring socioeconomic benefits.

References

1. Töpler J, Lehmann J, Hydrogen and fuel cell: technologies and market perspectives, Springer
2. Bhagwat SRK, Olczak M (2020) Green hydrogen: bridging the energy transition in Africa and Europe. Florence SchRegul—Energy. https://doi.org/10.2870/126402
3. Clifford Chance (2021) Focus on hydrogen: a new energy frontier for Africa, https://www.cliffordchance.com/content/dam/cliffordchance/briefings/2021/01/focus-on-hydrogen-a-new-energy-frontier-for-africa.pdf
4. Wall RF (1960) An Atlas of Africa, vol 36, no 3
5. I Energy Agency (2019) The future of hydrogen
6. IRENA (2019) Hydrogen: a renewable energy perspective, September
7. Sugawara E, Nikaido H (2014) Properties of AdeABC and AdeIJK efflux systems of Acinetobacter baumannii compared with those of the AcrAB-TolC system of Escherichia coli. Antimicrob Agents Chemother 58(12):7250–7257. https://doi.org/10.1128/AAC.03728-14
8. IRENA (2015) Africa 2030: roadmap for a renewable energy future. REmap 2030 Program 72. www.irena.org/remap
9. Deutsche Umwelthilfe (DUH) (2020) Hydrogen and power-to-X. Ideas for a green hydrogen strategy. Position Pap, Apr 2020
10. Belward A et al (2011) Renewable energies in Africa. JRC Sci Tech Rep 1–62. https://doi.org/10.2788/1881
11. Deutsche Umwelthilfe (DUH) Hydrogen and power-to-X. Ideas for a green hydrogen strategy. Position Paper
12. Lehmann J, Luschtinetz T, Gulden J (2018) Power to X—green hydrogen for electrical energy and fuel, for production and products. E3S Web Conf 70:10–12. https://doi.org/10.1051/e3sconf/20187001011
13. Matthes C, Aruffo V, Retby-Pradeau L, The risks and opportunities of green hydrogen production and export from the MENA Region to Europe
14. Velazquez Abad A, Dodds PE (2020) Green hydrogen characterisation initiatives: Definitions, standards, guarantees of origin, and challenges. Energy Policy 138. https://doi.org/10.1016/j.enpol.2020.111300
15. Basheer AA, Ali I (2019) Water photo splitting for green hydrogen energy by green nanoparticles. Int J Hydrog Energy 44(23):11564–11573. Elsevier Ltd, 03 May 2019. https://doi.org/10.1016/j.ijhydene.2019.03.040
16. Bhaskar A, Assadi M, Somehsaraei HN (2020) Decarbonization of the iron and steel industry with direct reduction of iron ore with green hydrogen. Energies 13(3). https://doi.org/10.3390/en13030758
17. Fajrina N, Tahir M (2019) A critical review in strategies to improve photocatalytic water splitting towards hydrogen production. Int J Hydrogen Energy 44(2):540–577. https://doi.org/10.1016/j.ijhydene.2018.10.200
18. Fukuzumi S (2017) Production of liquid solar fuels and their use in fuel cells. Joule 1(4):689–738. https://doi.org/10.1016/j.joule.2017.07.007
19. Borschette A (2019) Green hydrogen opportunities in selected industrial processes Workshop summary report, June 2019. https://doi.org/10.2760/634063
20. I Renewable Energy Agency and T Methanol Institute (2021) Innovation outlook renewable methanol in partnership with 2021

21. Gielen D, Boshell F, Saygin D, Bazilian MD, Wagner N, Gorini R (2019) The role of renewable energy in the global energy transformation. Energy Strateg Rev 24:38–50. https://doi.org/10.1016/j.esr.2019.01.006
22. Summeth Summeth-Sustainable marine methanol deliverable D5.1 CO-FUNDED BY (2018)
23. Pattabathula V, Richardson J (2016) Introduction to ammonia production. Chem Eng Prog 112(9):69–75. https://www.aiche.org/resources/publications/cep/2016/september/introduction-ammonia-production. Accessed 10 Jun 2021
24. Aliyu AK, Modu B, Tan CW (2018) A review of renewable energy development in Africa: a focus in South Africa, Egypt and Nigeria. Renew Sustain Energy Rev 81, June 2017:2502–2518. https://doi.org/10.1016/j.rser.2017.06.055
25. Ufomba HU (2020) The African union development agenda 2063: can Africa get it right? Brazilian J Dev 6(8):62626–62648. https://doi.org/10.34117/bjdv6n8-627
26. Kudria S, Ivanchenko I, Tuchynskyi B, Petrenko K, Karmazin O, Riepkin O (2021) Resource potential for wind-hydrogen power in Ukraine. Int J Hydrogen Energy 46(1):157–168. https://doi.org/10.1016/j.ijhydene.2020.09.211
27. Vázquez FV et al (2018) Power-to-X technology using renewable electricity and carbon dioxide from ambient air: SOLETAIR proof-of-concept and improved process concept. J CO_2 Util 28, no September:235–246. https://doi.org/10.1016/j.jcou.2018.09.026
28. Bessarabov D et al (2017) South African hydrogen infrastructure (HySA infrastructure) for fuel cells and energy storage: overview of a projects portfolio. Int J Hydrogen Energy 42(19):13568–13588. https://doi.org/10.1016/j.ijhydene.2016.12.140

The Influence of H_2 and CO Atmospheres on SiO Formation

Trygve Storm Aarnæs, Merete Tangstad, and Eli Ringdalen

Abstract Producing silicon with H_2 would be advantageous from an environmental viewpoint because it opens up a potentially CO_2-free process. This study investigated the interplay between atmosphere and the reaction between SiC and SiO_2 pellets. Process gasses containing Ar, H_2, and CO were examined at 1650 and 1750 °C. In pure Ar, the reaction was slow and found to be limited by mass transfer. The reaction was faster in the presence of H_2, and, in this case, it was instead slow reaction kinetics that was rate limiting. However, the effect disappeared when adding CO together with H_2. Both H_2 and CO produced SiC whiskers at 1650 °C, but H_2 to a greater degree than CO. The whiskers reinforced the pellets, which resulted in up to 20 times higher strength for a CO and H_2 containing process gas. Process gasses without of CO resulted in weaker pellets instead.

Keywords Hydrogen · SiO formation · Silicon · SiC whiskers

Introduction

The current process for producing silicon reduces silica (SiO_2) with carbon in submerged arc furnaces [1]. SiO_2 is supplied as quartz; it reacts with silicon carbide in the hot region of the furnace following Reaction (1). This generates SiO gas, which flows up and reacts with carbon in the relatively cool top region of the furnace. Reaction (2) transforms SiO gas and carbon to SiC, which flows downwards. Finally, the elemental Si forms through Reaction (3) from a reaction between silicon carbide and

---

T. S. Aarnæs (✉) · M. Tangstad
Department of Materials Science and Engineering, Norwegian University of Science and Technology, Trondheim, Norway
e-mail: trygve.s.aarnas@ntnu.no

M. Tangstad
e-mail: merete.tangstad@ntnu.no

E. Ringdalen
Metal Production and Processing, SINTEF Industry, Trondheim, Norway
e-mail: Eli.Ringdalen@sintef.no

F. Tesfaye et al. (eds.), *REWAS 2022: Energy Technologies and CO_2 Management (Volume II)*, The Minerals, Metals & Materials Series,
https://doi.org/10.1007/978-3-030-92559-8_17

SiO gas.

$$SiC + 2SiO_2 = 3SiO + CO \tag{1}$$

$$SiO + 2C = SiC + CO \tag{2}$$

$$SiC + SiO = 2Si + CO \tag{3}$$

$$SiO_2 + H_2 = SiO + H_2O \tag{4}$$

Because this process is carbothermal, CO_2 emissions are inevitable, even if there is a completely green energy source powering the process. As such, the ways to remove CO_2 emissions from silicon production requires either replacing 100% of fossil carbon with bio-carbon, or using something else than carbon as the reductant. For many other metals, hydrogen (H_2) is suggested as a possible substitute for carbon.

SiO_2 is a very stable oxide, and as a result, fully reducing it to silicon is challenging with H_2 as the reductant. However, a partial reduction, where H_2 only reduces SiO_2 to SiO gas might be possible. Several researchers have reported Reaction (4) to proceed to the right with modest reaction rates, but it was only investigated up to 1630 °C [2–4]. Further reduction from SiO to Si needs a more potent reductant, such as carbon. As a result, a silicon process utilizing H_2 may end up as a carbon/H_2 hybrid process.

This will require detailed knowledge on the difference between the Si–O–C system and the Si–O–C–H system. Research into this system has shown that many reactions from the Si–O–C system exhibit faster reaction rates in the Si–O–C–H system. Li et al. reported that when H_2 is present, SiC formation from carbon and quartz begins at a lower temperature, and that silicon formation from SiC and SiO_2 raw material gives a higher yield [5, 6]. Improved SiC whisker growth is also a difference between the two systems [7]. This is suggested to follow from the presence of small amounts of CH_4 produced by H_2 equilibrating with carbon, which improves carbon transfer through the gas phase. If a sufficiently high methane pressure is achieved it can even be used as the primary carbon source which was shown by Monsen et al. [8]. They also reported SiO and methane to react at a lower temperature than SiO and carbon does.

The aim of this study is to examine the effect H_2 containing atmospheres has on Reaction (1). Because silicon reduction with H_2 will likely take place in the presence of carbon, it is necessary to understand the advantages and disadvantages of being in the Si–O–C–H system. In addition, Ar and CO was used in the process gas. Ar as a comparison to H_2, and CO because it is present in current silicon producing furnaces. The holding temperature varied between 1650 and 1750 °C, which is below and above the melting point of SiO_2 as there may be different reaction mechanisms occurring at the two temperatures.

Experimental

Raw Materials

SiO and CO was produced through Reaction (1), from pellets made from a 2:1 molar ratio of SiO_2 and SiC powders. The SiC powder was provided by Washington Mills and was at least 95% pure, with the main impurities being SiO_2, Al, and Fe. The quartz was “Quartz type A” described by Jusnes [9], which is 99,98% pure. The powders were mixed in a Turbula Type T2C Shaker Mixer for 6 h, then the powders were pelletised in a steel-rotating mill with water as binder and sieved to a size range of 1–1, 5 mm. Finally, the pellets were dried for 6 h at 120 °C and then heated to 1200 °C for 30 min for strength.

Setup

Figure 1 shows a drawing of the reactor used for the experiments; it is constructed out of graphite, with the exception being the top part of the gas lance. The upper part of the reactor is the condensation chamber, and the lower part is the reaction chamber. The crucible is inside the reaction chamber, it has a ledge 1 cm above its bottom and a perforated disk rests on that ledge. The perforated disk holds the SiO_2/SiC pellets. The process gas enters through a lance that extends from above the condensation chamber, through the reaction chamber and into the space between the perforated disk and the crucible floor. The gas flows through the perforated disc, through the raw materials where it affects Reaction (1). After leaving the reaction chamber, the gas passes through the condensation chamber where remaining SiO, and some of CO, is converted to SiO_2 and SiC. A type C thermocouple measures the temperature within the reaction chamber. It is placed at the same height as the perforated disk the raw material rests on.

The setup was heated in a resistance heated vertical graphite tube furnace. A flow of 1 slpm (litres per minute at 0 °C and 1 bar) Ar was used during the 30-min heating step and during cooling. During the 60 min of holding time, the gasses used are shown in Table 1. Once the setup cooled to room temperature, the crucible was weighed to determine the weight loss. The setup clogged somewhat frequently, and in the cases where a too high pressure built up within the furnace the experiments were aborted before finishing the full holding time. These instances are written in parenthesis in the experimental matrix shown in Table 1, additionally, they are noted in figures as a cross.

A SEM (Zeiss-Supra 55VP, Scanning Electron Microscope) was used to investigate the used crucibles and remaining raw material after the experiments. The crucibles were first sawed vertically to investigate the interior crucible wall. They were examined with a secondary electron detector, and with EDS (energy-dispersive x-ray spectroscopy) to determine the chemical composition of the reaction products.

Fig. 1 Experimental setup used during the high-temperature experiments

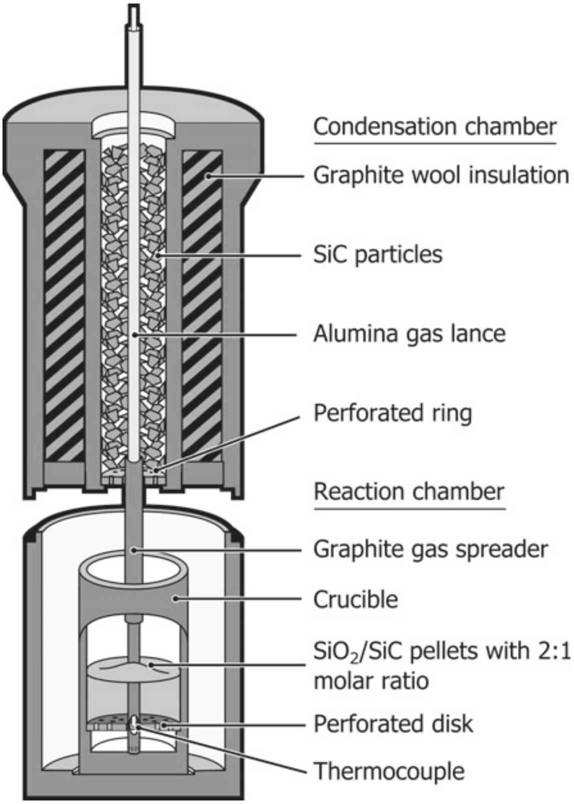

Table 1 Experimental matrix for high temperature experiments. Numbers outside of parenthesis is the number of experiments that completed the full holding time, numbers in parenthesis is the number of experiments that had to be stopped before completing the holding time

	Argon	100% H_2	25% CO 75% Ar	25% CO 75% H_2
1650 °C	2	2	2	2
1750 °C	2	2	4	(3)

In addition, a press was used to measure the pellet strength. Pellets were taken from experiments at 1650 °C because it is below the melting point of SiO_2. Some of the pellets that had a large strength increase were gently split into several pieces to expose the pellet interior to imaging.

Results and Discussion

Effect of Gasses on SiO Production

During each experiment, the SiO_2/SiC pellets reacted and produced SiO and CO gas that left the crucible. Thus, the weight loss recorded after each experiment indicates the extent of SiO and CO gas production occurring in the setup. A greater weight loss means greater gas production. By varying the atmosphere in the setup, the gas

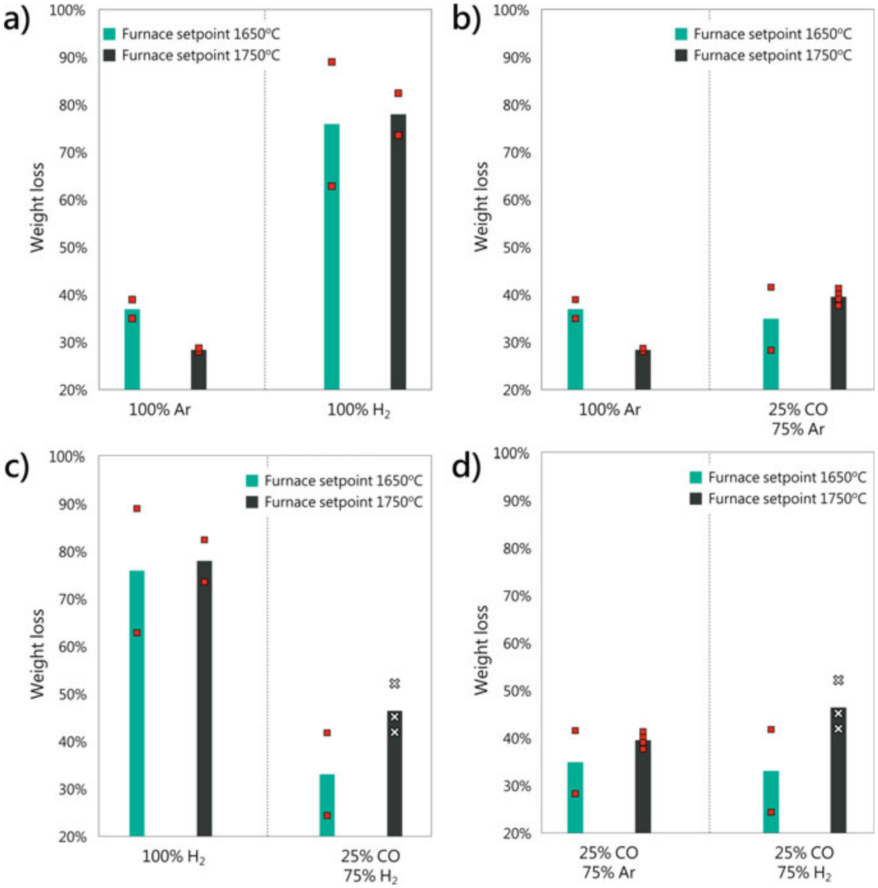

Fig. 2 Weight loss relative to the starting raw material when the different process gasses are used, **a** compares Ar to H_2, **b** compares Ar to 75% Ar with 25% CO, **c** compares H_2 to 75% H_2 with 25% CO, and **d** compares 25% CO and 75% Ar to 25% CO and 75% H_2. Squares signify experiments that completed the full holding time and crosses show the experiments that was aborted before completing the holding time

production from the pellets also changed. Figure 2 shows the weight loss during the experiments.

H_2 leads to greater gas production than Ar; this is evident from Fig. 2a which compares weight loss in 100% H_2 to weight loss in 100% Ar. This might be due to H_2 reducing the viscosity of the gas and thus increasing mass transfer, or due to its effect on the reaction mechanism. This was further investigated by adding CO to the process gas. Increasing the CO pressure in the setup should reduce the reaction rate because it lowers the driving force for Reaction (1). However, the CO content does not affect the gas production in an Ar atmosphere. Figure 2b shows that a process gas with 100% Ar sees roughly the same SiO gas production as 25% CO with 75% Ar. Thus, for 100% Ar the SiO formation is limited by mass transfer, because adding CO to the process gas did not affect the SiO generation. Figure 2c compares a process gas with 100% H_2, to one with 25% CO and 75% H_2. CO causes the SiO gas production to drop significantly. This means for a process gas with 100% H_2 the SiO formation is limited by the reaction rate. Figure 2d shows that the gas production in 25% CO and 75% H_2 is almost the same as in 25% CO with 75% Ar. An additional effect of CO was that process gasses containing both CO and H_2 resulted in a clogged condensation chamber due to too much condensation. For example, all experiments at 1750 °C with 25% CO and 75% H_2 had to be aborted after 30 min holding due to pressure buildup.

Possible Mechanisms

At 1750 °C, the SiO_2 in the raw material is liquid, which allows Reaction (1) to proceed through a liquid–solid reaction. But at 1650 °C, SiO_2 is still a solid so the contact area is much more limited, as such it is more likely Reaction (1) happens through gas–solid reactions. Three candidates for the reaction mechanisms are shown in Fig. 3. Figure 3a and Reactions (5) and (6) shows the reaction mechanism and gas–solid reactions in an atmosphere free from H_2, in this case CO_2 is the molecule

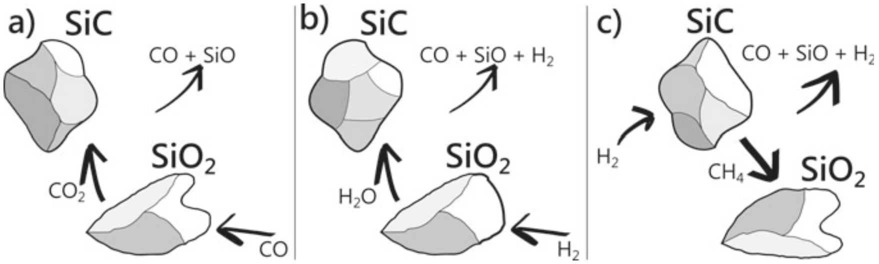

Fig. 3 Three candidates for reaction mechanisms, **a** shows the reaction mechanism in an H_2-free atmosphere where CO_2 is the only species available to perform mass transfer between SiC and SiO_2, **b** shows the reaction mechanism if mass transfer is performed by H_2O, and **c** shows the reaction mechanism if mass transfer is performed by CH_4

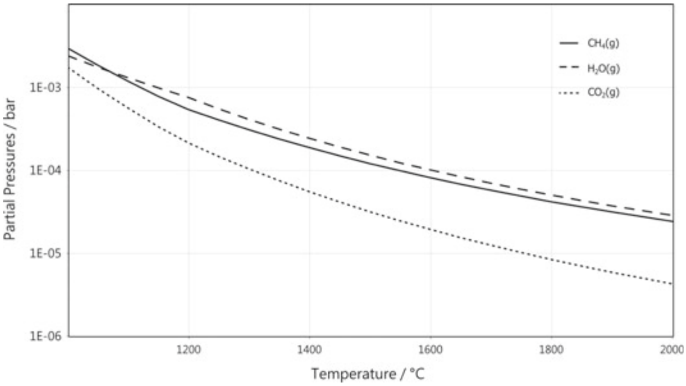

Fig. 4 Equilibrium partial pressures of CO_2, CH_4, and H_2O at 1 bar total pressure. Initial conditions were 1 mol carbon, 0.5 mol CO, and 0.5 mol H_2. Calculated with the software HSC9

carrying out the mass transfer between the particles. Figure 3b and Reactions (7) and (8) shows an analogous reaction mechanism to Fig. 3a, analogous in the sense that oxygen atoms are being transported from SiO_2 to SiC, but by H_2O instead of CO_2. Figure 3c and Reactions (9) and (10) are different from the other mechanisms, because carbon is being transported instead of oxygen. As a result, mass transport proceeds from SiC to SiO_2 instead. Figure 4 shows the equilibrium partial pressures of CO_2, CH_4, and H_2O in a system with carbon calculated with HSC9. It indicates that there is roughly 10 times more CH_4 and H_2O present relative to CO_2, yielding many additional molecules available for mass transfer. Ksiazek et al. attempted reducing quartz with an H_2/CH_4 gas mix through Reaction (9) [10]. They did not find the reaction to proceed at any significant rate, instead the CH_4 deposited carbon on the quartz particles. This might indicate that CH_4 is not very reactive towards SiO_2. Several studies have reported that H_2O restricts the reaction rate of Reaction (7) due to desorption of H_2O from SiO_2 being slow [2, 4]. Thus, if SiO_2 and SiC reacts through Reaction (7) and (8), then Reaction (8) must happen at a much faster rate than Reaction (7) in order to maintain a sufficiently low H_2O content. Moisture may also slow down other reactions, Bootsma et al. reported H_2O to prevent formation of SiC whiskers grown in an H_2 atmosphere [7].

$$SiO_2 + CO = SiO + CO_2 \tag{5}$$

$$SiC + 2CO_2 = 3CO + SiO \tag{6}$$

$$SiO_2 + H_2 = SiO + H_2O \tag{7}$$

$$SiC + 2H_2O = SiO + 2H_2 + CO \tag{8}$$

$$SiO_2 + CH_4 = CO + SiO + 2H_2 \tag{9}$$

$$SiC + 4H_2 + CO = SiO + 2CH_4 \tag{10}$$

All three reaction mechanisms interact with the graphite setup. By reacting with the process gas, graphite may produce CH_4 through Reaction (11), while H_2O and CO_2 can be consumed through Reaction (12) and Reaction (13). These side reactions causes the graphite setup to react with SiO_2 from the raw material, as a result it is not uncommon for the overall raw material reaction to not quite follow the stoichiometry [5, 11, 12]. In addition, SiC can react with SiO which produces elemental Si, but this usually does not occur below 1800 °C [13].

$$C + 2H_2 = CH_4 \tag{11}$$

$$C + CO_2 = 2CO \tag{12}$$

$$C + H_2O = CO + H_2 \tag{13}$$

Pellet Strengthening

Some process gasses resulted in SiC whisker formation within the SiO_2/SiC pellets. Figure 5 shows this for an experiment with 5% CH_4, 25% CO and 70% H_2 as process gas. Figure 5b shows the pellet interior, which contains a large amount of SiC whiskers in the space between the SiC and SiO_2 particles. These SiC whiskers had a notable effect on the strength of the pellets, and process gasses that promotes SiC whiskers reinforced and strengthened the pellets. Figure 6 shows the maximum load the pellets withstood prior to breaking as a function of the process gas. The pellets that experienced 100% Ar or 100% H_2 had a large reduction in strength, in fact, they were so weak most broke while being placed into the press. The process gas containing 25% CO and 75% Ar resulted in a moderate strength increase, while a large strength increase occurred for process gasses containing both CO and H_2. The strength increase was up to 20 times higher than the fresh pellets. These process gasses resulted in an upper section of the pellets covered by a faintly blue layer of reaction product, which loosely connected the pellets. This upper region had significantly higher strength than the lower region. Figure 5c shows that pellets from this region have a surface layer of SiO_2 droplets resting on a layer of SiC whiskers. A structure reminiscent of SiC–SiO_2 core shell whiskers, which is commonly seen for SiO condensation [14]. This structure grows as SiC whiskers surrounded by a shell of SiO_2, where only the tip is molten. Due to the high temperature, the SiO_2 layer melts and then contracts from surface tension, which forms the droplets. The

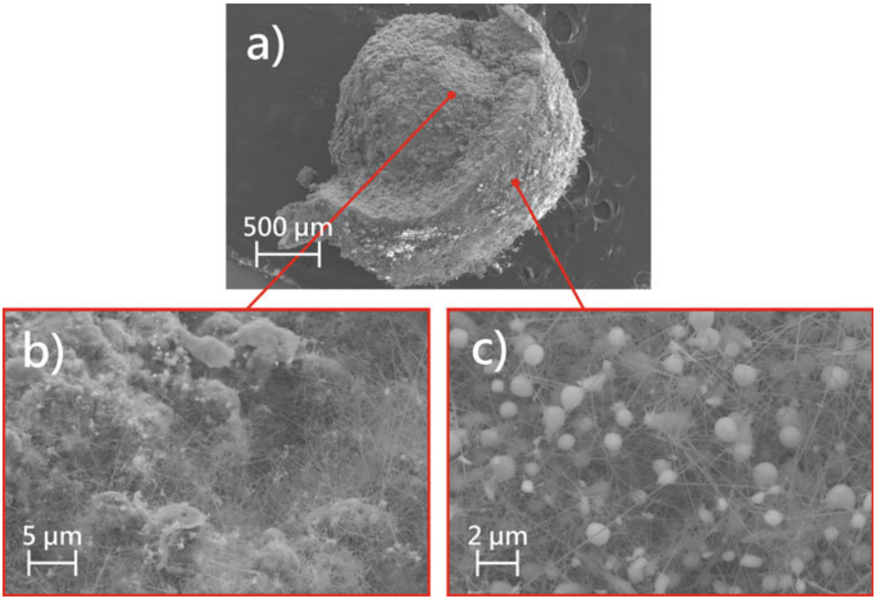

Fig. 5 SEM images of a pellet used with a process gas containing 5% CH_4, 25% CO, and 70% H_2. Prior to being imaged to was crushed to reveal its interior. **a** Shows an overview image of the pellet and how part of its outer layer broke off, **b** shows the interior of the pellet, and that SiC whisker formation has occurred within it, **c** shows the surface of the pellet, which is covered by a layer of SiO_2 droplets suspended by a layer of whiskers

center of the pellet was filled with SiC whiskers, but was absent of the SiO_2 seen on the surface layer.

The biggest strength increase occurred when the process gas contained both CO and H_2, with a smaller effect seen in 25% CO and 75% Ar. Thus, both CO and H_2 have separate effects on the strength of the reinforced pellet structure. The main driving force for weakening the pellet is how much of it reacts. As the individual particles shrink there is more room to move and the pellet disintegrates more easily. As discussed earlier, the strength increase results from SiC whisker reinforcement. With this in mind, the effect of H_2 is summarized as, increasing the pellet consumption and increasing the degree of whisker formation. Likewise, CO also increases the whisker formation, albeit to a lesser extent, but it suppresses the increased pellet consumption of H_2-containing atmospheres. Thus, it is no surprise that CO with H_2 has the highest strength, while 100% Ar or H_2 has the lowest, and that Ar with CO ranks in the middle.

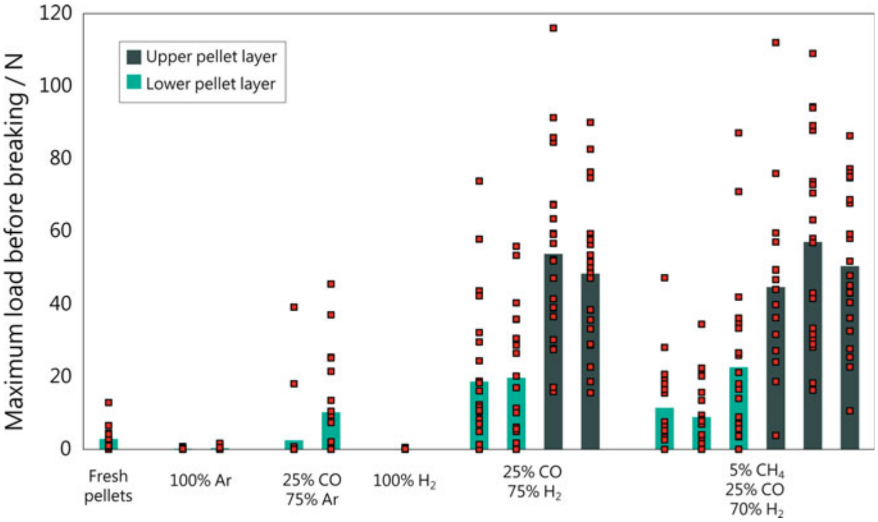

Fig. 6 The maximum load applied to pellets before breaking. CO and H_2 in combination gave rise to a substantial pellet strength increase, which was not seen when the gasses were used separately. The strength also varied between the surface pellets and the lower pellets. The bars show the average, and the red squares are individual data points. The 5% CH_4, 25% CO, and 70% H_2 is from a different experimental series not yet published, but is included as CH_4 does not seem to affect pellet strengthening

Conclusions

This study has investigated reactions taking place in the Si–O–C–H system. Despite H_2 itself not reducing the raw materials it had a noticeable effect on kinetics and the overall behavior of the system. Particularly:

- H_2 leads to faster gas production from the SiO_2/SiC pellets. However, adding 25% CO suppresses the increase in gas production caused by H_2, resulting in an equivalent reaction rate as in Ar.
- Both H_2 and CO resulted in the formation of SiC whiskers at 1650 °C. But, H_2 to greater extent than CO, which is possibly due to H_2 promoting Reaction (1) which gives a larger SiO pressure, or it may be a result of CH_4 formation.
- A CO-containing process gas resulted in increased pellet strength. 25% CO and 75% Ar yielded a 5 times increase in strength, whereas 25% CO and 75% H_2, or 5% CH_4, 25% CO, and 70% H_2 resulted in a 20 times increase in strength in comparison to fresh pellets. Examining the pellet interior with a SEM showed that SiC whiskers created a reinforced structure of SiC and SiO_2 particles within a mesh of mechanically strong SiC whiskers, which kept the structure from breaking apart. However, if H_2 is used without adding CO the pellets weaken instead due to increased pellet consumption.

Acknowledgements The authors gratefully acknowledge financial support from the Research Council of Norway (project number 280968).

References

1. Schei A (1998) Production of high silicon alloys. Trondheim: Tapir. Accessed 29 June 2019. http://urn.nb.no/URN:NBN:no-nb_digibok_2010021004001
2. Gardner RA (1974) The kinetics of silica reduction in hydrogen. J Solid State Chem 9(4):336–344
3. Han G, Sohn HY (2005) Kinetics of the hydrogen reduction of silica incorporating the effect of gas-volume change upon reaction. J Am Ceram Soc 88(4):882–888. https://doi.org/10.1111/j.1551-2916.2005.00144.x
4. Tso ST, Pask JA (1982) Reaction of fused silica with hydrogen gas. J Am Ceram Soc 65(9):457–460. https://doi.org/10.1111/j.1151-2916.1982.tb10514.x
5. Li X, Zhang G, Ostrovski O, Tronstad R (2016) Effect of gas atmosphere on the formation of silicon by reaction of SiC and SiO_2. J Mater Sci 51(2):876–884. https://doi.org/10.1007/s10853-015-9413-2
6. Li X, Zhang G, Tang K, Ostrovski O, Tronstad R (2015) Carbothermal reduction of quartz in different gas atmospheres. Metall Mater Trans B 46(3):1343–1352. https://doi.org/10.1007/s11663-015-0293-2
7. Bootsma GA, Knippenberg WF, Verspui G (1971) Growth of SiC whiskers in the system SiO_2-C-H_2 nucleated by iron. J Cryst Growth 11(3):297–309
8. Monsen B, Kolbeinsen L, Prytz S, Myrvågnes V, Tang K (2013) Possible use of natural gas for silicon or ferrosilicon production. In: Proceeding of the 13th international ferroalloys congress, Kazakhstan, vol 1, pp 467–478
9. Jusnes KF (2020) Phase transformations and thermal degradation in industrial quartz. NTNU. Accessed 08 Sept 2020. https://ntnuopen.ntnu.no/ntnu-xmlui/handle/11250/2675473
10. Ksiazek M, Tangstad M, Dalaker H, Ringdalen E (2014) Reduction of SiO_2 to SiC using natural gas. Metall Mater Trans E 1(3):272–279. https://doi.org/10.1007/s40553-014-0027-4
11. Folstad MB, Ringdalen E, Tveit H, Tangstad M (2021) Effect of different SiO_2 polymorphs on the reaction between SiO_2 and SiC in Si production. Metall Mater Trans B. https://doi.org/10.1007/s11663-020-02053-x
12. Tangstad M Reaction rates of $2SiO_2+SiC=3SiO+CO$ in pellets at elevated temperatures, p 11
13. Jayakumari S (2020) Formation and characterization of β-and α-silicon carbide produced during silicon/ferrosilicon process. NTNU. Accessed 19 Feb 2021. https://ntnuopen.ntnu.no/ntnu-xmlui/handle/11250/2678922
14. Broggi A, Tangstad M, Ringdalen E (2019) Characterization of a Si-SiO_2 mixture generated from SiO(g) and CO(g). Metall Mater Trans B 50(6):2667–2680. https://doi.org/10.1007/s11663-019-01678-x

Author Index

F. Tesfaye et al. (eds.), *REWAS 2022: Energy Technologies and CO_2 Management (Volume II)*, The Minerals, Metals & Materials Series,
https://doi.org/10.1007/978-3-030-92559-8

Subject Index

F. Tesfaye et al. (eds.), *REWAS 2022: Energy Technologies and CO_2 Management (Volume II)*, The Minerals, Metals & Materials Series,
https://doi.org/10.1007/978-3-030-92559-8